**Title**
The neural basis of thirst



**Author**
Zimmerman, Christopher A

**Publication Date**
2019

Peer reviewed|Thesis/dissertation

The neural basis of thirst

by
Christopher A. Zimmerman

DISSERTATION
Submitted in partial satisfaction of the requirements for degree of
DOCTOR OF PHILOSOPHY

in

Neuroscience

in the

GRADUATE DIVISION
of the
UNIVERSITY OF CALIFORNIA, SAN FRANCISCO

Approved:

DocuSigned by:
Roger Nicoll
44EF5DD68BD1430...

Roger Nicoll
Chair

DocuSigned by:
Zachary Knight
DocuSigned by:
Vikaas Sohal
DocuSigned by:
Nirao Shah
F806E9A8D8D148C...

Zachary Knight
Vikaas Sohal
Nirao Shah

Committee Members

**ACKNOWLEDGEMENTS**

I would like to thank my advisor, Zack, for his insight and enthusiasm; my friends and labmates for their encouragement and support; and my partner, Grace, for countless wonderful moments.

The material in this dissertation is reprinted with permission from the following publications:

> Christopher A. Zimmerman, Yen-Chu Lin, David E. Leib, Ling Guo, Erica L. Huey, Gwendolyn E. Daly, Yiming Chen, Zachary A. Knight. Thirst neurons anticipate the homeostatic consequences of eating and drinking. *Nature* 537, 680–684, 2016.
>
> Christopher A. Zimmerman, David E. Leib, Zachary A. Knight. Neural circuits underlying thirst and fluid homeostasis. *Nature Reviews Neuroscience* 18, 459–469, 2017.
>
> David E. Leib*, Christopher A. Zimmerman*, Ailar Poormoghaddam, Erica L. Huey, Jamie S. Ahn, Yen-Chu Lin, Chan Lek Tan, Yiming Chen, Zachary A. Knight. The forebrain thirst circuit drives drinking through negative reinforcement. *Neuron* 96, 1272–1281, 2017. *These authors contributed equally
>
> Christopher A. Zimmerman, Erica L. Huey, Jamie S. Ahn, Lisa R. Beutler, Chan Lek Tan, Seher Kosar, Ling Bai, Yiming Chen, Timothy V. Corpuz, Linda Madisen, Hongkui Zeng, Zachary A. Knight. A gut-to-brain signal of fluid osmolarity controls thirst satiation. *Nature* 568, 98–102, 2019.

The work in this dissertation was supported by the following funding sources:

> NSF Graduate Research Fellowship, 2013–2016
>
> UCSF Discovery Fellowship, 2015–2018
>
> Genentech Foundation Predoctoral Fellowship, 2016–2017
>
> NIH National Research Service Award Predoctoral Fellowship, 2017–2019

## ABSTRACT

The neural basis of thirst

Christopher A. Zimmerman

The physiological conditions within our bodies are remarkably stable. To maintain this internal stability (called 'homeostasis'), we have evolved specialized neural systems that precisely regulate the physiological parameters that are critical for our survival. For example, the brain's thirst circuit monitors the osmolarity and volume of the blood and fine-tunes drinking behavior, cardiovascular tone, and renal function in order to maintain fluid homeostasis.

Thirst has traditionally been viewed as a simple negative feedback response to changes in the blood. However, most natural drinking behavior is regulated too rapidly to be controlled by blood composition directly and instead appears to anticipate homeostatic perturbations before they arise. To address this paradox, we identified genetic markers for neural populations throughout the brain's thirst circuit and used them as tools to investigate the origins of thirst.

Chapter one of this dissertation reviews our historical understanding of thirst and fluid homeostasis. Chapter two describes the first *in vivo* recordings of thirst neuron activity during behavior, which unexpectedly revealed that these cells—historically viewed as merely passive sensors of blood composition—also integrate sensory information from the oropharynx and gastrointestinal tract to predict the homeostatic consequences of eating and drinking. Chapter three describes the motivational mechanism underlying thirst. Chapter four describes a new mode of gut–brain communication that regulates thirst satiation. Together, these experiments have revealed fundamental organizing principles by which the brain monitors the state of the body in order to dynamically control ingestive behavior and maintain physiological homeostasis.

## TABLE OF CONTENTS

## LIST OF FIGURES

*I. Introduction*

---

The material in this chapter is partially reprinted from:

> Christopher A. Zimmerman, David E. Leib, Zachary A. Knight.
> Neural circuits underlying thirst and fluid homeostasis.
> *Nature Reviews Neuroscience* 18, 459–469, 2017.

C.A.Z., D.E.L. and Z.A.K. prepared the manuscript.

## BACKGROUND AND MOTIVATION

Why do we feel thirsty? Early theories posited that thirst is the local sensation of dryness in the mouth and throat[1], but today thirst is conventionally viewed as a negative feedback response to changes in the blood[2,3]: increases in plasma osmolarity or decreases in plasma volume or pressure trigger the sensation of thirst, which motivates animals to find and consume water and thereby restore these parameters to their physiological set points (Figure 1.1).

Our modern understanding of the neural control of thirst originated with the discovery by Bengt Andersson in the 1950s that infusion of hypertonic saline into the anterior hypothalamus of goats stimulates intense drinking and water retention (antidiuresis)[4]. James Fitzsimons later discovered that infusion of the hormone angiotensin into the same area of rats also produces thirst[5]. Together, these and subsequent[6–9] experiments identified a small forebrain region (the lamina terminalis; LT) that monitors homeostatic signals of fluid balance (plasma osmolarity and angiotensin) and translates these signals into appropriate counter-regulatory responses.

The LT is composed of three small, interconnected structures that lie adjacent (anterior and/or dorsal) to the third ventricle. Two of these structures—the subfornical organ (SFO) and the organum vasculosum of the lamina terminalis (OVLT)—are sensory circumventricular organs, meaning that they lie outside the blood–brain barrier and therefore have direct access to the circulation[10]. Information about fluid balance enters the LT primarily through specialized interoceptive neurons in the SFO and OVLT. Some of these interoceptive SFO and OVLT neurons are intrinsically osmosensitive, meaning that their firing rate increases in response to elevations in the tonicity of the extracellular fluid, and many of these osmosensitive neurons are also activated by the hormone angiotensin, which is rapidly generated in the circulation when plasma volume or pressure falls. In addition, some SFO or OVLT neurons may receive ascending neural signals from peripheral blood pressure sensors (baroreceptors). Thus, SFO and OVLT neurons are poised to integrate signals about plasma osmolarity, volume and pressure and to use this

information to control thirst. The third component of the LT is the median preoptic nucleus (MnPO), which cannot access the blood directly and is thought to be an integratory center[11]. Together, these three structures form a forebrain hub for the regulation of fluid balance.

Signals detected in the SFO and OVLT are shared with each other and the MnPO through an extensive network of bidirectional projections[12–14]. Activation of this network triggers a coordinated set of homeostatic responses that restores fluid balance. These responses include: behavioral mechanisms that motivate water and sodium consumption (that is, thirst and salt appetite)[6,15,16]; autonomic mechanisms that modulate sympathetic outflow and thereby alter blood pressure and heart rate[17,18]; and neuroendocrine mechanisms that modulate water and sodium retention by the kidneys[19,20]. The neuroendocrine responses are mediated primarily by the hormones vasopressin and, in rodents but not in humans, oxytocin, both of which are secreted into the circulation by specialized posterior pituitary-projecting magnocellular neurosecretory cells in the paraventricular (PVH) and supraoptic (SON) nuclei of the hypothalamus that are under direct control of descending input from the LT[21,22].

Historically, the study of thirst and the LT has focused almost exclusively on the role of negative feedback signals like plasma osmolarity and angiotensin. However, most natural drinking behavior is regulated too rapidly to be controlled by blood composition directly and instead appears to anticipate homeostatic perturbations before they arise. For example, drinking satiates thirst long before ingested water enters the bloodstream to ultimately restore fluid homeostasis[23]. Similarly, animals tightly coordinate eating and drinking in order to ensure that adequate water is available for chewing, swallowing and digesting food and to counteract the effects of salt absorption into the bloodstream[24]. While these behavioral observations highlight the physiological importance of ‘anticipatory’ thirst regulation, the underlying neural mechanisms remain almost completely unknown.

Although the importance of the LT in the control of drinking has been appreciated for decades, our understanding of the underlying neural circuitry remains limited. For example, we still do not know the genetic identity of most of the cell types that reside in the LT; the dynamics of those cells during behavior; or the anatomical pathways by which they transmit information to other brain regions. This knowledge gap reflects, in part, the complexity of the LT, which contains a diversity of intermingled neural cell types distributed across three small nuclei. Although these features have traditionally made the thirst circuit challenging to dissect, the recent application of genetically targeted techniques[25,26] in mice has led to renewed progress.

## OVERVIEW OF THE DISSERTATION

This chapter has reviewed our historical understanding of thirst and fluid homeostasis[27]. Chapter two describes the first *in vivo* recordings of thirst neuron activity during behavior[28], which unexpectedly revealed that these cells—historically viewed as merely passive sensors of blood composition—also integrate sensory information from the oropharynx and gastrointestinal tract to predict the homeostatic consequences of eating and drinking. Chapter three describes the motivational mechanism underlying thirst[29]. Chapter four describes a new mode of gut–brain communication that regulates thirst satiation[30]. Together, these experiments have revealed fundamental organizing principles by which the brain monitors the state of the body in order to dynamically control ingestive behavior and maintain physiological homeostasis.

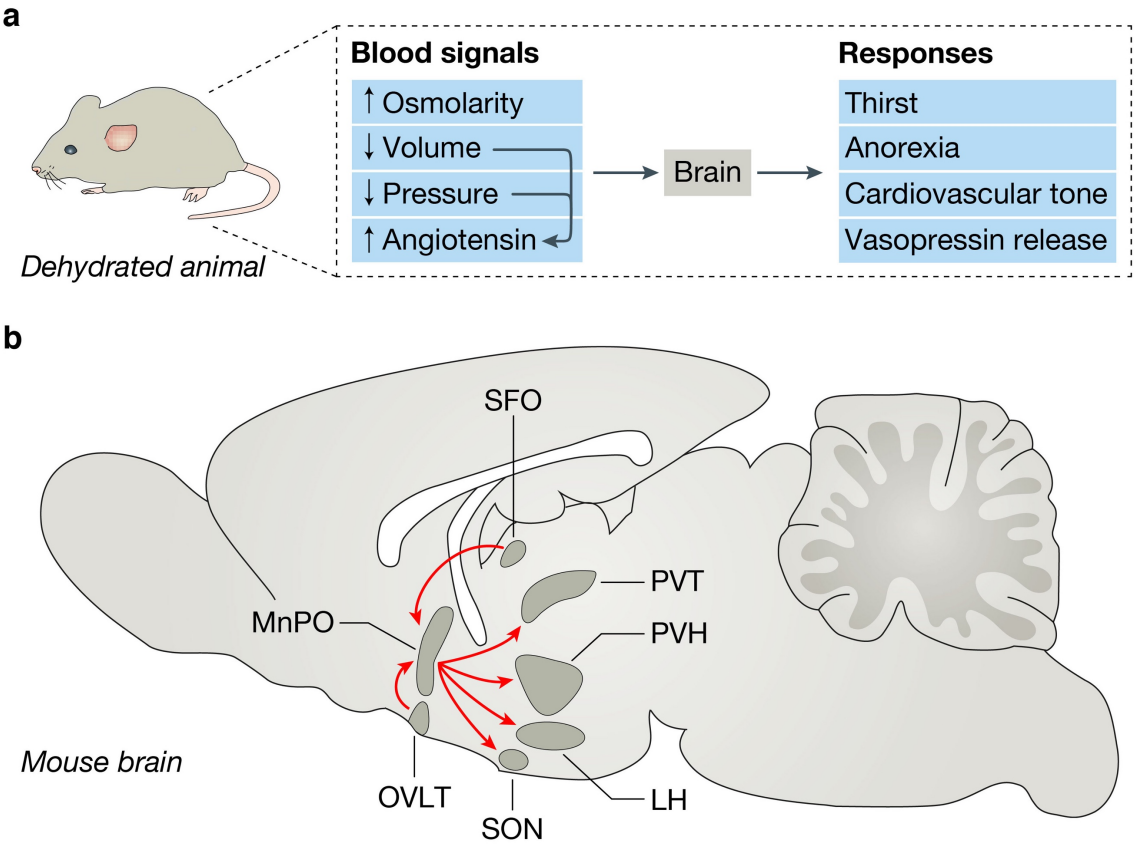


**c**

| Downstream brain region | LT inputs | Functions |
|---|---|---|
| Supraoptic nucleus (SON) | SFO, OVLT, MnPO | Vasopressin release |
| Paraventricular hypothalamus (PVH) | SFO, OVLT, MnPO | Thirst<br>Cardiovascular tone<br>Vasopressin release |
| Lateral hypothalamus (LH) | MnPO | Thirst<br>Cardiovascular tone |
| Paraventricular thalamus (PVT) | MnPO | Thirst |
| Bed nucleus of the stria terminalis (BNST) | SFO | Salt appetite |
| Dorsomedial hypothalamus (DMH) | MnPO | ? |
| Arcuate nucleus (ARC) | MnPO | ? |

**Figure 1.1 | Neural circuits underlying thirst and fluid homeostasis.**
**a**, Illustration of the body's response to dehydration. **b**, Simplified sagittal representation of the brain's thirst circuit. **c**, Summary of downstream brain regions innervated by LT thirst neurons. Panels **a** and **b** are adapted from ref. 27.

## REFERENCES


1 Cannon, W. B. Croonian Lecture—The physiological basis of thirst. *Proc. R. Soc. B Biol. Sci.* **90**, 283–301 (1918).

2 Fitzsimons, J. T. Angiotensin, thirst, and sodium appetite. *Physiol. Rev.* **78**, 583–686 (1998).

3 Bourque, C. W. Central mechanisms of osmosensation and systemic osmoregulation. *Nat. Rev. Neurosci.* **9**, 519–531 (2008).

4 Andersson, B. The effect of injections of hypertonic NaCl-solutions into different parts of the hypothalamus of goats. *Acta Physiol. Scand.* **28**, 188–201 (1953).

5 Epstein, A. N., Fitzsimons, J. T. & Rolls, B. J. Drinking induced by injection of angiotensin into the brain of the rat. *J. Physiol.* **210**, 457–474 (1970).

6 Simpson, J. B. & Routtenberg, A. Subfornical organ: site of drinking elicitation by angiotensin II. *Science* **181**, 1172–1175 (1973).

7 Buggy, J. & Jonhson, A. K. Preoptic-hypothalamic periventricular lesions: thirst deficits and hypernatremia. *Am. J. Physiol. Regul. Integr. Comp. Physiol.* **233**, R44–R52 (1977).

8 McKinley, M. J., Denton, D. A. & Weisinger, R. S. Sensors for antidiuresis and thirst—osmoreceptors or CSF sodium detectors? *Brain Res.* **141**, 89–103 (1978).

9 Thrasher, T. N., Keil, L. C. & Ramsay, D. J. Lesions of the organum vasculosum of the lamina terminalis (OVLT) attenuate osmotically-induced drinking and vasopressin secretion in the dog. *Endocrinology* **110**, 1837–1839 (1982).

10 McKinley, M. J. *et al.* The sensory circumventricular organs of the mammalian brain. *Adv. Anat. Embryol. Cell Biol.* **172**, 1–127 (2003).

11 McKinley, M. J. *et al.* The median preoptic nucleus: front and centre for the regulation of body fluid, sodium, temperature, sleep and cardiovascular homeostasis. *Acta Physiol.* **214**, 8–32 (2015).

12 Swanson, L. W. An autoradiographic study of the efferent connections of the preoptic region in the rat. *J. Comp. Neurol.* **167**, 227–256 (1976).

13 Miselis, R. R., Shapiro, R. E. & Hand, P. J. Subfornical organ efferents to neural systems for control of body water. *Science* **205**, 1022–1025 (1979).

14 Lind, R. W., van Hoesen, G. W. & Johnson, A. K. An HRP study of the connections of the subfornical organ of the rat. *J. Comp. Neurol.* **210**, 265–277 (1982).

15 Fluharty, S. J. & Epstein, A. N. Sodium appetite elicited by intracerebroventricular infusion of angiotensin II in the rat: II. Synergistic interaction with systemic mineralocorticoids. *Behav. Neurosci.* **97**, 746–758 (1983).

16 Robertson, A., Kucharczyk, J. & Mogenson, G. J. Drinking behavior following electrical stimulation of the subfornical organ in the rat. *Brain Res.* **274**, 197–200 (1983).

17 Mangiapane, M. L. & Simpson, J. B. Subfornical organ: forebrain site of pressor and dipsogenic action of angiotensin II. *Am. J. Physiol. Regul. Integr. Comp. Physiol.* **239**, R382–R389 (1980).

18 Ishibashi, S. & Nicolaïdis, S. Hypertension induced by electrical stimulation of the subfornical organ (SFO). *Brain Res. Bull.* **6**, 135–139 (1981).

19 Ferguson, A. V. & Kasting, N. W. Electrical stimulation in subfornical organ increases plasma vasopressin concentrations in the conscious rat. *Am. J. Physiol. Regul. Integr. Comp. Physiol.* **251**, R425–R428 (1986).

20 Ferguson, A. V. & Kasting, N. W. Activation of subfornical organ efferents stimulates oxytocin secretion in the rat. *Regul. Pept.* **18**, 93–100 (1987).

21 Verney, E. B. Croonian Lecture—The antidiuretic hormone and the factors which determine its release. *Proc. R. Soc. B Biol. Sci.* **135**, 25–106 (1947).

22 Antunes-Rodrigues, J., de Castro, M., Elias, L. L. K., Valença, M. M. & McCann, S. M. Neuroendocrine control of body fluid metabolism. *Physiol. Rev.* **84**, 169–208 (2004).

23 Bellows, R. T. Time factors in water drinking in dogs. *Am. J. Physiol.* **125**, 87–97 (1938).

24 Fitzsimons, J. T. & Le Magnen, J. Eating as a regulatory control of drinking in the rat. *J. Comp. Physiol. Psychol.* **67**, 273–283 (1969).

25 Zeng, H. & Sanes, J. R. Neuronal cell-type classification: challenges, opportunities and the path forward. *Nat. Rev. Neurosci.* **18**, 530–546 (2017).

26 Luo, L., Callaway, E. M. & Svoboda, K. Genetic dissection of neural circuits: a decade of progress. *Neuron* **98**, 256–281 (2018).

27 Zimmerman, C. A., Leib, D. E. & Knight, Z. A. Neural circuits underlying thirst and fluid homeostasis. *Nat. Rev. Neurosci.* **18**, 459–469 (2017).

28 Zimmerman, C. A. *et al.* Thirst neurons anticipate the homeostatic consequences of eating and drinking. *Nature* **537**, 680–684 (2016).

29 Leib, D. E. *et al.* The forebrain thirst circuit drives drinking through negative reinforcement. *Neuron* **96**, 1272–1281 (2017).

30 Zimmerman, C. A. *et al.* A gut-to-brain signal of fluid osmolarity controls thirst satiation. *Nature* **568**, 98–102 (2019).

*II. Thirst neurons anticipate the homeostatic consequences of eating and drinking*

---

The material in this chapter is reprinted from:

> Christopher A. Zimmerman, Yen-Chu Lin, David E. Leib, Ling Guo, Erica L. Huey, Gwendolyn E. Daly, Yiming Chen, Zachary A. Knight. Thirst neurons anticipate the homeostatic consequences of eating and drinking. *Nature* 537, 680–684, 2016.

C.A.Z. and Z.A.K. conceived the project and designed the experiments. C.A.Z., Y.-C.L., D.E.L., L.G., E.L.H., G.E.D. and Y.C. performed stereotaxic surgery and histology. Y.-C.L. conducted acute slice experiments. C.A.Z. and Y.C. conducted photometry experiments. C.A.Z. conducted optogenetics experiments. C.A.Z. and D.E.L. conducted plasma composition experiments. Y.C. generated the synaptophysin-GCaMP6s construct. C.A.Z., Y.-C.L., Y.C. and Z.A.K. analyzed the data. C.A.Z. and Z.A.K. prepared the manuscript with input from all authors.

## ABSTRACT

Thirst motivates animals to drink in order to maintain fluid balance. Thirst has conventionally been viewed as a homeostatic response to changes in blood volume or tonicity[1–3]. However, most drinking behaviour is regulated too rapidly to be controlled by blood composition directly, and instead seems to anticipate homeostatic imbalances before they arise[4–11]. How this is achieved remains unknown. Here we reveal an unexpected role for the subfornical organ (SFO) in the anticipatory regulation of thirst in mice. By monitoring deep-brain calcium dynamics, we show that thirst-promoting SFO neurons respond to inputs from the oral cavity during eating and drinking and then integrate these inputs with information about the composition of the blood. This integration allows SFO neurons to predict how ongoing food and water consumption will alter fluid balance in the future and then to adjust behaviour pre-emptively. Complementary optogenetic manipulations show that this anticipatory modulation is necessary for drinking in several contexts. These findings provide a neural mechanism to explain longstanding behavioural observations, including the prevalence of drinking during meals[10,11], the rapid satiation of thirst[7–9], and the fact that oral cooling is thirst-quenching[12–14].

## INTRODUCTION

Deviations of blood volume or osmolarity from their set points are detected by specialized neurons within the circumventricular organs (CVOs) of the brain[1–3]. Activation of these neurons generates thirst, which motivates animals to find and consume water and thereby restore fluid balance.

Nevertheless, many aspects of drinking behaviour cannot be explained by this textbook homeostatic model[15] because their regulation precedes rather than responds to changes in the blood[4–11]. For example, drinking quenches thirst tens of minutes before ingested water reaches the circulation and alters the composition of the blood, indicating that thirst is sated before

homeostasis is restored. Yet animals somehow calibrate their water consumption to match their physiological need precisely[7–9]. Conversely, most drinking occurs during meals, as a result of prandial thirst that develops long before the ingested food has been absorbed and altered the blood tonicity[10,11]. These observations indicate that much normal drinking behaviour is anticipatory in nature, meaning that the brain predicts impending changes in fluid balance and adjusts behaviour pre-emptively. How this is achieved remains unknown.

The CVOs are the brain regions most strongly associated with fluid balance[1–3]. Functional MRI (fMRI) studies failed to detect rapid modulation of these structures during drinking[16,17], leading to the idea that the integratory circuits for thirst reside in higher brain centres[3,18] and that the CVOs function only as passive sensors of blood composition[1–3]. However, this conclusion is complicated by the fact that the CVOs contain a diversity of intermingled neural cell types[19,20], which cannot be discriminated by functional imaging. Importantly, current models for the thirst circuitry have never been tested by recording the dynamics of identified neurons in awake, behaving animals.

## RESULTS

To investigate thirst circuits *in vivo*, we focused on the SFO, a CVO that is strongly implicated in the control of drinking behaviour[21]. Optogenetic activation of SFO excitatory neurons expressing nitric oxide synthase 1 (*Nos1*) promotes voracious drinking in water-sated mice[19,22]. We replicated this (Figure 2.6) and then targeted the calcium indicator GCaMP6s to $SFO^{Nos1}$ neurons for calcium imaging. We first confirmed in slice that GCaMP6s reported $SFO^{Nos1}$ neuron activity induced by current injection or application of angiotensin (Figure 2.7). We then installed fibre optics above the SFO for recordings of population activity by fibre photometry[23] in awake, behaving mice (Figure 2.1a).

To define the regulation of $SFO^{Nos1}$ neurons *in vivo*, we recorded GCaMP fluorescence responses to a series of systemic challenges[24]. Peripheral injection of angiotensin (Figure 2.8) or hypertonic saline (Figure 2.1b) rapidly and dose-dependently activated $SFO^{Nos1}$ neurons. The response to hypertonic saline was mediated by an osmosensory (rather than sodium-sensory) mechanism, because injection of equiosmotic concentrations of mannitol[25] induced a similar response (Figure 2.1d). Challenge with polyethylene glycol (PEG), which induces hypovolaemia[26], or isoproterenol, which induces hypotension[24], resulted in slower and more sustained activation of $SFO^{Nos1}$ neurons (Figure 2.1e, g). The responses to PEG and isoproterenol were abolished by pre-treatment with angiotensin blockers (Figure 2.1f, h), whereas the response to osmotic challenge was unaffected (Figure 2.1c). Thus, $SFO^{Nos1}$ neurons sense the osmolarity, volume and pressure of the blood via a combination of angiotensin-dependent and -independent mechanisms (Figure 2.1i, Figure 2.8).

Consistent with this homeostatic regulation, overnight water restriction strongly activated $SFO^{Nos1}$ neurons (Figure 2.2a). When water was made available, mice drank avidly and, surprisingly, $SFO^{Nos1}$ neurons were inhibited within 1 min (Figure 2.2b–d). This inhibition was time-locked to the act of drinking, with activity beginning to decline the moment of the first lick (Figure 2.2g) and stabilizing whenever drinking was paused. Drinking continued until the precise moment at which $SFO^{Nos1}$ neuron activity returned to baseline, at which point drinking terminated. These responses were much too fast to be mediated by changes in the blood, which we confirmed directly by measuring plasma volume and osmolarity along a time-course of rehydration (Figure 2.2e, f). Thus, contrary to current models, thirst is not quenched by the reverse of the process that generates it[1–3]. Instead, drinking resets thirst-promoting SFO neurons in a way that anticipates the future restoration of homeostasis. Importantly, this anticipatory feedback provides a mechanism to explain how animals can match ongoing water consumption

to the level of physiological need, a longstanding observation that has lacked a clear neural basis[7–9].

To investigate whether this rapid inhibition of $SFO^{Nos1}$ neurons is sufficient to explain thirst satiation, we used optogenetic silencing to replay this inhibition in thirsty animals. Of note, previous studies found that SFO ablation does not completely block drinking[1], but interpretation of these lesion experiments is complicated by the fact that the SFO contains intermingled thirst-driving and -suppressing cell types[19,20]. We targeted the inhibitory opsin eArch3.0 to $SFO^{Nos1}$ neurons (Figure 2.2h) and confirmed that this can silence $SFO^{Nos1}$ neurons *ex vivo* (Figure 2.9). We then water-restricted mice overnight and measured subsequent drinking behaviour. Notably, silencing $SFO^{Nos1}$ neurons abolished drinking in dehydrated animals (Figure 2.2i–j, Figure 2.9). This effect was rapidly reversible, as mice engaged in voracious drinking soon after silencing was terminated (latency to first lick 113 ± 17 s; mean ± s.e.m.). It was also specific to drinking, as silencing did not inhibit food intake after fasting (Figure 2.12). Thus, $SFO^{Nos1}$ neurons are necessary for water consumption, and, importantly, their rapid inhibition during drinking is sufficient to explain thirst satiation.

We sought to clarify the mechanism of rapid feedback to $SFO^{Nos1}$ neurons during drinking. $SFO^{Nos1}$ neuron activity was unaffected by allowing mice to see but not consume water (Figure 2.3e, f) or by presenting sensory cues that had been paired with water access via Pavlovian conditioning (Figure 2.10). $SFO^{Nos1}$ neurons are therefore not inhibited by the expectation of water availability alone, in contrast to $ARC^{AgRP}$ neurons that control hunger[22,27,28]. Similarly, the act of licking per se was insufficient, since $SFO^{Nos1}$ neuron activity was not reduced in mice that performed several hundred ‘air licks’ after presentation of an empty water bottle (Figure 2.3g, h). This indicates that a signal tightly linked to the act of water ingestion itself, such as the sensation of liquid in the oral cavity, inhibits $SFO^{Nos1}$ neurons.

To investigate this further, we tested whether drinking would inhibit $SFO^{Nos1}$ neurons if the ingested liquid could not restore homeostasis. Mice were salt-challenged and then provided with access to water or hypertonic saline. Water consumption rapidly inhibited $SFO^{Nos1}$ neurons (Figure 2.3a–c, Figure 2.10), and this inhibition preceded any change in plasma osmolarity (Figure 2.3d). Notably, consumption of hypertonic saline also rapidly inhibited $SFO^{Nos1}$ neurons, with kinetics initially indistinguishable from water consumption (Figure 2.3i, j). However, this initial decline was reversed after approximately 1 min. This indicates that the rapid anticipatory response to drinking has at least two components: an immediate signal that tracks fluid ingestion, and a delayed signal that reports on fluid tonicity, possibly generated by an oesophageal or gastric osmosensor.

To probe the oropharyngeal signals that regulate $SFO^{Nos1}$ neurons further, we investigated the role of water temperature. Humans experience cold drinks as more thirst-quenching[14], and a similar preference is observed in rodents[12,13]. To test whether $SFO^{Nos1}$ neurons contribute to this effect, we presented thirsty mice with access to water of different temperatures. We found that, regardless of temperature, mice consumed enough water to reduce the activity of their $SFO^{Nos1}$ neurons to baseline (Figure 2.3k). However, the reduction in $SFO^{Nos1}$ neuron activity per lick was strongly temperature-dependent, with cold water inducing the largest decrease per lick and warm water the smallest (Figure 2.3l). This suggests that the temperature dependence of thirst-quenching may be encoded in $SFO^{Nos1}$ neuron activity. To test this directly, we measured the isolated effect of oral cooling on these neurons. We found that applying cold, but not room temperature, metal to the oral cavity of awake, thirsty mice was sufficient to inhibit $SFO^{Nos1}$ neurons rapidly (Figure 2.3m, n). Thus, temperature-dependent modulation of $SFO^{Nos1}$ neurons may explain the enigmatic connection between oral cooling and thirst, including why thirsty rodents will avidly lick cold metal[29] and humans report that sucking on ice chips rapidly relieves thirst[14].

Eating is a potent stimulus for thirst, and many animals drink primarily during meals. However, the neural basis for prandial thirst is unknown, partly because feeding stimulates drinking before any change in the blood occurs[10,11]. To investigate the role of $SFO^{Nos1}$ neurons, we fasted mice overnight and then provided them with access to food but not water. Remarkably, food consumption rapidly activated $SFO^{Nos1}$ neurons, beginning at the onset of feeding and plateauing within 15 min (Figure 2.4a). When water was presented, mice drank avidly and $SFO^{Nos1}$ neurons were quickly inhibited. A similar activity pattern was observed when hungry mice were given simultaneous access to food and water (Figure 2.4c). Activation of $SFO^{Nos1}$ neurons during eating was not caused by changes in blood composition, because activation was complete before plasma osmolarity increased (Figure 2.4b) and was unaffected by angiotensin blockers (Figure 2.11). Importantly, silencing $SFO^{Nos1}$ neurons during these same protocols greatly reduced meal-associated water consumption (Figure 2.4d, e) but not food intake (Figure 2.12), indicating that $SFO^{Nos1}$ neurons are specifically necessary for prandial drinking. Thus, modulation of $SFO^{Nos1}$ neurons during feeding provides a mechanism to explain the coordination of eating and drinking, a widespread phenomenon that has lacked a clear neural substrate.

To understand better the circuit mechanisms underlying the regulation of drinking by $SFO^{Nos1}$ neurons, we investigated the inputs and outputs of these cells. Projection mapping revealed that $SFO^{Nos1}$ neurons densely innervate several hypothalamic nuclei associated with fluid balance[30] (Figure 2.13). Optogenetic stimulation of projections to the median preoptic nucleus (MnPO), but not the paraventricular hypothalamus (PVH), was sufficient to drive voracious drinking (Figure 2.5a–c). Notably, examination of the monosynaptic inputs to $SFO^{Nos1}$ neurons by retrograde rabies tracing revealed a partially overlapping set of structures (Figure 2.5d–f, Figure 2.13). Determination of the cell-type-specific connectivity between these structures will be an important area for future investigation.

## DISCUSSION

Ingestive behaviour is regulated by a combination of anticipatory and homeostatic cues[4–6]. Interoceptive neurons within the CVOs have been recognized for decades as crucial sites for the homeostatic regulation of drinking[1–3,21,24,26]. By contrast, the neural substrates for the anticipatory regulation of drinking have remained obscure, despite abundant evidence that such mechanisms are important for the control of behaviour[4–11]. Here we have demonstrated that the anticipatory signals for thirst unexpectedly converge on the same homeostatic neurons that monitor the composition of the blood (Figure 2.14). This convergence provides a straightforward mechanism for the brain to compare the needs of the body with the anticipated effects of ongoing food and water consumption and then adjust behaviour pre-emptively. This in turn explains longstanding behavioural observations, including the speed of thirst satiation (Figure 2.2), the fact that oral cooling is thirst-quenching (Figure 2.3), and the widespread coordination of eating and drinking (Figure 2.4). These findings reveal that the CVOs, long viewed as merely passive sensors of the blood, receive a second class of anticipatory signals that enable their dynamic regulation of behaviour.

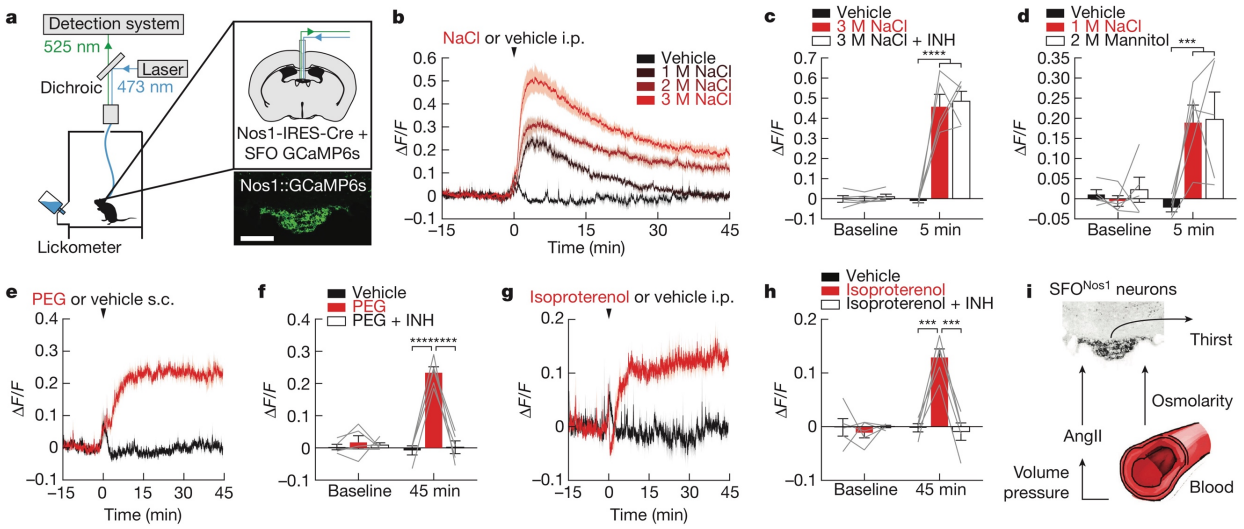


**Figure 2.1 | Mechanisms of homeostatic regulation of SFO$^{Nos1}$ neurons.**
**a**, Schematic of fibre photometry set up. Scale bar, 100 μm. **b**, SFO$^{Nos1}$ neurons are activated by injection of NaCl. i.p., intraperitoneal. **c**, Angiotensin blockers (INH) do not abolish the response to NaCl. **d**, SFO$^{Nos1}$ neurons are similarly activated by equiosmotic concentrations of mannitol and NaCl. **e**, SFO$^{Nos1}$ neurons are activated by injection of PEG. s.c., subcutaneous. **f**, Angiotensin blockers abolish this response. **g**, SFO$^{Nos1}$ neurons are activated by injection of isoproterenol. **h**, Angiotensin blockers abolish this response. **i**, Schematic summarizing the mechanisms by which SFO$^{Nos1}$ neurons monitor the blood. AngII, angiotensin II. All error bars and shaded areas represent mean ± s.e.m. Statistical analyses are described in Methods. *n* = 5 mice for all experiments.

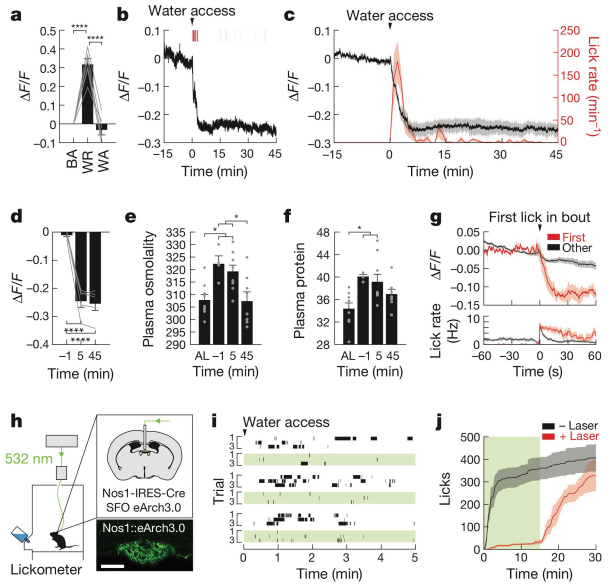


**Figure 2.2 | SFO$^{Nos1}$ neurons receive rapid anticipatory modulation and are necessary for drinking.**

**a**, SFO$^{Nos1}$ neurons are activated by water restriction (WR), and their activity returns to baseline (BA) after water access (WA) (*n* = 6 mice). **b**, Representative recording showing rapid inhibition of SFO$^{Nos1}$ neurons during drinking after water restriction (1 out of 5 mice; red lines, licks; red boxes, bouts). **c**, Averaged traces showing SFO$^{Nos1}$ neuron activity and lick rate (*n* = 5 mice). **d**, Quantification (*n* = 5 mice). **e**, Plasma osmolality (mOsm kg$^{-1}$) is increased by water restriction and is unchanged by 5 min after re-access (*n* = 9 [AL], 4 [–1], 9 [5], 8 [45] mice per group). AL, ad libitum. **f**, Plasma protein concentration (mg ml$^{-1}$) is increased by water restriction and is unchanged by 5 min after re-access (*n* = 9 [AL], 4 [–1], 9 [5], 8 [45] mice per group). **g**, Peristimulus time histogram (PSTH) around first lick in first bout or all other bouts (*n* = 5 mice). **h**, Schematic of optogenetic set up for silencing SFO$^{Nos1}$ neurons. Scale bar, 100 μm. **i**, Representative rasters of drinking after water restriction (3 out of 5 mice; black lines, licks; green boxes, laser on). **j**, Averaged traces showing cumulative licks following water restriction (*n* = 5 mice; green box, laser on). All error bars and shaded areas represent mean ± s.e.m. Statistical analyses are described in Methods.

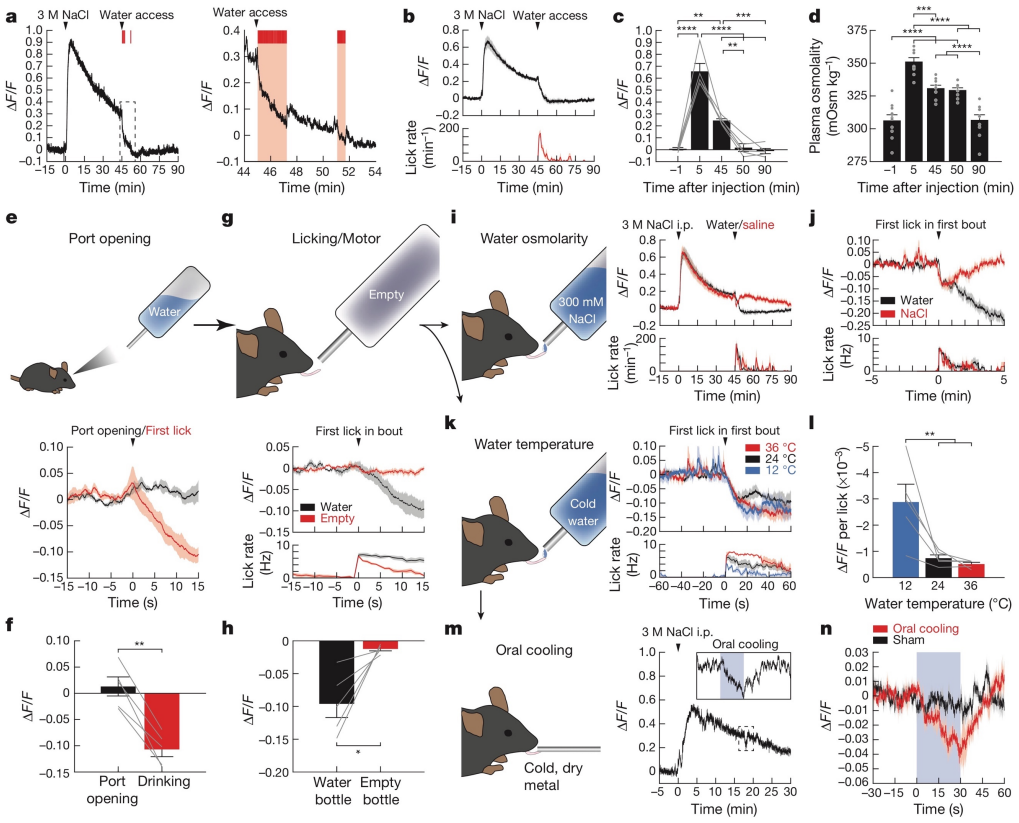


**Figure 2.3 | Mechanisms of anticipatory regulation of SFO$^{Nos1}$ neurons.**
**a**, Representative recording showing rapid inhibition of SFO$^{Nos1}$ neurons during drinking after salt challenge (1 out of 8 mice; red lines, licks; red boxes, bouts). **b**, Averaged traces showing SFO$^{Nos1}$ neuron activity and lick rate. **c**, Quantification. **d**, Plasma osmolality is increased by salt challenge and is unchanged by 5 min after water re-access ($n$ = 10 mice per group). **e**, SFO$^{Nos1}$ neurons do not respond to the sight of water. **f**, Quantification. **g**, SFO$^{Nos1}$ neurons do not respond to motor movements associated with licking. **h**, Quantification. **i**, SFO$^{Nos1}$ neurons receive a post-ingestive error signal that reports the osmolarity of ingested fluids. **j**, PSTH around first lick in first bout. **k**, SFO$^{Nos1}$ neurons were similarly inhibited regardless of water temperature. **l**, Drop in activity per lick was highly temperature-dependent. **m**, Representative recording showing rapid inhibition of SFO$^{Nos1}$ neurons during oral cooling (1 out of 5 mice; blue box, oral cooling). **n**, PSTH around placement of dry metal into oral cavity. All error bars and shaded areas represent mean ± s.e.m. Statistical analyses are described in Methods. $n$ = 5 mice for all photometry experiments.

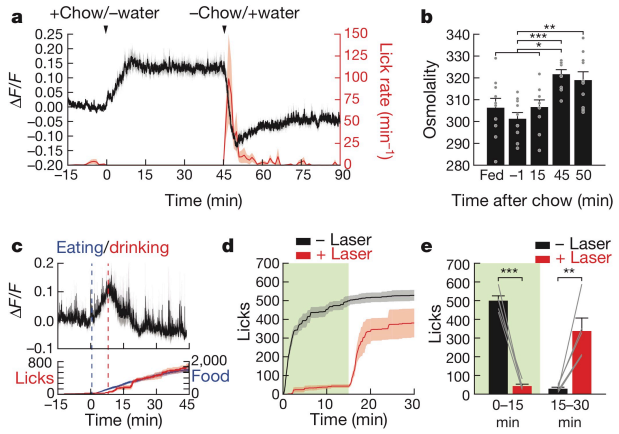


**Figure 2.4 | SFO$^{Nos1}$ neurons are activated by eating and are required for prandial thirst.** **a**, SFO$^{Nos1}$ neurons are rapidly activated by eating and inhibited by prandial drinking after overnight fasting ($n$ = 6 mice). **b**, Plasma osmolality is increased by eating by 45 min (but not 15 min) after chow access, and is unchanged by 5 min after water re-access ($n$ = 10 mice per group). **c**, SFO$^{Nos1}$ neurons are rapidly modulated in fasted mice provided with simultaneous access to chow and water ($n$ = 5 mice). Food refers to time (s) spent interacting with food. **d**, Silencing SFO$^{Nos1}$ neurons abolishes prandial thirst in fasted mice re-fed chow before water access ($n$ = 5 mice; green box, laser on). **e**, Quantification ($n$ = 5 mice). All error bars and shaded areas represent mean ± s.e.m. Statistical analyses are described in Methods.

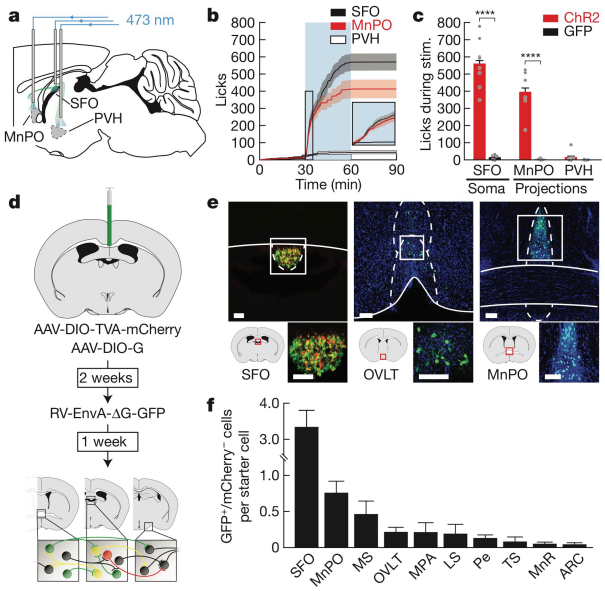


**Figure 2.5 | Structure of the SFO$^{Nos1}$ neuron-associated thirst circuit.**
**a**, Schematic of optogenetic set up for activating SFO$^{Nos1}$ neuron somas or axon terminals in the MnPO or PVH. **b**, Averaged traces showing cumulative licks during photostimulation ($n$ = 8 [SFO$^{ChR2}$], 6 [MnPO$^{ChR2}$], 7 [PVH$^{ChR2}$] mice per group). **c**, Quantification ($n$ = 8 [SFO$^{ChR2}$], 5 [SFO$^{GFP}$], 6 [MnPO$^{ChR2}$], 4 [MnPO$^{GFP}$], 7 [PVH$^{ChR2}$], 4 [PVH$^{GFP}$] mice per group). ChR2, channelrhodopsin-2. **d**, Schematic of viral strategy for identifying monosynaptic inputs to SFO$^{Nos1}$ neurons. AAV, adeno-associated virus; RV, rabies virus. **e**, Representative images showing SFO injection site (red, mCherry; green, green fluorescent protein; GFP) and monosynaptically connected neurons (green, GFP; blue, DAPI) in the organum vasculosum of the lamina terminalis (OVLT) and MnPO (1 out of 6 mice). Scale bars, 100 μm. **f**, Quantification ($n$ = 6 mice). ARC, arcuate nucleus; LS, lateral septum; MPA, medial preoptic area; MnR, median raphe; MS, medial septum; Pe, periventricular hypothalamus; TS, triangular septum. All error bars and shaded areas represent mean ± s.e.m. Statistical analyses are described in Methods.

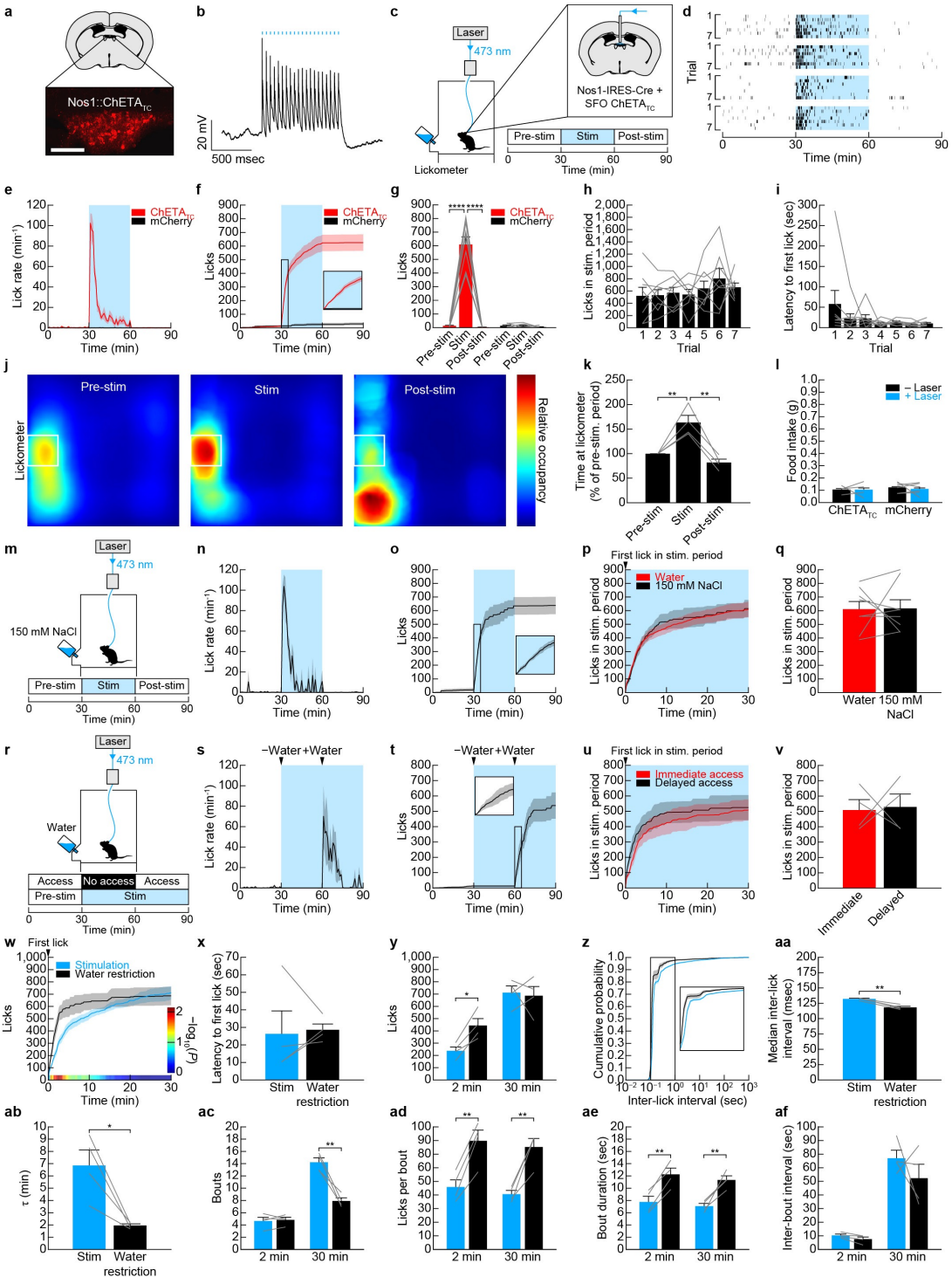


**Figure 2.6 | Optogenetic activation of SFO$^{Nos1}$ neurons is sufficient to promote drinking, but negative feedback inhibits excessive drinking during optogenetically and dehydration-induced drinking.**

**a**–**l**, Optogenetic activation of SFO$^{Nos1}$ neurons rapidly and specifically promotes drinking. **a**, Expression of mCherry in SFO$^{Nos1}$ neurons from AAV5-EF1α-DIO-ChETA$_{TC}$-2A-mCherry. Scale bar, 100 μm. **b**, Representative recording showing rapid firing of SFO$^{Nos1}$ neuron in response to

photostimulation (20 Hz) in acute slice (1 out of 3 cells; blue lines, stimulation). **c**, Schematic of optogenetic set up for activating $SFO^{Nos1}$ neurons. **d**, Rasters of drinking in response to optogenetic stimulation for seven trials each for four $SFO^{Nos1}$::$ChETA_{TC}$ mice (black lines, licks; blue boxes, stimulation). **e**, Averaged traces showing lick rate ($n$ = 6 $SFO^{Nos1}$::mCherry mice and 8 $SFO^{Nos1}$::$ChETA_{TC}$ mice). **f**, Averaged traces showing cumulative licks ($n$ = 6 $SFO^{Nos1}$::mCherry mice and 8 $SFO^{Nos1}$::$ChETA_{TC}$ mice). **g**, Quantification of drinking during stimulation protocol (****$P$ < 0.0001, two-way repeated-measures ANOVA, $n$ = 6 $SFO^{Nos1}$::mCherry mice and 8 $SFO^{Nos1}$::$ChETA_{TC}$ mice). **h**, Licks during stimulation period across seven consecutive trials (not significant (n.s.), one-way repeated-measures ANOVA, $n$ = 8 mice). **i**, Latency to first lick during stimulation period across seven consecutive trials (n.s., one-way repeated-measures ANOVA, $n$ = 8 mice). **j**, Heat maps showing location of $SFO^{Nos1}$::$ChETA_{TC}$ mice during stimulation protocol ($n$ = 4 mice). **k**, Quantification of time spent at lickometer during stimulation protocol (**$P$ < 0.01, one-way repeated-measures ANOVA, $n$ = 4 mice). **l**, Activation of $SFO^{Nos1}$ neurons did not induce feeding (n.s., two-way repeated-measures ANOVA, $n$ = 6 $SFO^{Nos1}$::mCherry mice and 4 $SFO^{Nos1}$::$ChETA_{TC}$ mice). Panels **m**–**q** show that osmotic dilution does not inhibit excessive drinking during optogenetically induced drinking. **m**, $SFO^{Nos1}$::$ChETA_{TC}$ mice were stimulated, but with access to 150 mM NaCl instead of water. **n**, Lick rate ($n$ = 8 mice). **o**, Cumulative licks ($n$ = 8 mice). **p**, Comparison to stimulation with water access ($n$ = 8 mice). **q**, Quantification (n.s., two-tailed Student's $t$-test, $n$ = 8 mice). Panels **r**–**v** show that channelrhodopsin failure does not explain the negative feedback that inhibits excessive drinking during optogenetically induced drinking. **r**, $SFO^{Nos1}$::$ChETA_{TC}$ mice were stimulated, but with delayed access to water instead of immediate access. **s**, Lick rate ($n$ = 4 mice). **t**, Cumulative licks ($n$ = 4 mice). **u**, Comparison to stimulation with water access ($n$ = 4 mice). **v**, Quantification (n.s., two-tailed Student's $t$-test, $n$ = 4 mice). Panels **w**–**af** show that a negative feedback mechanism also inhibits excessive drinking during dehydration-induced drinking. **w**, Comparison of optogenetically and dehydration-induced drinking in $SFO^{Nos1}$::$ChETA_{TC}$ mice ($n$ = 4 mice; $P$ value colour bar represents independent two-tailed Student's $t$-tests). **x**, Latency to first lick (n.s., two-tailed Student's $t$-test, $n$ = 4 mice). **y**, Cumulative licks (*$P$ < 0.05, two- way repeated-measures ANOVA, $n$ = 4 mice). **z**, Cumulative probability distribution for inter-lick interval, a measure of licking 'speed' ($n$ = 4 mice). **aa**, Median inter-lick interval (**$P$ < 0.01, two-tailed Student's $t$-test, $n$ = 4 mice). **ab**, Time constant ($\tau$) for cumulative licks (*$P$ < 0.05, two-tailed Student's $t$-test, $n$ = 4 mice). **ac**, Number of drinking bouts (**$P$ < 0.01, two-way repeated-measures ANOVA, $n$ = 4 mice). **ad**, Number of licks per drinking bout (**$P$ < 0.01, two-way repeated- measures ANOVA, $n$ = 4 mice). **ae**, Bout duration (**$P$ < 0.01, two-way repeated-measures ANOVA, $n$ = 4 mice). **af**, Inter-bout interval (n.s., two- way repeated-measures ANOVA, $n$ = 4 mice). Values are mean ± s.e.m. (error bars or shaded area).

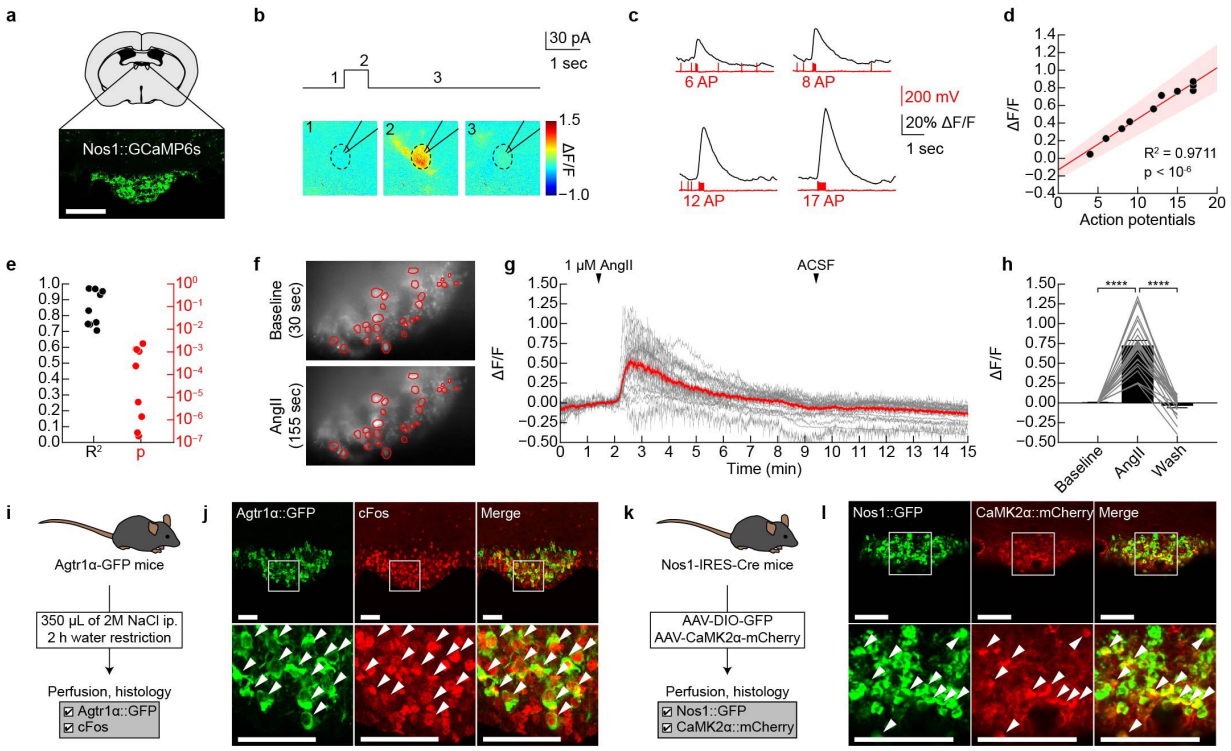


**Figure 2.7 | GCaMP6s accurately reports SFO$^{Nos1}$ neuron activity in acute slices.**
**a**, Expression of GCaMP6s in SFO$^{Nos1}$ neurons from AAV5-EF1α-FLEX-GCaMP6s. Scale bar, 100 μm. **b**, Representative fluorescence images of a neuron given a 30 pA current injection for 700 ms in acute slice (1 out of 9 cells). **c**, Representative traces showing calcium responses in response to 30 pA current injections of increasing duration to produce increasing numbers of action potentials (1 out of 9 cells). **d**, Relationship between number of action potentials and Δ*F*/*F* for the representative neuron in **c** (shaded area denotes 95% confidence interval). **e**, $R^2$ and *P* value for linear relationship between number of action potentials and Δ*F*/*F* (*n* = 9 cells). Panels **f–j** show that SFO$^{Nos1}$ neurons are homogeneously responsive to both angiotensin and salt challenge. **f**, Representative fluorescence images showing SFO$^{Nos1}$ neuron activity before and during bath application of angiotensin (1 out of 3 experiments; red circles, identified neurons). **g**, 24 out of 27 (~90%) identified SFO$^{Nos1}$ neurons were activated by bath application of angiotensin (red line, mean; grey lines, individual activated neurons). **h**, Quantification (****$P < 0.0001$, two-way repeated-measures ANOVA, $n = 24$ activated neurons). **i**, Experimental design to test whether a single population of SFO neurons is responsive to both angiotensin and salt challenge. **j**, Co-localization of Agtr1α::GFP and salt-challenge-induced cFos indicates that SFO$^{Nos1}$ neurons are homogeneously responsive to both angiotensin and salt challenge. Scale bars, 100 μm. **k**, Experimental design to test whether SFO neurons express the excitatory neuron marker CaMK2α. **l**, Co-localization of CaMK2α::mCherry and Nos1::GFP indicates that SFO$^{Nos1}$ neurons are excitatory. Scale bars, 100 μm. Values are mean ± s.e.m. (error bars or shaded area).

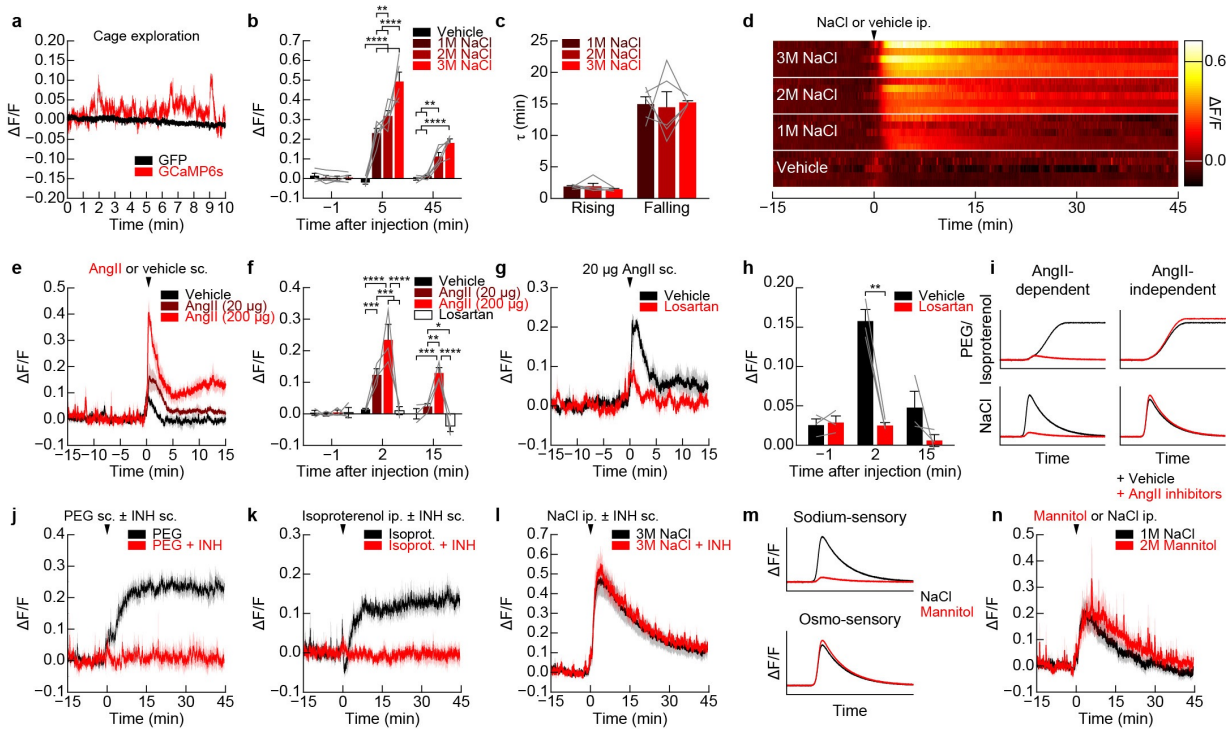


**Figure 2.8 | Regulation of SFO$^{Nos1}$ neurons by homeostatic signals.**
**a**, Recordings from SFO$^{Nos1}$::GCaMP6s mice as they explored a behavioural chamber without access to food or water revealed dynamic fluctuations in fluorescence around a stable baseline (1 out of 8 mice); these fluctuations were absent from recordings from SFO$^{Nos1}$::GFP mice (1 out of 3 mice). **b**, Quantification of response to peripheral injection of NaCl (averaged traces in Figure 2.1b; $^{**}P < 0.01$, $^{****}P < 0.0001$, two-way repeated-measures ANOVA, $n = 5$ mice). **c**, Time constant ($\tau$) of rising and falling phases of response to peripheral injection of NaCl (n.s., two-way repeated-measures ANOVA, $n = 5$ mice). **d**, Representative recordings for five mice showing response to peripheral injection of NaCl or vehicle. **e**, SFO$^{Nos1}$ neurons are activated by peripheral injection of angiotensin in a dose-dependent manner ($n = 3$ mice). **f**, Quantification ($^{*}P < 0.05$, $^{**}P < 0.01$, $^{***}P < 0.001$, $^{****}P < 0.0001$, two-way repeated- measures ANOVA, $n = 3$ mice). **g**, The $AT_1R$ antagonist losartan abolished the response to peripheral injection of angiotensin ($n = 3$ mice). **h**, Quantification ($^{**}P < 0.01$, two-way repeated-measures ANOVA, $n = 3$ mice). **i**, Schematic illustrating expected observations whether activation of SFO$^{Nos1}$ neurons in response to peripheral injection of PEG/isoproterenol and NaCl is angiotensin-dependent. **j**, Angiotensin blockers abolished the response to peripheral injection of PEG (quantification in Figure 2.1f; $n = 5$ mice). **k**, Angiotensin blockers abolished the response to peripheral injection of isoproterenol (quantification in Figure 2.1h; $n = 5$ mice). **l**, Angiotensin blockers did not abolish the response to peripheral injection of NaCl (quantification in Figure 2.1c; $n = 5$ mice). **m**, Schematic illustrating expected observations if activation of SFO$^{Nos1}$ neurons in response to peripheral injection of NaCl is sodium-sensory or osmosensory. **n**, SFO$^{Nos1}$ neurons are similarly activated by peripheral injection of equimolar concentrations of mannitol and NaCl (quantification in Figure 2.1d; $n = 5$ mice). Values are mean ± s.e.m. (error bars or shaded area).

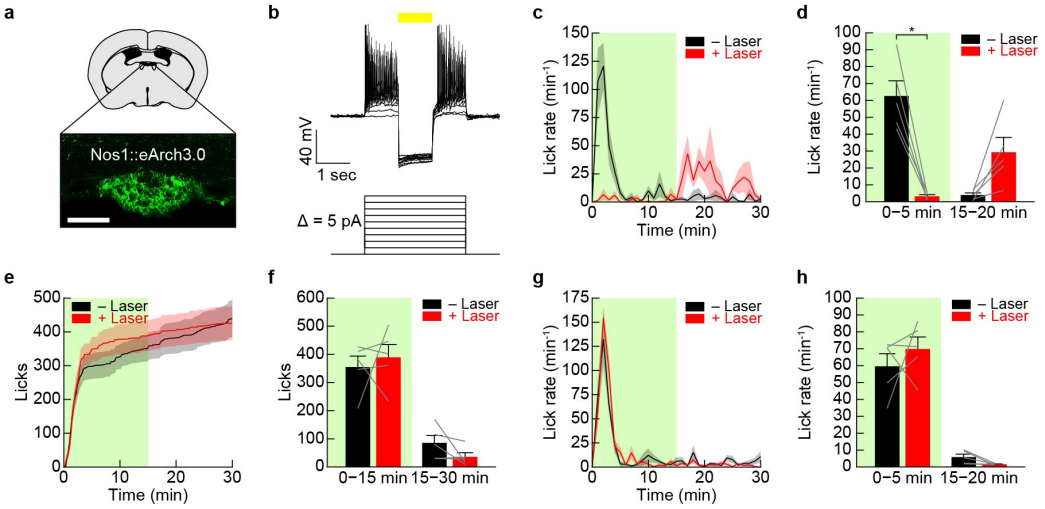


**Figure 2.9 | SFO$^{Nos1}$ neurons are necessary for drinking.**
**a**, Expression of yellow fluorescent protein (YFP) in SFO$^{Nos1}$ neurons from AAV5-EF1α-DIO-eArch3.0-YFP. Scale bar, 100 μm. **b**, Representative recording showing firing of SFO$^{Nos1}$ neurons is blocked in response to photosilencing in acute slice (1 out of 3 cells; yellow line, laser). **c**, Averaged traces showing lick rate for experiment in Figure 2.2j ($n$ = 5 mice; green box, laser on). **d**, Quantification (*$P$ < 0.05, two-way repeated- measures ANOVA, $n$ = 5 mice). **e**, Averaged traces showing cumulative licks after water restriction for SFO$^{Nos1}$::mCherry control mice ($n$ = 5 mice; green box, laser on). **f**, Quantification (n.s., two-way repeated-measures ANOVA, $n$ = 5 mice). **g**, Averaged traces showing lick rate after water restriction for SFO$^{Nos1}$::mCherry control mice ($n$ = 5 mice; green box, laser on). **h**, Quantification (n.s., two-way repeated-measures ANOVA, $n$ = 5 mice). Values are mean ± s.e.m. (error bars or shaded area).

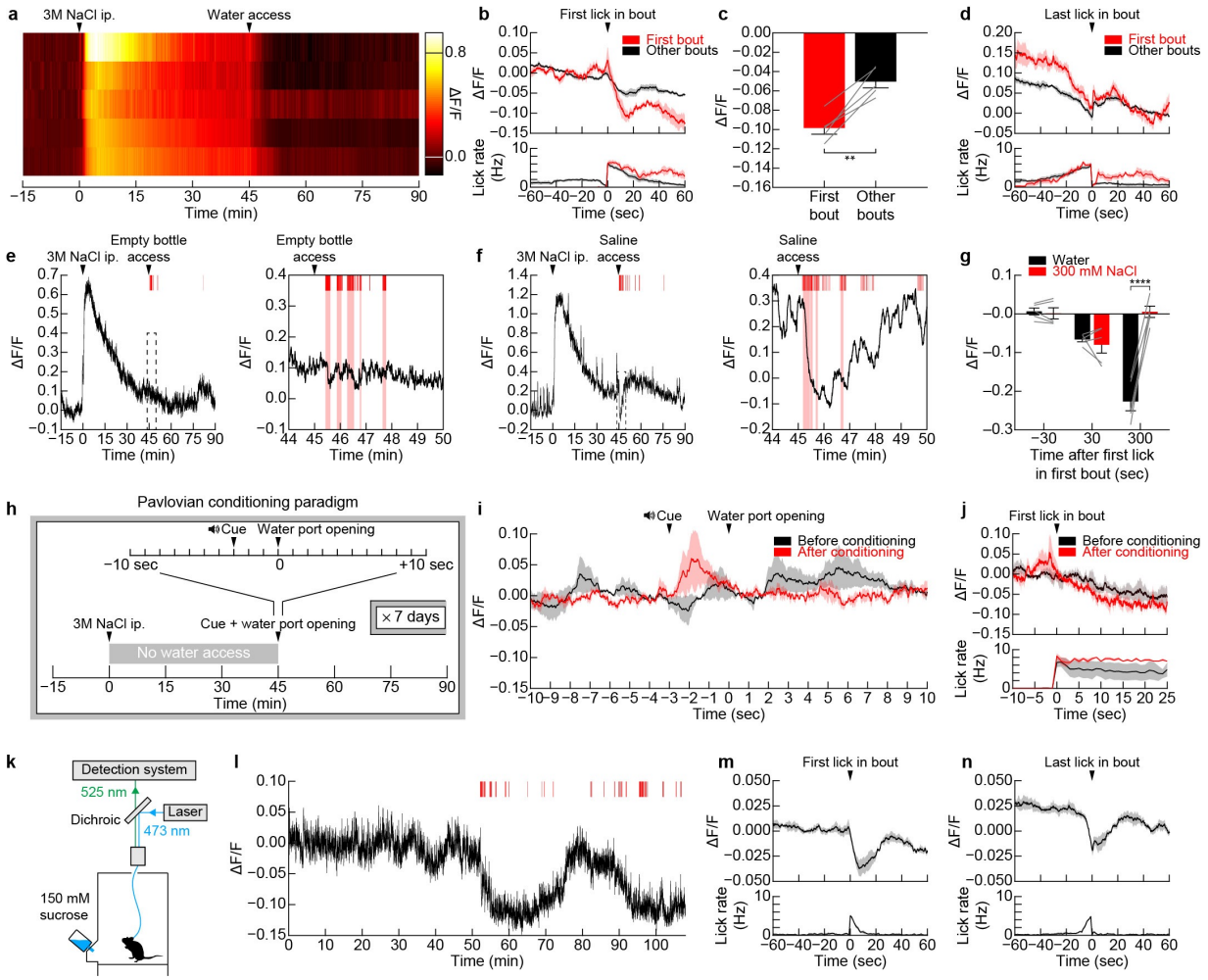


**Figure 2.10 | Regulation of SFO$^{Nos1}$ neurons by anticipatory signals.**
**a**, Representative recordings for five mice showing activation of SFO$^{Nos1}$ neurons during salt challenge and rapid inhibition of SFO$^{Nos1}$ neurons during drinking. **b**, PSTH of SFO$^{Nos1}$ neuron activity and lick rate around the first lick in either the first drinking bout or all other drinking bouts following salt challenge ($n$ = 5 mice). **c**, The decrease in SFO$^{Nos1}$ neuron activity was greatest during the first drinking bout ($\Delta F/F$ at 20 s after first lick; $^{**}P < 0.01$, two-tailed Student's $t$-test, $n$ = 5 mice). **d**, PSTH of SFO$^{Nos1}$ neuron activity and lick rate around the last lick in either the first drinking bout or all other drinking bouts following salt challenge ($n$ = 5 mice). **e**, Representative recording showing no inhibition of SFO$^{Nos1}$ neurons during licking an empty bottle following salt challenge (1 out of 5 mice; red lines, licks; red boxes, drinking bouts). **f**, Representative recording showing rapid inhibition followed by 're-setting' of SFO$^{Nos1}$ neurons during drinking 300 mM NaCl following salt challenge (1 out of 5 mice; red lines, licks; red boxes, drinking bouts). **g**, SFO$^{Nos1}$ neurons receive a post-ingestive error signal that reports the osmolarity of ingested fluids (averaged traces in Figure 2.3j; $^{****}P < 0.0001$, two-way repeated- measures ANOVA, $n$ = 5 mice). Panels **h–j** show that SFO$^{Nos1}$ neurons do not transmit a teaching signal in a Pavlovian conditioning model. **h**, Schematic of Pavlovian conditioning model. **i**, SFO$^{Nos1}$ neurons were not inhibited by cue presentation after 1 week of Pavlovian conditioning ($n$ = 3 mice). **j**, PSTH of SFO$^{Nos1}$ neuron activity and lick rate around the first lick in the first drinking bout either before or after Pavlovian conditioning ($n$ = 3 mice). Panels **k–n** demonstrate that SFO$^{Nos1}$ neurons are

modulated by rapid anticipatory signals during drinking in the absence of homeostatic need. **k**, The activity of $SFO^{Nos1}$ neurons was recorded while fully hydrated mice were given ad libitum access to sucrose. **l**, Representative recording showing modulation of $SFO^{Nos1}$ neurons during sucrose drinking (1 out of 4 mice; red lines, licks). **m**, PSTH of $SFO^{Nos1}$ neuron activity and lick rate around the first lick in all sucrose drinking bouts ($n$ = 4 mice). **n**, PSTH of $SFO^{Nos1}$ neuron activity and lick rate around the last lick in all sucrose drinking bouts ($n$ = 4 mice). Values are mean ± s.e.m. (error bars or shaded area).

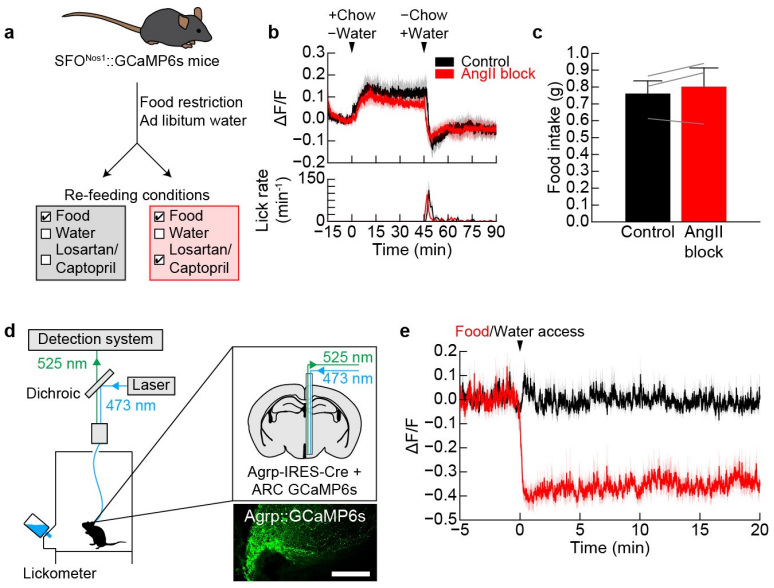


**Figure 2.11 | Activation of SFO$^{Nos1}$ neurons during eating does not require angiotensin signalling.**

**a**, Experimental design to test whether angiotensin signalling is necessary for prandial thirst. **b**, Angiotensin blockers (INH) did not inhibit eating-induced activation of SFO$^{Nos1}$ neurons or prandial drinking ($n$ = 3 mice). **c**, Angiotensin blockers did not affect food consumption (n.s., two-tailed Student's $t$-test, $n$ = 3 mice). **d**, **e**, ARC$^{AgRP}$ neurons that control hunger are not reciprocally modulated by eating and drinking. **d**, Schematic of fibre photometry set up for recording the activity of ARC$^{AgRP}$ neurons. Scale bar, 100 µm. **e**, ARC$^{AgRP}$ neurons were rapidly inhibited when fasted mice were presented with chow, as previously reported[27], but were unaffected when dehydrated mice were presented with water ($n$ = 5 mice). Values are mean ± s.e.m. (error bars or shaded area).

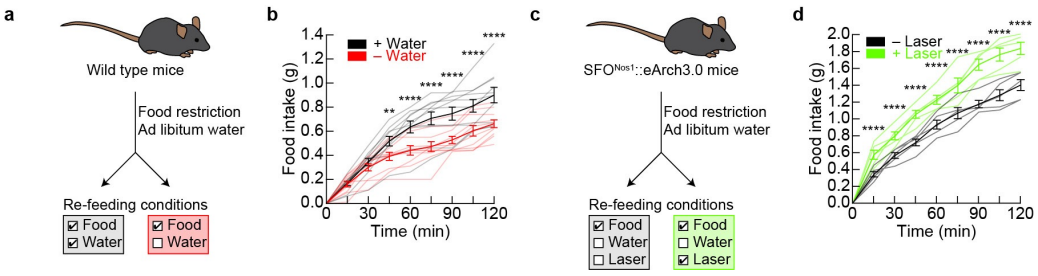


**Figure 2.12 | Silencing of SFO$^{Nos1}$ neurons disinhibits feeding.**
**a**, Experimental design to test whether prandial thirst inhibits food intake. **b**, Mice provided simultaneous access to water consumed more food after overnight fasting than mice without simultaneous access to water (**$P < 0.01$, ****$P < 0.0001$, two-way ANOVA, $n = 10$ mice per group), consistent with previous reports that thirst can inhibit hunger in rats[33]. **c**, Experimental design to test whether SFO$^{Nos1}$ neurons mediate inhibition of food intake by prandial thirst. **d**, Silencing of SFO$^{Nos1}$ neurons increased food intake when mice were provided with access to chow without simultaneous access to water after overnight fasting (****$P < 0.0001$, two-way repeated-measures ANOVA, $n = 5$ mice). Values are mean ± s.e.m. (error bars or shaded area).

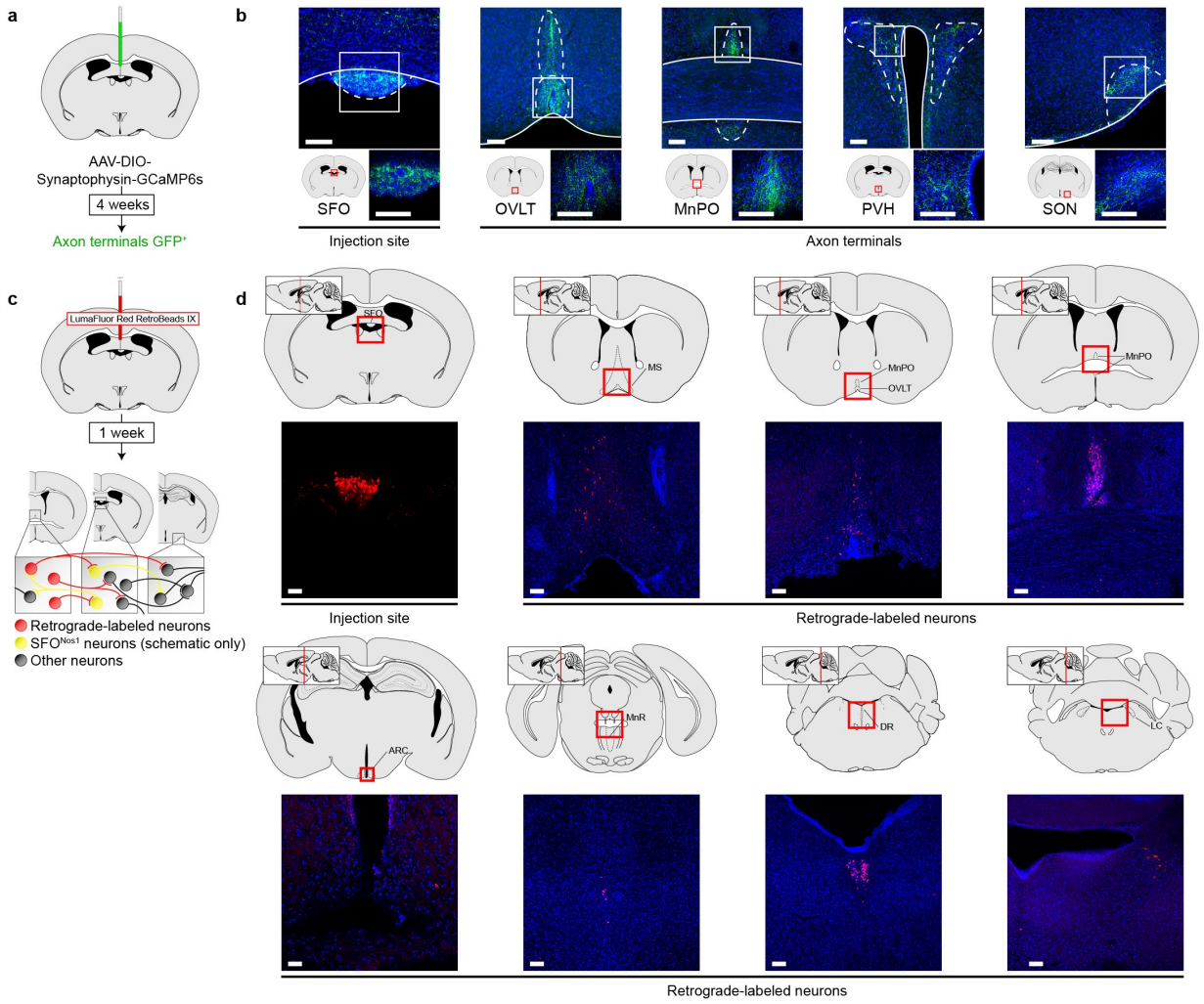


**Figure 2.13 | Projection mapping and retrograde tracing from SFO neurons.**
**a**, Schematic of viral strategy for identifying projections from SFO$^{Nos1}$ neurons using a fluorescent synaptophysin fusion protein. **b**, Representative images showing SFO$^{Nos1}$ neuron somas in the SFO and axon terminals in the OVLT, MnPO, PVH and supraoptic nucleus (SON) (1 out of 1 mice; green, GFP; blue, DAPI). Scale bars, 100 μm. **c**, Schematic of strategy for retrograde tracing from SFO neurons using retrobeads. **d**, Representative images showing retrobeads injection site in the SFO and retrograde-labelled neurons in the medial septum (MS), OVLT, MnPO, ARC, MnR, dorsal raphe (DR), and locus coeruleus (LC) (1 out of 2 mice; red, rhodamine; blue, DAPI). Scale bars, 100 μm.

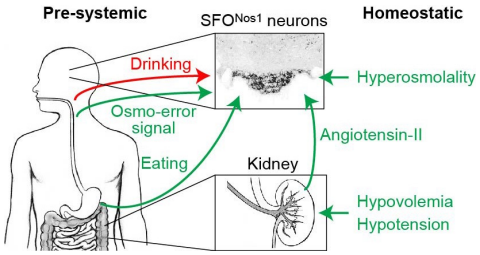


**Figure 2.14 | Schematic for convergence of anticipatory and homeostatic signals at SFO$^{Nos1}$ thirst neurons.**

SFO$^{Nos1}$ neurons monitor the composition of the blood by sensing plasma osmolarity and, via angiotensin, plasma volume and pressure. SFO$^{Nos1}$ neurons predict the future state of the blood by integrating temperature-dependent inputs from the mouth and osmolarity-dependent inputs from the gut during drinking, and angiotensin- and osmolarity-independent inputs from the mouth/gut during eating. Illustration from National Institute of Diabetes and Digestive and Kidney Diseases, US National Institutes of Health.

## METHODS

Experimental protocols were approved by the University of California, San Francisco IACUC following the NIH Guide for the Care and Use of Laboratory Animals.

### Reagents

Nos1-IRES-Cre mice (*Nos1*$^{tm1(cre)Mgmj}$, strain 017526), Agrp-IRES-Cre mice (*Agrp*$^{tm1(cre)LowJ}$, strain 012899), and wild-type mice (C57BL/6J, strain 000664) were obtained from the Jackson Laboratory. Agtr1$\alpha$-GFP mice (*Tg*(*Agtr1a-EGFP*)*NZ44Gsat*, strain 033059) were obtained from MMRRC. Adult mice (>4 weeks old) of both genders were used for experiments.

Recombinant AAVs expressing ChETA$_{TC}$ (AAV5-EF1$\alpha$-DIO-hChR2(E123T/T159C)-P2A-mCherry; AAV5-CaMK2$\alpha$-hChR2(E123T/T159C)-P2A-mCherry), ChR2/H134R (AAV5-CaMK2$\alpha$-hChR2(H134R)-YFP), eArch3.0 (AAV5-EF1$\alpha$-DIO-eArch3.0-YFP), mCherry (AAV5-EF1$\alpha$-DIO-mCherry), and GFP (AAV5-CaMK2$\alpha$-GFP) were obtained from the UNC Vector Core. Recombinant AAVs expressing GCaMP6s (AAV1-hSyn-FLEX-GCaMP6s; AAV5-hSyn-FLEX-GCaMP6s) and eArch3.0 (AAV5-CBA-FLEX-eArch3.0-GFP) were obtained from the Penn Vector Core. Recombinant EnvA-pseudotyped G-deficient Rabies virus expressing GFP (RV-EnvA-$\Delta$G-GFP) was obtained from the Salk Institute.

Plasmids encoding synaptophysin-GCaMP6s and GFP-RPL10a fusion proteins were generated in-house. Recombinant AAVs containing these plasmids (AAV5-EF1$\alpha$-DIO-synaptophysin-GCaMP6s; AAV2-EF1$\alpha$-FLEX-GFP-RPL10a) were commercially produced by the UNC Vector Core. Rabies helper viruses (AAV1-CAG-DIO-TVA-mCherry; AAV1-CAG-DIO-G) were obtained from the laboratory of N. Shah.

**Stereotaxic surgery**

For SFO injections, 100–300 nl of virus was injected at one site (–0.50 mm antero-posterior (AP); 0 mm medio-lateral (ML); –2.75 mm dorso-ventral (DV) relative to bregma). For ARC injections, 1 μl of virus total was injected at two sites (–1.85 mm AP; –0.3 mm ML; –5.7 and –5.8 mm DV). Mice were allowed 2–4 weeks for viral expression and recovery from surgery before behavioural testing.

For soma photostimulation experiments, recombinant AAVs expressing $ChETA_{TC}$, mCherry, or GFP were stereotaxically injected into the SFO of Nos1-IRES-Cre mice and wild-type mice. In the same surgery, a fibreoptic cannula was implanted unilaterally above the SFO (–2.25 mm DV).

For terminal photostimulation experiments, recombinant AAVs expressing hChR2/H134R or GFP were injected into the SFO of wild-type mice. In the same surgery, a fibreoptic cannula was implanted unilaterally above the MnPO (+0.45 mm AP; +0 mm ML; –3.7 mm DV) or PVH (–0.75 mm AP; +0.2 mm ML; –3.9 mm DV).

For photoinhibition experiments, recombinant AAVs expressing eArch3.0 or mCherry were injected into the SFO of Nos1-IRES-Cre mice. In the same surgery, a fibreoptic cannula was implanted unilaterally above the SFO (–2.35 mm DV).

For photometry experiments, recombinant AAVs expressing GCaMP6s or GFP were injected into the SFO of Nos1-IRES-Cre mice and into the ARC of Agrp-IRES-Cre. In the same surgery, a fibreoptic cannula was implanted unilaterally above the SFO (–2.95 mm DV) or ARC (–5.7 mm DV).

For projection-mapping experiments, recombinant AAVs expressing synaptophysin-GCaMP6s were injected into the SFO of Nos1-IRES-Cre mice. After four weeks, mice were euthanized and processed for histology.

For rabies tracing experiments, recombinant AAVs expressing TVA and G were injected into the SFO of Nos1-IRES-Cre mice. After two weeks, recombinant EnvA-pseudotyped G-deficient rabies virus expressing GFP was injected into the SFO. After one additional week, mice were euthanized and processed for histology.

For retrobeads tracing experiments, red RetroBeads IX (LumaFluor) were injected into the SFO of wild-type mice. After one week, mice were euthanized and processed for histology.

**Slice electrophysiology and calcium imaging**

Acute forebrain slices were prepared from 8–15-week-old Nos1-IRES-Cre mice expressing $ChETA_{TC}$, eArch3.0, or GCaMP6s for 2–4 weeks. Fluorescent cells in the SFO were identified for whole-cell patch clamp recordings. Slices were sectioned in ice-cold oxygenated (95% $O_2$/ 5% $CO_2$) cutting saline containing (in mM) 26 $NaHCO_3$, 1.25 $NaH_2PO_4$, 3 KCl, 10 glucose, 210 sucrose, 2 $CaCl_2$, 2 $MgCl_2$. Slices were then transferred to oxygenated artificial cerebrospinal fluid (ACSF) containing (in mM) 125 NaCl, 25 $NaHCO_3$, 1.25 $NaH_2PO_4$, 2.5 KCl, 15 glucose, 2 $CaCl_2$, 1 $MgCl_2$ and incubated at 34 °C for 30 min. Slices were then stored at room temperature until used. During experiments, slices were placed in a recording chamber and superfused with oxygenated ACSF. Glass pipettes for recording (3–8 MΩ) were pulled from borosilicate glass capillary (O.D. 1.5 mm, I.D. 0.86 mm, Sutter Instrument) and filled with internal solution containing (in mM) 125 K gluconate, 10 KCl, 4 NaCl, 4 $Mg_3ATP_2$, 0.3 $Na_3ATP$, 5 $Na_2$-phosphocreatine, 10 HEPES. Whole-cell recordings were made at 28 °C using an Axopatch 700B amplifier (Molecular Devices). Data acquisition (filtered at 5 kHz and digitized at 10 kHz) and pulse generation were performed using a Digidata 1550 (Molecular Devices) and pClamp software (version 10.5, http://www.moleculardevices.com).

For channelrhodopsin validation, cells were photostimulated under current clamp mode using an LED light source (Lambda HPX, Sutter Instruments) pulsing light at 5–40 Hz through a 470 nm excitation filter set (U-N41 017, E.X. 470 nm, B.S. 495 nm, E.M. 5, Olympus).

For archaerhodopsin validation, cells were activated using currents ranging from 0 pA to 45 pA ($\Delta I$ = 5 pA) for 3 s in duration injected under current clamp mode. During current injection, cells were photosilenced using an LED light source (Lambda HPX, Sutter Instruments) sending constant light through a 500 nm excitation filter set (49003, E.X. 500 nm, B.S. 515 nm, E.M. 5, Chroma Technology).

For calcium imaging validation, cells were activated using currents (30 pA) ranging from 100 ms to 1 s ($\Delta t$ = 100 ms) in duration injected under current clamp mode. Calcium imaging was performed simultaneously using a digital CCD camera (Hamamatsu, ORCA-ER) mounted on an upright microscope (Olympus, BX51). Micro-manager software (version 1.4, http://www.micro-manager.org) was used as microscope control interface. After loading, cells were imaged (10 ms exposure time; 10 Hz) using an LED light source (Lambda HPX, Sutter Instruments) sending constant light through a 470 nm excitation filter set (U-N41 017, E.X. 470 nm, B.S. 495 nm, E.M. 5, Olympus). We have previously validated the use of GCaMP6s to image calcium signals in $ARC^{AgRP}$ neurons[27].

To visualize the responsiveness of $SFO^{Nos1}$ neurons to angiotensin II (AngII), 1 μM AngII was bath-applied using a slow perfusion system (2 ml $min^{-1}$) during imaging. Data analysis followed the basic logic described previously[27]. Regions of interest (ROIs) were selected using the polygon selection tool in ImageJ with cell nucleus included. The plot *z*-axis profile function in ImageJ was then used to measure the mean value of each ROI versus frame number. Neuropil fluorescence was selected and estimated using the same protocol. Only regions located near the cell with no detectable fluorescent neural processes were used. The true fluorescence signal of each cell was estimated with function: $F_{cell\_true}(t) = F_{cell\_measured}(t) - r \times F_{neuropil}(t)$, where $r$ = 0.7.

**Photostimulation *in vivo***

All experiments were performed in behavioural chambers (Coulbourn Instruments, Habitest Modular System). Experiments were performed during the light cycle to control for circadian factors and performed in a well-lit environment illuminated with white light. Water consumption was monitored with an optical lickometer (Colbourn Instruments). Mice were acclimated to the behavioural chamber for at least 15 min before the beginning of each testing session. For some experiments, video was recorded using cameras installed above each cage.

To test whether acute photostimulation could induce drinking, mice were provided with constant access to water and monitored for 30 min (pre-stim), then photostimulated for 30 min (stim, 10 ms pulses at 20 Hz for 1 s every 4 s, 20–25 mW) using a DPSS 473 nm laser (Shanghai Laser and Optics Century), and then monitored for another 30 min (post-stim).

For saline drinking experiments, the same model was used except that mice were provided with access to 150 mM NaCl in water.

For delayed-access experiments, the same model was used except that stimulation lasted 60 min instead of 30 min. Water access was removed after 30 min pre-stimulation period and water re-access was provided 30 min later.

For water restriction experiments, mice were water-restricted for 24 h in their home cages, acclimated to the behavioural chamber for 15 min, and then provided with access to water for 30 min. To compare photostimulation to water restriction, all sessions were aligned to the first lick in the stimulation or water-access period.

For food consumption experiments, mice were fed ad libitum in their home cages, acclimated to the behavioural chamber for 15 min, and then provided with a single pellet of chow without simultaneous access to water for 30 min. After 30 min, chow was removed and the amount consumed measured.

**Photoinhibition *in vivo***

All experiments were performed in behavioural chambers (Coulbourn Instruments, Habitest Modular System). Experiments were performed during the light cycle to control for circadian factors and performed in a well-lit environment illuminated with white light. Water consumption was monitored with an optical lickometer (Colbourn Instruments). Mice were acclimated to the behavioural chamber for at least 15 min before the beginning of each testing session.

To test whether acute silencing could inhibit drinking, mice were water-restricted for 24 h in their home cages, acclimated to the behavioural chamber for 15 min, and then provided with access to water for 15 min with or without optical silencing (10–15 mW) using a DPSS 532 nm laser (Shanghai Laser and Optics Century), then monitored for another 15 min without optical silencing. Trials with and without photoinhibition ('–laser' and '+laser') were interleaved.

To test whether acute optical silencing could inhibit prandial drinking in fasted mice, mice were fasted for 24 h in their home cages, acclimated to the behavioural chamber for 15 min, then provided with a single pellet of chow under one of two experimental conditions: (1) no water access and no laser for 45 min, chow removal, then water access ± laser for 30 min, (2) no water access ± laser for 2 h. In experimental condition 2, chow was removed and the amount consumed measured every 15 min.

**Fibre photometry**

Construction of the rig for performing fibre photometry has been previously described[27]. The signal was output to a lock-in amplifier (Stanford Research System, SR810) with time constant 30 ms to allow filtering of noise at higher frequency. Signal was then digitized with LabJack U6-Pro and recorded using software provided by LabJack (http://labjack.com/support/software) with 250 Hz sampling rate.

All experiments were performed in behavioural chambers (Coulbourn Instruments, Habitest Modular System). Experiments were performed during the light cycle to control for circadian factors and performed in a well-lit environment illuminated with white light. Mice were acclimated to the behavioural chamber for at least 15 min with access to 24 °C water before the beginning of each testing session. Photometry data were subjected to minimal processing consisting of only within-trial fluorescence normalization. For some experiments, video was recorded using cameras installed above each cage.

For pharmacological experiments, mice were acclimated to the behavioural chamber for 15 min, then given an injection and monitored for 45 min. AngII (20 μg per mouse, 200 μg per mouse), losartan (100 mg $kg^{-1}$), captopril (50 mg $kg^{-1}$), and PEG (40%) were administered subcutaneously, and NaCl (1 M, 2 M, 3 M), mannitol (2 M), and isoproterenol (100 mg $kg^{-1}$) were administered intraperitoneally. All subcutaneous injections were given in a total volume of 400 μl with PBS as vehicle, and all intraperitoneal injections were given in a total volume of 150 μl with PBS as vehicle. To block angiotensin signalling, losartan was administered 30 min before AngII injection, and losartan plus captopril (described as 'angiotensin blockers' and 'INH') were administered simultaneously to PEG/NaCl/isoproterenol injection or chow access. Losartan is a selective AngII type 1 receptor ($AT_1R$) antagonist[31], and captopril is an angiotensin converting enzyme (ACE) inhibitor[32]. Mice were not provided with access to water unless otherwise noted.

For water restriction experiment in Figure 2.2a, mice were placed in the behavioural chamber and calcium signals recorded for 10 min on day one ('BA'). Mice were then returned to their home cages and water-restricted for 24 h. After 24 h of water restriction, mice were placed in the behavioural chamber and calcium signals again recorded for 10 min on day two ('WR'). Mice were then returned to their home cages and immediately provided with access to water. After 1 h of water re-access, mice were placed in the behavioural chamber and calcium signals again recorded for 10 min ('WA'). Photometry settings, including laser power and time constant,

were the same for every mouse and every recording session. The reported fluorescence was calculated as the median fluorescence of minutes 5–10 of each recording.

For other water restriction experiments, mice were water-restricted for 48 h in their home cages, acclimated to the behavioural chamber for 15 min, and then provided with access to water for 45 min. For all experiments, the opening of a guillotine port cued water access.

For salt-loading experiments, mice were acclimated to the behavioural chamber for 15 min, and then given an intraperitoneal injection of 150 μl 3 M NaCl. After 45 min, mice were provided with access for 45 min to a bottle that was empty, contained 12 °C, 24 °C or 36 °C water, or contained 24 °C 300 mM NaCl in water. Quantification of PSTHs in Figure 2.3f, h refers to $\Delta F/F$ at 15 s. The PSTHs in Figure 2.3g represent the first bout from 24 °C water bottle and all bouts from empty bottle.

For oral cooling experiments, mice were given an intraperitoneal injection of 150 μl 3 M NaCl. After 10–15 min, a piece of dry metal (ice-cold, 'oral cooling'; room temperature, 'sham') was placed in the oral cavity, held for 30 s, and then removed. This process was repeated after >60 s wait with metal of the other temperature. The temperature order was counter-balanced across trials.

For sucrose drinking experiments, mice were provided with access to food and water ad libitum before testing. Mice were acclimated to the behavioural chamber for 15 min, then provided with ad libitum access to 150 mM sucrose for >2 h.

For fasting-refeeding experiments, mice were fasted for 24 h in their home cages, acclimated to the behavioural chamber for 15 min, and then provided with a single pellet of chow either with or without simultaneous access to water for 45 min. After 45 min, chow was removed and the amount consumed measured, and mice were immediately provided with access to water for 45 min.

For Pavlovian conditioning experiments, mice were acclimated to the behavioural chamber for 15 min, and then given an intraperitoneal injection of 150 μl 3 M NaCl. After 45 min, an auditory cue was played (2.9 kHz, 300 ms; Colbourn Instruments), and 3 s later the water port was opened and mice were provided with access to water for 45 min. There were seven training trials and a final probe trial (both training and probe trials included auditory cue).

**Data analysis**

All data were analysed with custom MATLAB code. Throughout the paper, a drinking bout is defined as any set of ten or more licks in which no inter-lick interval is greater than one second.

For photometry data, all responses were normalized to baseline using the function: $\Delta F/F = (F - F_0)/F_0$, in which $F_0$ is the median fluorescence of the baseline period. The baseline period for full experiments was 15 min before time zero, and the baseline period for PSTHs around drinking bouts was 60 s before the first lick or 60 s after the last lick in a bout (15 s for cue and empty bottle plots). Time zero was defined as the moment the mouse was returned to the behavioural chamber following injection, the moment of water access, or the moment of chow access. The time constant, $\tau$, was estimated as described previously[27]. In bar graphs quantifying $\Delta F/F$, the median fluorescence of a 1-s window around the indicated time is reported, and 1 min before time zero is reported as baseline.

**Plasma osmolality**

For water restriction experiments, wild-type mice were water-restricted for 24 h, then provided with access to water at $t = 0$. For salt-loading experiments, wild-type mice were given an intraperitoneal injection of 150 μl 3 M NaCl at $t = 0$, and then provided with access to water at $t = 45$ min. For fasting-refeeding experiments, wild-type mice were fasted for 24 h, then provided

with a single pellet of chow without simultaneous access to water at $t$ = 0. At $t$ = 45 min, chow was removed, and mice were immediately provided with access to water. At a single time point per session (hydrated, 0 min, 5 min, 45 min for water restriction experiments; 0 min, 5 min, 45 min, 50 min, 90 min for salt-loading experiments; fed, 0 min, 15 min, 45 min, 50 min for fasting-refeeding experiments), 125 μl of blood was collected from the tail vein using EDTA-coated capillary tubes (RAM Scientific). Plasma was isolated by centrifugation, and osmolality was measured using a freezing point osmometer (Fiske Associates). Mice were allowed 1 week for recovery between sessions.

**Plasma protein**

Wild-type mice were water-restricted for 24 h, and then provided with access to water at $t$ = 0. At a single time point per session (hydrated, 0 min, 5 min, 45 min), 125 μl of blood was collected from the tail vein using EDTA-coated capillary tubes (RAM Scientific). Plasma was isolated by centrifugation, and plasma protein concentration was measured using a BCA protein assay kit (Thermo Fisher Scientific). Mice were allowed 1 week for recovery between sessions. Plasma protein concentration is inversely proportional to plasma volume.

**Immunohistochemistry**

Mice were transcardially perfused with PBS followed by formalin. Brains were post-fixed overnight in formalin and placed in 20% sucrose for 24 h. Free-floating sections (40 μm) were prepared with a cryostat, blocked (3% BSA, 2% NGS, and 0.1% Triton-X in PBS for 2 h), and then incubated with primary antibody (chicken anti-GFP, Abcam, ab13970, 1:1,000; rat anti-RFP, ChromoTek, 5f8, 1:2,000; rabbit anti-cFos, Santa Cruz Biotech, sc52, 1:1,000) overnight at 4 °C (two nights for cFos staining). Sections were then washed, incubated with secondary antibody (Alexa Fluor 488 goat anti-chicken, Life Technologies, a11039, 1:1,000; Alexa Fluor 568 goat

anti-rat, Life Technologies, a11077, 1:1,000; Alexa Fluor 568 goat anti-rabbit, Life Technologies, a11011, 1:1,000) for 2 h at room temperature, mounted, and imaged with a Zeiss LSM 700 confocal microscope. Sections stained for cFos underwent unmasking before blocking (1% $H_2O_2$ and 1% NaOH in PBS for 10 min; 0.3% glycine in PBS for 10 min; 0.03% SDS in PBS for 10 min).

For rabies tracing experiments, mice were transcardially perfused with PBS followed by formalin. Brains were post-fixed overnight in formalin and placed in 20% sucrose for 24 h. Free-floating sections (40 μm) were prepared with a cryostat and half of sections were immediately mounted and imaged by direct fluorescence with a Zeiss LSM 700 confocal microscope. Quantification was performed using the cell counter tool in ImageJ.

**Statistics**

Values are reported as mean ± s.e.m. (error bars or shaded area). The shaded area in Figure 2.7d represents the 95% confidence interval for the line-of-best-fit. Statistical analyses and linear regressions were performed using MATLAB or Prism. *P* values for pair-wise comparisons were performed using a two-tailed Student's *t*-test. *P* values for comparisons across multiple groups were performed using analysis of variance (ANOVA) and corrected for multiple comparisons using the Holm–Šídák method. $^{*}P < 0.05$, $^{**}P < 0.01$, $^{***}P < 0.001$, $^{****}P < 0.0001$. Result sheets of statistical tests from Prism detailing (wherever applicable) estimates of variance within each group, comparison of variances across groups and so on are available on request. Animals for fibre photometry experiments were excluded if there was no response (<10%) to 3 M NaCl injection i.p. ($SFO^{Nos1}$ neurons) or to 60 μg ghrelin injection i.p. ($ARC^{AgRP}$ neurons). Animals for optogenetics experiments were excluded based on histology (expression of $ChETA_{TC}$/ hChR2(H134R)/eArch3.0 in SFO) and fibreoptic placement. We observed few and sparse virally infected cells outside the SFO. These criteria were pre-established. No statistical method was used to predetermine sample size. Randomization and blinding were not used.

## REFERENCES


1 Lind, R. W., Thunhorst, R. L. & Johnson, A. K. The subfornical organ and the integration of multiple factors in thirst. *Physiol. Behav.* **32**, 69–74 (1984).

2 McKinley, M. J. & Johnson, A. K. The physiological regulation of thirst and fluid intake. *News Physiol. Sci.* **19**, 1–6 (2004).

3 Bourque, C. W. Central mechanisms of osmosensation and systemic osmoregulation. *Nat. Rev. Neurosci.* **9**, 519–531 (2008).

4 Berridge, K. C. Motivation concepts in behavioral neuroscience. *Physiol. Behav.* **81**, 179–209 (2004).

5 Woods, S. C. & Ramsay, D. S. Homeostasis: beyond Curt Richter. *Appetite* **49**, 388–398 (2007).

6 Stricker, E. M. & Hoffmann, M. L. Presystemic signals in the control of thirst, salt appetite, and vasopressin secretion. *Physiol. Behav.* **91**, 404–412 (2007).

7 Thrasher, T. N., Nistal-Herrera, J. F., Keil, L. C. & Ramsay, D. J. Satiety and inhibition of vasopressin secretion after drinking in dehydrated dogs. *Am. J. Physiol. Endocrinol. Metabol.* **240**, E394–E401 (1981).

8 Bellows, R. T. Time factors in water drinking in dogs. *Am. J. Physiol.* **125**, 87–97 (1938).

9 Adolph, E. F., Barker, J. P. & Hoy, P. A. Multiple factors in thirst. *Am. J. Physiol.* **178**, 538–562 (1954).

10 Oatley, K. & Toates, F. M. The passage of food through the gut of rats and its uptake of fluid. *Psychon. Sci.* **16**, 225–226 (1969).

11 Fitzsimons, J. T. & Le Magnen, J. Eating as a regulatory control of drinking in the rat. *J. Comp. Physiol. Psychol.* **67**, 273–283 (1969).

12 Deaux, E. Thirst satiation and the temperature of ingested water. *Science* **181**, 1166–1167 (1973).

13 Kapatos, G. & Gold, R. M. Tongue cooling during drinking: a regulator of water intake in rats. *Science* **176**, 685–686 (1972).

14 Eccles, R., Du-Plessis, L., Dommels, Y. & Wilkinson, J. E. Cold pleasure. Why we like ice drinks, ice-lollies and ice cream. *Appetite* **71**, 357–360 (2013).

15 Shizgal, P. B. & Hyman, S. E. in *Principles of Neural Science* (eds Kandel, E. R. *et al.*), 5 edn, 1095–1115 (McGraw-Hill, 2013).

16 Egan, G. *et al.* Neural correlates of the emergence of consciousness of thirst. *Proc. Natl. Acad. Sci. USA* **100**, 15241–15246 (2003).

17 Farrell, M. J. *et al.* Cortical activation and lamina terminalis functional connectivity during thirst and drinking in humans. *Am. J. Physiol. Regul. Integr. Comp. Physiol.* **301**, R623–R631 (2011).

18 McKinley, M. J., Denton, D. A., Oldfield, B. J., De Oliveira, L. B. & Mathai, M. L. Water intake and the neural correlates of the consciousness of thirst. *Semin. Nephrol.* **26**, 249–257 (2006).

19 Oka, Y., Ye, M. & Zuker, C. S. Thirst driving and suppressing signals encoded by distinct neural populations in the brain. *Nature* **520**, 349–352 (2015).

20 Grob, M., Trottier, J. F., Drolet, G. & Mouginot, D. Characterization of the neurochemical content of neuronal populations of the lamina terminalis activated by acute hydromineral challenge. *Neuroscience* **122**, 247–257 (2003).

21 Simpson, J. B. & Routtenberg, A. Subfornical organ: site of drinking elicitation by angiotensin II. *Science* **181**, 1172–1175 (1973).

22 Betley, J. N. *et al.* Neurons for hunger and thirst transmit a negative-valence teaching signal. *Nature* **521**, 180–185 (2015).

23 Gunaydin, L. A. *et al.* Natural neural projection dynamics underlying social behavior. *Cell* **157**, 1535–1551 (2014).

24 Rowland, N. E. Brain mechanisms of mammalian fluid homeostasis: insights from use of immediate early gene mapping. *Neurosci. Biobehav. Rev.* **23**, 49–63 (1998).

25 Szczepańska-Sadowska, E., Kozłowski, S. & Obidzińska, K. Equipotency of hypertonic solutions of mannitol and sodium chloride in eliciting thirst in the dog. *Pflügers Arch.* **358**, 259–264 (1975).

26 Fitzsimons, J. T. Drinking by rats depleted of body fluid without increase in osmotic pressure. *J. Physiol.* **159**, 297–309 (1961).

27 Chen, Y., Lin, Y. C., Kuo, T. W. & Knight, Z. A. Sensory detection of food rapidly modulates arcuate feeding circuits. *Cell* **160**, 829–841 (2015).

28 Mandelblat-Cerf, Y. *et al.* Arcuate hypothalamic AgRP and putative POMC neurons show opposite changes in spiking across multiple timescales. *eLife* **4**, e07122 (2015).

29 Mendelson, J. & Chillag, D. Tongue cooling: a new reward for thirsty rodents. *Science* **170**, 1418–1421 (1970).

30 Miselis, R. R., Shapiro, R. E. & Hand, P. J. Subfornical organ efferents to neural systems for control of body water. *Science* **205**, 1022–1025 (1979).

31 Smith, R. D., Chiu, A. T., Wong, P. C., Herblin, W. F. & Timmermans, P. B. M. W. M. Pharmacology of nonpeptide angiotensin II receptor antagonists. *Annu. Rev. Pharmacol. Toxicol.* **32**, 135–165 (1992).

32 Ondetti, M. A., Rubin, B. & Cushman, D. W. Design of specific inhibitors of angiotensin-converting enzyme: new class of orally active antihypertensive agents. *Science* **196**, 441–444 (1977).

33 Hsiao, S. & Trankina, F. Thirst-hunger interaction: I. Effects of body-fluid restoration on food and water intake in water-deprived rats. *J. Comp. Physiol. Psychol.* **69**, 448–453 (1969).

*III. The forebrain thirst circuit drives drinking through negative reinforcement*

---

The material in this chapter is reprinted from:

> David E. Leib*, Christopher A. Zimmerman*, Ailar Poormoghaddam, Erica L. Huey, Jamie S. Ahn, Yen-Chu Lin, Chan Lek Tan, Yiming Chen, Zachary A. Knight. The forebrain thirst circuit drives drinking through negative reinforcement. *Neuron* 96, 1272–1281, 2017. *These authors contributed equally

D.E.L., C.A.Z. and Z.A.K. conceived the project and designed the experiments. D.E.L. and C.A.Z. performed stereotaxic surgeries and conducted experiments related to the MnPO and SFO/OVLT, respectively. A.P. and E.L.H. also performed stereotaxic surgeries, and A.P. conducted some behavioral experiments. J.S.A. performed in situs, Y.-C.L. performed electrophysiology experiments and C.L.T. performed thermoregulation experiments. C.A.Z. generated the *Agtr1a-2a-Cre* mouse with initial help from Y.C. D.E.L., C.A.Z. and Z.A.K. analyzed the data and prepared the manuscript with input from all authors.

## ABSTRACT

The brain transforms the need for water into the desire to drink, but how this transformation is performed remains unknown. Here we describe the motivational mechanism by which the forebrain thirst circuit drives drinking. We show that thirst-promoting subfornical organ neurons are negatively reinforcing, and that this negative-valence signal is transmitted along projections to the organum vasculosum of the lamina terminalis (OVLT) and median preoptic nucleus (MnPO). We then identify molecularly-defined cell types within the OVLT and MnPO that are activated by fluid imbalance and show that stimulation of these neurons is sufficient to drive drinking, cardiovascular responses, and negative reinforcement. Finally, we demonstrate that the thirst signal exits these regions through at least three parallel pathways and show that these projections dissociate the cardiovascular and behavioral responses to fluid imbalance. These findings reveal a distributed thirst circuit that motivates drinking by the common mechanism of drive reduction.

## INTRODUCTION

Eating and drinking are fundamental motivated behaviors, but how the brain transforms the need for food or water into a specific motivational drive remains poorly understood. Traditionally, two broad classes of mechanisms have been proposed to motivate behavior[1]. The first involves the ability of food or water deprivation to magnify the rewarding properties of eating or drinking and thereby positively reinforce these behaviors. This is the mechanism that makes food taste more delicious when you are hungry, a phenomenon known as alliesthesia[2,3]. On the other hand, food and water deprivation are experienced as intrinsically unpleasant states, and therefore, animals will perform work simply to avoid these aversive conditions, a mechanism known as negative reinforcement or drive reduction[4,5]. Under normal conditions, these two processes are thought

to work together to motivate behavior, but it remains unknown how they are each instantiated in the brain at the level of specific neural circuits.

For the control of drinking behavior, the critical neurons that sense and respond to changes in internal state are located within three small, interconnected forebrain nuclei known collectively as the lamina terminalis (LT). These structures include the subfornical organ (SFO) and organum vasculosum of the lamina terminalis (OVLT), which are situated outside the blood-brain barrier and contain interoceptive neurons that monitor the blood directly[6], and the median preoptic nucleus (MnPO), which is thought to function as a downstream integratory site[7]. When the blood volume falls or osmolarity rises, neurons within these three nuclei become activated, thereby triggering thirst, salt appetite, and an array of autonomic and neuroendocrine outputs that function to restore fluid balance[8–11].

Given its preeminent role in the control of drinking behavior, the LT represents a logical starting point for investigation of the motivational processes underlying thirst. However, this investigation has been complicated by the fact that each structure within the LT is neurochemically heterogeneous, and the specific cell types that control drinking in the OVLT and MnPO have not been fully characterized[11,12]. In the SFO, a population of glutamatergic neurons defined by expression of the genes *Nos1*, *Etv1*, and *Camk2* ($SFO^{GLUT}$ neurons) are activated during thirst and are necessary and sufficient for drinking behavior[13–17]. Furthermore, stimulation of $SFO^{GLUT}$ neurons has negative valence[14]. However, it remains unclear whether this negative-valence signal is the mechanism by which $SFO^{GLUT}$ neurons motivate behavior, because it has not been demonstrated that animals will perform work to shut off this signal, which is the hallmark of negative-reinforcement learning[18].

To address these questions, we have systematically investigated the cells, pathways, and motivational mechanisms by which the forebrain thirst circuit generates drinking behavior.

## RESULTS

### $SFO^{GLUT}$ neurons coordinate the behavioral and autonomic responses to fluid imbalance

We first targeted channelrhodopsin-2 (ChR2) to $SFO^{GLUT}$ neurons and implanted an optical fiber above the SFO (Figure 3.1a). As previously reported, photostimulation of $SFO^{GLUT}$ neurons triggered voracious and specific water consumption (Figure 3.1b, c)[13,14,16]. Photostimulation of $SFO^{GLUT}$ neurons also triggered a rapid and reversible increase in blood pressure (Figure 3.1d, Figure 3.5), which likely functions to increase blood circulation in response to acute drops in blood volume[19]. These results indicate that glutamatergic neurons in the SFO coordinate both the behavioral and autonomic responses to fluid imbalance.

### Stimulation of $SFO^{GLUT}$ neurons and their projections is negatively reinforcing

We next trained mice with daily sessions in which they were exposed to tonic photostimulation while given access to two levers, one of which induced a pause in photostimulation and the other of which was inactive (Figure 3.1e). After training in this negative-reinforcement paradigm, mice expressing ChR2 in $SFO^{GLUT}$ neurons preferentially pressed the active lever to pause photostimulation (Figure 3.1e). In contrast, control mice expressing GFP in $SFO^{GLUT}$ neurons showed no response to photostimulation in any assay. These data demonstrate that mice will perform instrumental responses to reduce $SFO^{GLUT}$ neuron activity and therefore that the activity of these neurons is negatively reinforcing.

The SFO drives thirst via projections to two other LT structures, the OVLT and MnPO[16,17]. To test whether $SFO^{GLUT}$ neurons transmit a negative-reinforcement signal to these downstream sites, we targeted ChR2 to $SFO^{GLUT}$ neurons and implanted an optical fiber above the MnPO (Figure 3.1f). This fiber placement results in stimulation of axons innervating the MnPO as well as fibers of passage targeting the OVLT. We first confirmed that photostimulation of $SFO^{GLUT}\rightarrow$ MnPO/OVLT axons drives robust and specific water consumption (Figure 3.1g, h) and elevates

blood pressure (Figure 3.1i, Figure 3.5) to an extent comparable to stimulation of $SFO^{GLUT}$ neuron somas. We then trained these mice in the negative-reinforcement paradigm described above, which revealed that mice will robustly lever press to prevent photostimulation of $SFO^{GLUT}$→MnPO/OVLT projections (Figure 3.1j). Thus, projections from $SFO^{GLUT}$ neurons to the OVLT and/or MnPO relay a negative-reinforcement signal that corresponds with the ability of these projections to drive drinking.

**$OVLT^{Agtr1a}$ neurons are activated by hyperosmolarity, and their activation drives drinking and hypertension**

The OVLT and MnPO were first implicated in the control of drinking behavior decades ago[20], but the molecular identity of thirst-promoting neurons in these structures has remained unclear[11]. We first focused on the OVLT, which, like the SFO, lies outside the blood-brain barrier and therefore has unfettered access to circulating signals that stimulate thirst. The angiotensin 1A receptor (encoded by the *Agtr1a* gene) is expressed in the OVLT[21,22] and is involved in the control of drinking behavior[23]. We used an Agtr1a-GFP reporter line[22] to examine whether $OVLT^{Agtr1a}$ neurons are activated by salt challenge (350 µL intraperitoneal injection of 2 M NaCl), a stimulus that rapidly increases plasma osmolarity and robustly triggers thirst (Figure 3.2a). This revealed extensive (70% ± 3% $Fos^+$ neurons were $GFP^+$) and specific (64% ± 7% $GFP^+$ neurons were $Fos^+$) co-localization between Fos induced by salt challenge and Agtr1a-GFP, suggesting that the *Agtr1a* gene may label thirst-promoting neurons in the OVLT. To gain genetic access to these cells, we generated a knockin mouse line that expresses Cre recombinase in frame with the endogenous *Agtr1a* gene (Agtr1a-2A-Cre mice; Figure 3.2b, Figure 3.6). Crossing this knockin line to a Cre-dependent GFP reporter line revealed recombination that was remarkably specifically localized to the OVLT relative to adjacent structures (Figure 3.2c, Figure 3.6). Neurochemical characterization by *in situ* hybridization revealed that $OVLT^{Agtr1a}$ neurons primarily

express Vglut2 (*Slc17a6*), but not Vgat (*Slc32a1*), indicating that these cells are predominantly glutamatergic (Figure 3.2j; see Figure 3.6 for additional discussion). Thus, the Agtr1a-2A-Cre mouse line provides genetic access to a specific population of OVLT neurons that are activated during thirst.

We next targeted ChR2 to OVLT$^{Agtr1a}$ neurons and positioned an optical fiber above the OVLT. Photostimulation of these cells induced robust water intake that was time-locked to the onset of stimulation (Figure 3.2d), specific to water relative to hypertonic NaCl (Figure 3.2e, f) and food (Figure 3.6), and absent from control mice. Photostimulation also caused a rapid and reversible increase in blood pressure (Figure 3.2g, Figure 3.6). These data indicate that OVLT$^{Agtr1a}$ neurons are sufficient to trigger homeostatic responses to fluid imbalance.

**Stimulation of OVLT$^{Agtr1a}$ neurons is negatively reinforcing**

We next investigated the motivational mechanisms by which OVLT$^{Agtr1a}$ neurons drive drinking behavior. We first trained mice to perform a fixed ratio 3 (FR3) task, in which delivery of each drop of water requires three presses of an active lever (Figure 3.2h). Photostimulation of OVLT$^{Agtr1a}$ neurons caused otherwise water-sated mice to vigorously and preferentially press the active lever to receive water (Figure 3.2h). Thus, stimulation of OVLT$^{Agtr1a}$ neurons drives instrumental responding for water, indicating that these cells promote drinking through a specific change in motivational state rather than through a general enhancement of activity or ingestive behavior. We then trained mice in the negative-reinforcement paradigm described above, which revealed that mice will selectively lever press to prevent photostimulation of OVLT$^{Agtr1a}$ neurons (Figure 3.2i). Thus, OVLT$^{Agtr1a}$ neurons, like SFO$^{GLUT}$ neurons, are activated by deviations from fluid homeostasis, are sufficient to generate robust thirst and cardiovascular responses, and motivate instrumental responding via negative reinforcement.

**MnPO$^{Adcyap1}$ neurons are activated by hyperosmolarity and receive input from the SFO and OVLT**

Signals from the SFO and OVLT are thought to converge on the MnPO[7,9,11]. To identify the MnPO neurons that control drinking behavior, we first identified several genes enriched in the MnPO relative to adjacent structures (including *Adcyap1*, *Agtr1a*, and *Slc17a6*), and then measured co-localization between these candidate markers and Fos induced by salt challenge (Figure 3.3a). This revealed that most Fos$^+$ MnPO neurons express Adcyap1 (81% ± 3%) and, conversely, that most Adcyap1$^+$ neurons express salt challenge-induced Fos (60% ± 4%). A similar, but somewhat lesser, degree of co-localization was observed between Fos and the markers *Agtr1a* and *Slc17a6* (Figure 3.3a). Consistent with these results, we found that most MnPO$^{Adcyap1}$ neurons express *Slc17a6* (Vglut2), but not *Slc32a1* (Vgat), indicating that these cells are predominantly glutamatergic (Figure 3.3b). These findings are supported by recent single-cell RNA sequencing data showing that *Adcyap1*, *Agtr1a*, and *Slc17a6* are all enriched in MnPO neurons that express Fos in response to dehydration[24].

To demonstrate that MnPO$^{Adcyap1}$ neurons receive input from other structures that drive drinking, we performed cell-type-specific retrograde tracing by targeting the monosynaptic rabies virus to MnPO$^{Adcyap1}$ neurons using an Adcyap-2A-Cre mouse (Figure 3.3c). This revealed that MnPO$^{Adcyap1}$ neurons receive strong, monosynaptic input from the SFO and OVLT (Figure 3.3c) as well as weaker input from several other structures (Figure 3.7). Thus, these cells are activated by salt challenge and receive direct input from the SFO and OVLT, strongly suggesting that they are involved in the control of drinking behavior.

**Stimulation of MnPO$^{Adcyap1}$ neurons drives drinking and hypertension**

To directly test the function of these cells, we targeted ChR2 to MnPO$^{Adcyap1}$ neurons and positioned an optical fiber above the MnPO (Figure 3.3d). Photostimulation of MnPO$^{Adcyap1}$

neurons caused rapid drinking behavior that was time-locked to the onset of stimulation (Figure 3.3e) and specific to water relative to hypertonic NaCl (Figure 3.3f) and food (Figure 3.7). Stimulation of MnPO$^{Adcyap1}$ neurons also caused a rapid and reversible increase in blood pressure (Figure 3.3g, Figure 3.7). None of these responses were observed in control mice expressing GFP in MnPO$^{Adcyap1}$ neurons (Figure 3.3e, g). We also observed no thermoregulatory response following stimulation of MnPO$^{Adcyap1}$ neurons (Figure 3.7), consistent with the dorsocaudal location of MnPO$^{Adcyap1}$ neurons relative to the VMPO$^{Adcyap1}$ neurons previously shown to regulate body temperature[25]. In addition, stimulation of the largely overlapping MnPO$^{Vglut2}$ neuron population (Figure 3.3b) recapitulated the behavioral effects of MnPO$^{Adcyap1}$ neuron stimulation (Figure 3.7). Thus, activation of MnPO$^{Adcyap1}$ neurons is sufficient to selectively drive the homeostatic responses to fluid imbalance.

**Stimulation of MnPO$^{Adcyap1}$ neurons is negatively reinforcing**

We next investigated the motivational mechanisms by which MnPO$^{Adcyap1}$ neurons drive drinking behavior. We first tested mice in an FR3 task, which revealed that photostimulation of MnPO$^{Adcyap1}$ neurons caused otherwise water-sated mice to vigorously and preferentially press the active lever to receive water (Figure 3.3h). This demonstrates that stimulation of MnPO$^{Adcyap1}$ neurons drives instrumental responding for water and therefore that these cells promote drinking through a specific change in motivational state.

To characterize the nature of this motivational signal, we measured the valence of MnPO$^{Adcyap1}$ neuron activity using a real-time, place-preference test in which mice were selectively photostimulated when they occupied one chamber of a two-chamber testing apparatus (Figure 3.3i). At baseline, ChR2 mice showed no preference between the two chambers, but upon testing they quickly developed a preference for the side without photostimulation (Figure 3.3i). In contrast, control mice developed no chamber preference

despite repeated testing (Figure 3.3i). This indicates that activation of MnPO$^{Adcyap1}$ neurons is aversive.

To determine whether this aversive signal is sufficient to motivate instrumental responding, we tested whether mice would lever press to block photostimulation of MnPO$^{Adcyap1}$ neurons (Figure 3.3j). We found that mice expressing ChR2 in MnPO$^{Adcyap1}$ neurons exhibited dramatic lever pressing that was specifically directed toward the active lever (Figure 3.3j). We observed similar operant responding to shut off stimulation of MnPO$^{Vglut2}$ neurons (Figure 3.7), whereas control mice showed little or no responding in any assay. Interestingly, mice engaged in significantly more vigorous and specific lever pressing to block stimulation of MnPO$^{Adcyap1}$ neurons compared to otherwise identical experiments involving upstream OVLT$^{Agtr1a}$ and SFO$^{GLUT}$ neurons (850 $\pm$ 190 MnPO$^{Adcyap1}$ versus 169 $\pm$ 51 SFO$^{GLUT}$ versus 134 $\pm$ 45 OVLT$^{Agtr1a}$, $^{****}P < 0.0001$). This suggests that these upstream signals may converge on the MnPO to generate an integrated motivational output.

**MnPO$^{Adcyap1}$ neuron projections dissociate the behavioral, affective, and cardiovascular output of these cells**

Little is known about how information about fluid balance exits the LT to engage downstream brain regions. SFO$^{GLUT}$ neurons promote thirst primarily through innervation of the other LT regions, the OVLT and MnPO, whereas they promote salt appetite through a projection to the bed nucleus of the stria terminalis (BNST)[16,17]. To investigate the downstream targets of thirst neurons in the MnPO, we performed anterograde tracing from MnPO$^{Adcyap1}$ neurons using a Cre-dependent AAV expressing synaptophysin-GCaMP6s (Figure 3.4a). This revealed innervation of a distributed set of downstream structures, including reciprocal projections to the SFO and OVLT (Figure 3.4b, Figure 3.8). Optogenetic stimulation of the retrograde MnPO$^{Adcyap1}\rightarrow$

SFO pathway was sufficient to induce drinking and increase blood pressure (Figure 3.8), suggesting that these reciprocal connections may functionally synchronize LT activity.

In addition to the SFO and OVLT, we found that MnPO$^{Adcyap1}$ neurons project to a number of other structures, including the paraventricular hypothalamus (PVH), supraoptic nuclei (SON), lateral hypothalamus (LH), paraventricular thalamus (PVT), arcuate nucleus (ARC), and dorsomedial hypothalamus (DMH) (Figure 3.4c, Figure 3.8). Anterograde tracing from MnPO$^{Vglut2}$ neurons revealed a similar set of projection targets (Figure 3.8). As these structures have been linked to ingestive behavior, valence, and cardiovascular regulation, they represent candidates to mediate the behavioral and autonomic effects of LT stimulation.

To probe the function of these pathways, we targeted ChR2 to MnPO$^{Adcyap1}$ neurons and positioned an optical fiber above the PVH, LH, or PVT to enable photostimulation of MnPO$^{Adcyap1}$ neuron terminals in these regions (Figure 3.4d, h, l). Stimulation of all three sites induced voracious drinking that was time-locked to the onset of stimulation and absent from control mice (Figure 3.4e, i, m). Photostimulation of terminals in the PVH and LH, but not the PVT, also induced a rapid increase in blood pressure (Figure 3.4f, j, n, Figure 3.8). This indicates that the effects of MnPO$^{Adcyap1}$ neuron activation on drinking and blood pressure can be anatomically dissociated.

We next investigated the motivational properties of these projections. Using a real-time, place-preference test, we found that photostimulation of terminals in the PVH and LH, but not the PVT, was aversive (Figure 3.4g, k, o). Surprisingly, the aversive signal was not strong enough to motivate lever pressing to shut off photostimulation of any of these structures (Figure 3.8). This may be, in part, because the valence of MnPO$^{Adcyap1}$ neuron activity is diluted as it is partitioned across multiple anatomic pathways (Figure 3.8). Taken together, these data reveal that the behavioral, motivational, and autonomic responses to fluid imbalance, which are unified within the LT, are differentially distributed as they exit the LT via projections of the MnPO.

## DISCUSSION

### Negative reinforcement is a mechanism that drives ingestive behavior

The nature of the motivational processes that drive eating and drinking has long been debated[1–5]. The drive-reduction hypothesis emphasized the fact that hunger and thirst are aversive states and therefore that animals may eat or drink to reduce this unpleasant sensation[4,5]. However, this idea was challenged by classic experiments showing that electrical stimulation of the LH, which promotes feeding, is rewarding rather than aversive[1,26,27]. Consistent with this, recent experiments have identified several neural populations that drive food intake and also support self-stimulation and, therefore, may act by positive reinforcement[28–30]. In contrast, although several neural cell types that promote eating or drinking have been shown to exhibit negative valence, none have yet been shown to support operant responding to reduce neural activity, which is the hallmark of negative-reinforcement learning. Thus, direct confirmation that neural circuits motivate ingestive behavior by this mechanism has been lacking.

We have shown here that stimulation of three different cell types distributed throughout the LT, as well as stimulation of projections connecting these neurons, is sufficient to drive drinking and, furthermore, that mice will perform operant tasks for the sole purpose of blocking stimulation of any of these neurons or projections. In addition, while this manuscript was in review, a separate study showed that stimulation of MnPO neurons that express Fos in response to dehydration drives drinking and is negatively reinforcing[24]. These findings strongly suggest that mice are motivated to find and consume water because they want to reduce the activity of thirst-promoting cells in the LT, consistent with the predictions of the drive-reduction hypothesis[4,5].

**The natural dynamics of the thirst circuit are consistent with a negative reinforcement mechanism**

Optogenetic manipulations can reveal the capabilities of a neural circuit, but the meaning of these manipulations can only be understood in the context of the natural dynamics of the circuit during behavior. While the optogenetic data presented here suggest that mice drink water to reduce the activity of their LT neurons, this interpretation requires that LT neurons are actually inhibited during the natural process of drinking.

We recently measured the natural dynamics of $SFO^{GLUT}$ neurons during drinking behavior and discovered that this is indeed the case[16]. $SFO^{GLUT}$ neurons are highly active when mice are thirsty and then become progressively inhibited each time a mouse takes a lick of water, which continues until the neurons return to baseline activity and drinking terminates[16]. This activity pattern is precisely what would be predicted for a neural population that motivates behavior by negative reinforcement[1]. Moreover, it was recently shown that vasopressin neurons in the PVH and SON, which are downstream of $SFO^{GLUT}$ neurons, display very similar dynamics during drinking[31], as do MnPO neurons that are activated by dehydration[24]. It therefore appears likely that the LT as a whole is regulated in this manner, consistent with the data presented here showing that each node shares common motivational properties.

While it may seem intuitive that a neuron driving ingestive behavior would be progressively inhibited during satiation, thereby gradually reducing an aversive drive, this result is not guaranteed. Indeed, it was long assumed that AgRP neurons that control hunger would display these dynamics during food intake, but they do not. AgRP neurons are instead inhibited the moment that a mouse detects food, and critically, they are not further inhibited during the course of eating[14,32,33]. Consistent with this result, the activity of AgRP neurons is not negatively reinforcing[14,29], but instead supports self-stimulation[29]. Thus, the data presented here reveal that

interoceptive neurons that control hunger and thirst utilize fundamentally different mechanisms to motivate behavior.

**The functional outputs of the LT are distributed along multiple anatomic pathways**

For more than 40 years, research into the neurobiology of thirst has focused on the LT[8–11,34]. These studies have established a critical role for the LT in a broad range of homeostatic responses, including not only thirst, but also salt appetite, blood pressure, and vasopressin release. What has remained unclear, however, is how information from the LT exits this circuitry to communicate with downstream brain regions that directly control the motor, cardiovascular, and motivational aspects of fluid homeostasis.

In this study, we have identified neurons in all three LT structures that are sufficient to drive the behavioral and autonomic responses to fluid imbalance. By obtaining genetic access to these cells, we have further been able to visualize their projections and test their function. Signals from the SFO and OVLT are thought to converge on the MnPO, and consistent with this, we have shown that stimulation of MnPO neurons has stronger motivational effects than stimulation of analogous cells in the SFO or OVLT. This suggests that MnPO activation is the mechanism by which these upstream structures generate valence, but it does not rule out more complex mechanisms involving other brain regions. Addressing this question will require further studies that map the functional connectivity between genetically defined cell types in these three structures and their downstream targets.

We have shown that MnPO$^{Adcyap1}$ neurons project broadly to brain regions outside the LT, suggesting that these cells may function as the output node of the LT thirst circuit. Stimulation of MnPO$^{Adcyap1}$ neuron projections innervating three structures (PVH, LH, and PVT) revealed that all three pathways are sufficient to drive drinking behavior, similar to recent observations for MnPO neurons that are activated by dehydration[24]. We found that these projections differ in their

ability to recapitulate the motivational/affective and cardiovascular responses to fluid imbalance. These results reveal that some functional outputs of the LT are anatomically segregated, whereas others are redundantly distributed. An important task for the future will be to identify and characterize the thirst-promoting cells in each of these downstream targets, in order to understand how the LT transforms chemical information about fluid balance into a coordinated, homeostatic response.

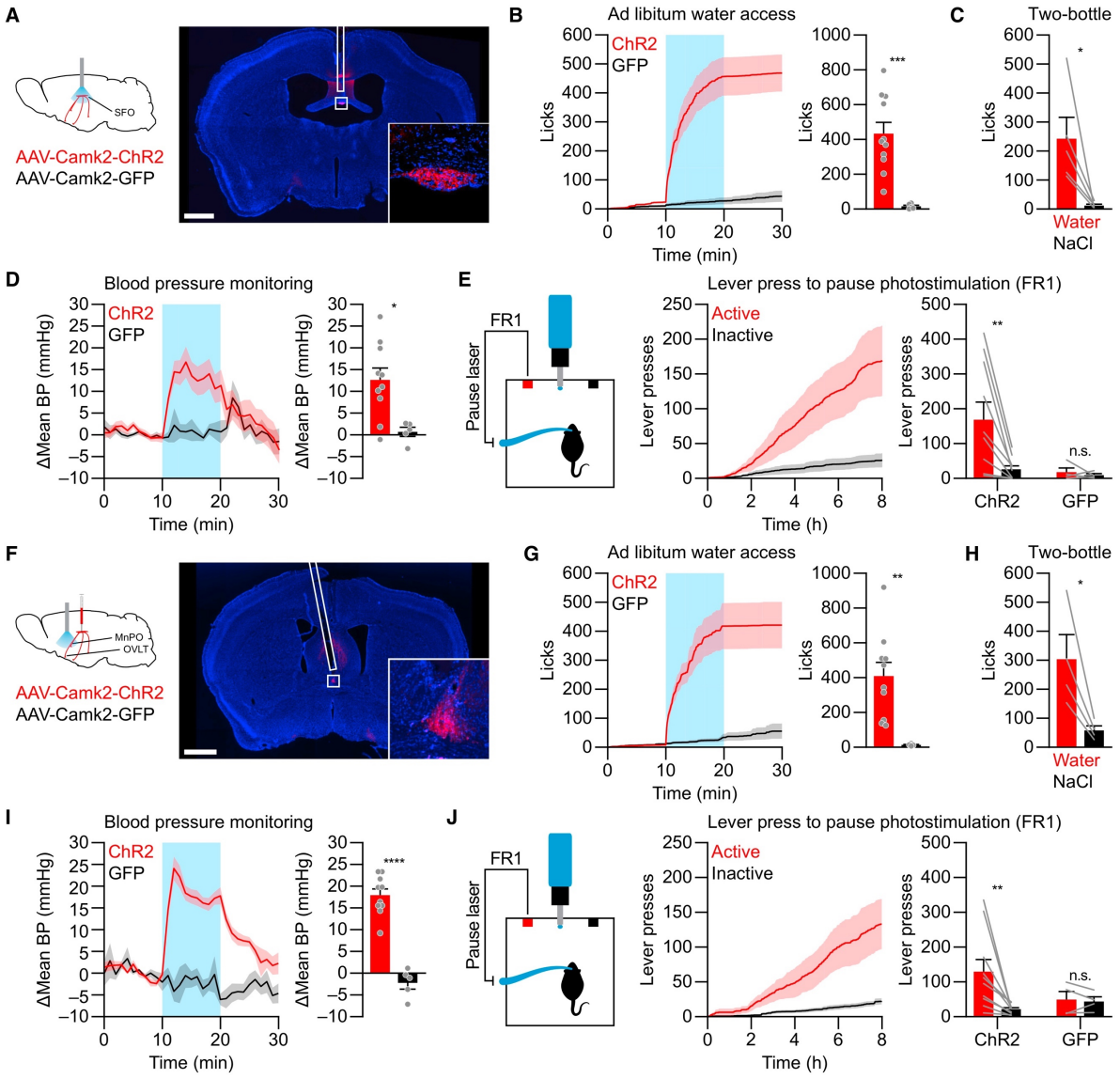


**Figure 3.1 | SFO thirst neurons are negatively reinforcing.**
**a**, Schematic of SFO$^{GLUT}$ neuron photostimulation (left). ChR2-mCherry expression and optical fiber placement (right; scale bar, 1 mm). **b**, Cumulative drinking (left) and total drinking during photostimulation (right) by ChR2 ($n$ = 11) and GFP ($n$ = 5) mice. **c**, Total drinking during photostimulation by ChR2 mice ($n$ = 5) with access to water and 0.3 M NaCl. **d**, Change in mean arterial blood pressure over time (left) and average photostimulation-induced change (right) for ChR2 ($n$ = 10) and GFP ($n$ = 5) mice. **e**, Schematic of negative-reinforcement experiment (left). Cumulative lever presses by ChR2 mice (middle). Total lever presses by ChR2 ($n$ = 10) and GFP ($n$ = 4) mice (right). **f**, Schematic of SFO$^{GLUT}$→MnPO/OVLT axon photostimulation (left). ChR2-mCherry expression and optical fiber placement (right; scale bar, 1 mm). **g**, Cumulative drinking (left) and total drinking during photostimulation (right) by ChR2 ($n$ = 10) and GFP ($n$ = 5) mice. **h**, Total drinking during photostimulation by ChR2 mice ($n$ = 4) with access to water and 0.3 M NaCl. **i**, Change in mean arterial blood pressure over time (left) and average photostimulation-induced change (right) for ChR2 ($n$ = 10) and GFP ($n$ = 5) mice. **j**, Schematic of negative-reinforcement experiment (left). Cumulative lever presses by ChR2 mice (middle). Total

lever presses by ChR2 ($n$ = 10) and GFP ($n$ = 4) mice (right). Values are reported as mean ± s.e.m. *$P$ < 0.05; **$P$ < 0.01; ***$P$ < 0.001; ****$P$ < 0.0001.

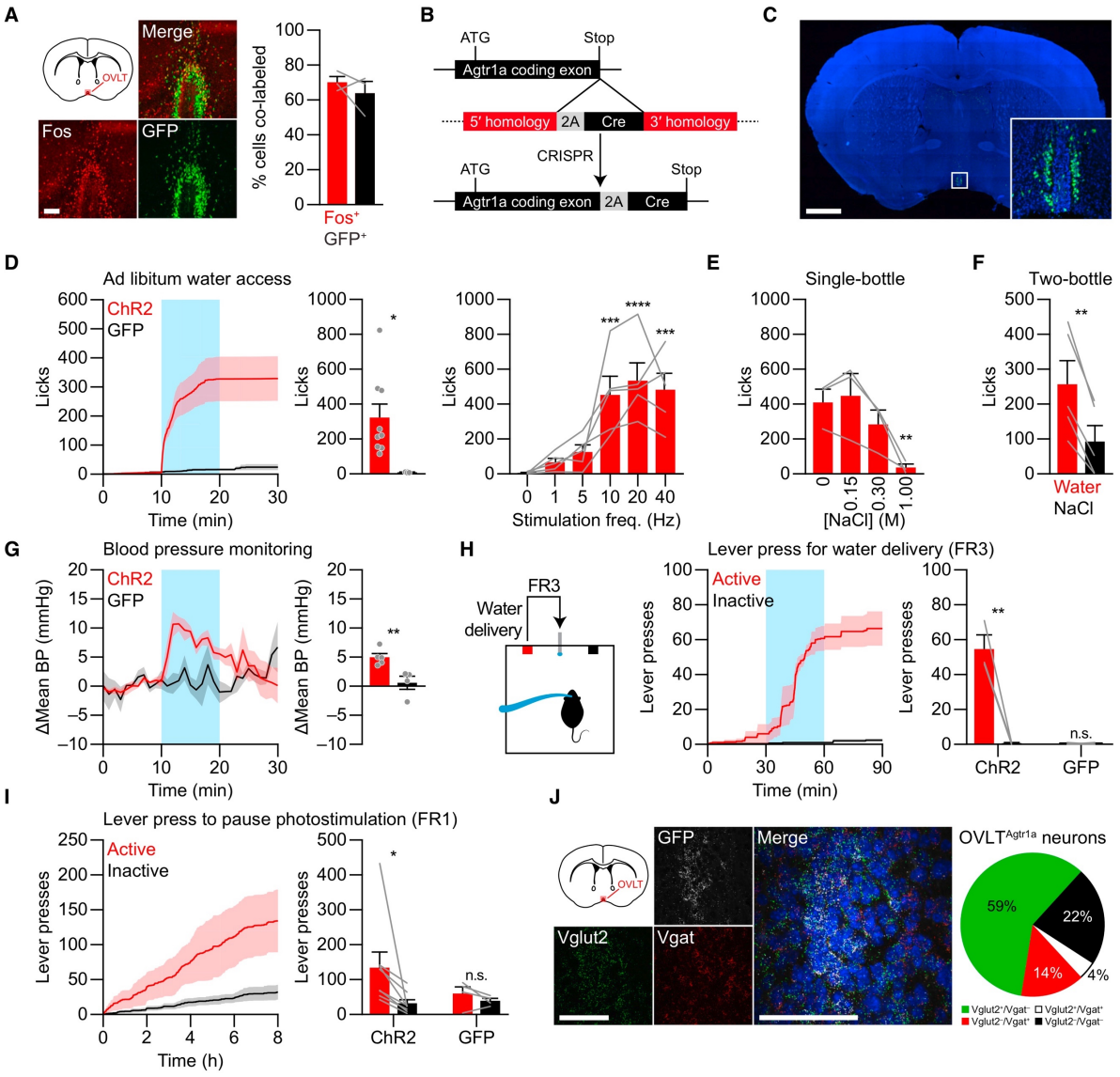


**Figure 3.2 | OVLT$^{Agtr1a}$ neurons drive thirst and hypertension and are negatively reinforcing.** **a**, Colocalization of Agtr1a-GFP and Fos induced by salt challenge in the OVLT of BAC transgenic mice (left; scale bar, 100 μm). Quantification (right; *n* = 3). **b**, Schematic for generation of Agtr1a-2A-Cre knockin mouse line by CRISPR-mediated homologous recombination. **c**, Histology showing GFP expression in the OVLT of Agtr1a-2A-Cre mice crossed to a GFP reporter line (scale bar, 1 mm). **d**, Cumulative drinking (left) and total drinking during photostimulation (middle) by ChR2 (*n* = 8) and GFP (*n* = 4) mice. Total drinking during photostimulation by ChR2 mice (*n* = 5) at different photostimulation frequencies (right). **e**, Total drinking during photostimulation by ChR2 mice (*n* = 3) with access to various NaCl solutions. **f**, Total drinking during photostimulation by ChR2 mice (*n* = 5) with access to water and 0.3 M NaCl. **g**, Change in mean arterial blood pressure over time (left) and average photostimulation-induced change (right) for ChR2 (*n* = 5) and GFP (*n* = 4) mice. **h**, Schematic of instrumental responding for water access experiment (left). Cumulative lever presses by ChR2 mice (middle). Total lever presses during photostimulation by ChR2 (*n* = 3) and GFP (*n* = 3) mice (right). **i**, Cumulative lever presses by ChR2 mice in the negative-reinforcement experiment (left). Total

lever presses by ChR2 ($n$ = 8) and GFP ($n$ = 4) mice (right). **j**, RNAscope *in situ* hybridization showing colocalization of GFP, Vglut2, and Vgat mRNA in the OVLT of Agtr1a-2A-Cre mice crossed to a GFP reporter line (left; scale bars, 100 μm). Quantification (right; $n$ = 201 cells from 2 mice). Values are reported as mean ± s.e.m. $^{*}P < 0.05$; $^{**}P < 0.01$; $^{***}P < 0.001$; $^{****}P < 0.0001$.

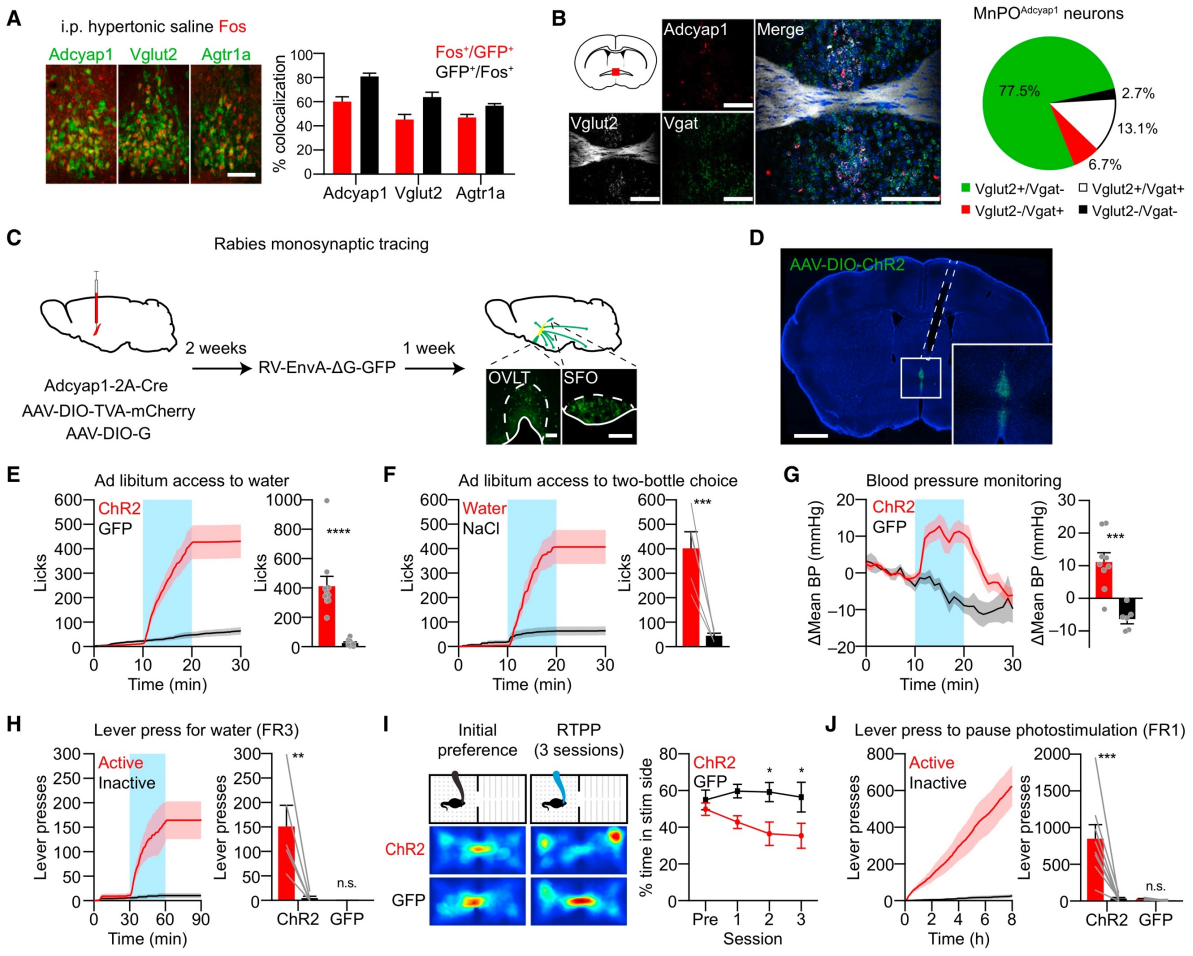


**Figure 3.3 | MnPO thirst neurons are negatively reinforcing.**
**a**, Colocalization of Fos with Adcyap1 (*n* = 4), Vglut2 (*n* = 3), and Agtr1a (*n* = 3) in the MnPO following salt challenge. Scale bar, 30 µm. **b**, RNAscope *in situ* colocalization of Adcyap1, Vglut2, and Vgat (left; scale bars, 200 µm). Quantification (right, *n* = 239 cells from 3 mice). **c**, Monosynaptic retrograde rabies tracing from MnPO$^{Adcyap1}$ neurons. Scale bars, 200 µm. **d**, Injection site and fiber placement (dashed line) in MnPO$^{Adcyap1}$ ChR2 mice. Scale bar, 1 mm. **e**, Cumulative drinking (left) and total drinking during photostimulation (right) by ChR2 (*n* = 10) and GFP (*n* = 9) mice. **f**, Cumulative drinking (left) and total drinking during photostimulation (right) by ChR2 mice (*n* = 5) during two-bottle choice assay with water and 0.3 M NaCl. **g**, Change in mean arterial blood pressure over time (left) and average photostimulation-induced change (right) in ChR2 (*n* = 9) and GFP (*n* = 6) mice. **h**, Cumulative lever pressing for water by ChR2 mice (*n* = 5) (left) and total lever presses during photostimulation by ChR2 (*n* = 5) and GFP (*n* = 3) mice (right). **i**, Real-time, place-preference assay with location heatmaps of individual ChR2 and GFP mice from pre-conditioning and third session of conditioning (left). Percent time spent in photostimulation-paired chamber by ChR2 (*n* = 6) and GFP (*n* = 6) mice (right). **j**, Cumulative lever pressing to pause photostimulation by ChR2 mice (*n* = 8) (left). Lever presses by ChR2 (*n* = 8) and GFP (*n* = 4) mice in the negative-reinforcement experiment (right). Values are reported as mean ± s.e.m. **P* < 0.05, ***P* < 0.01, ****P* < 0.001, *****P* < 0.0001.

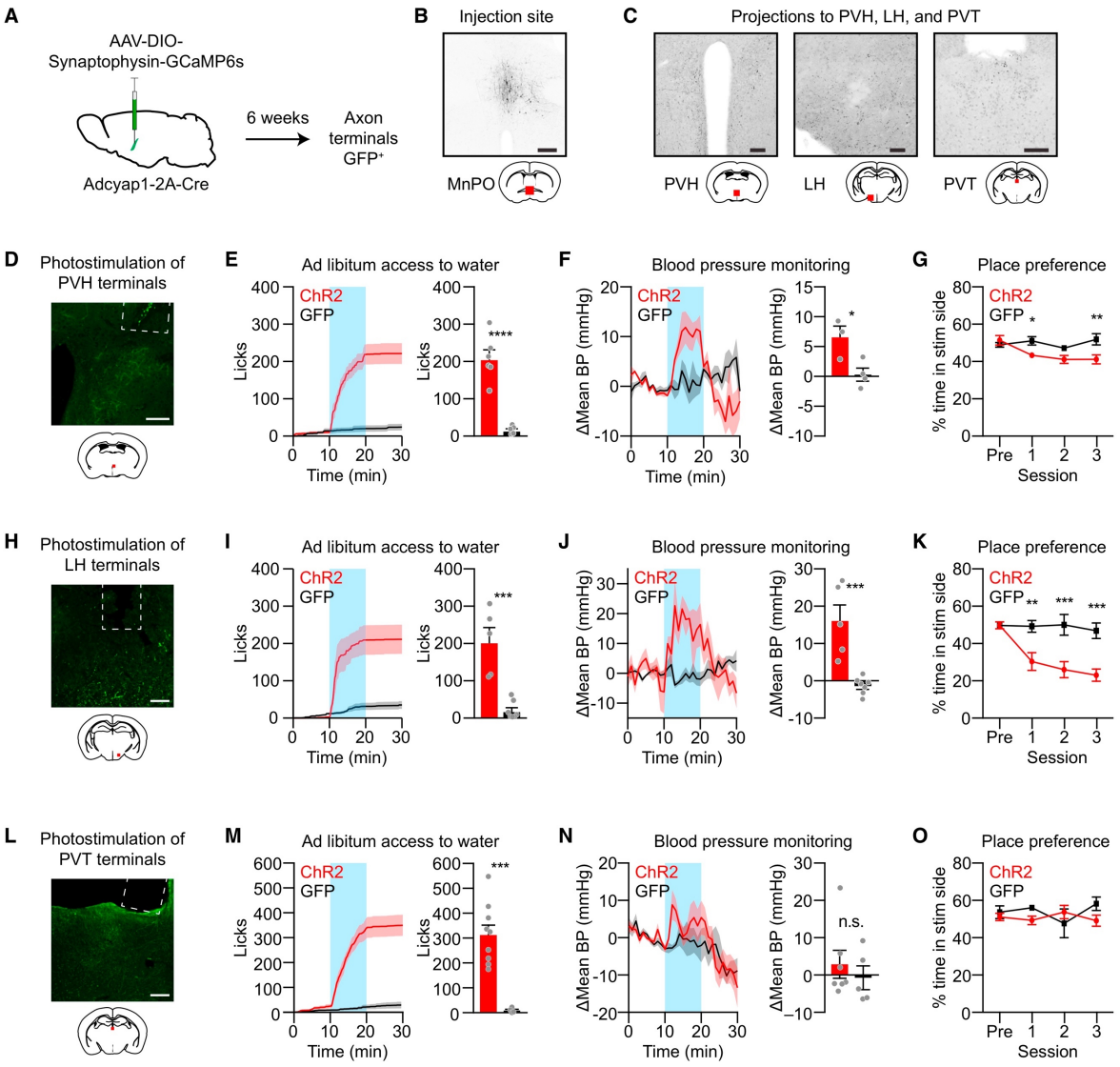


**Figure 3.4 | MnPO$^{Adcyap1}$ neuron projections dissociate the behavioral, affective, and cardiovascular effects of dehydration.**

**a**, Anterograde tracing strategy. **b**, Example injection site. Scale bar, 200 µm. **c,** MnPO$^{Adcyap1}$ projections to PVH, LH, and PVT. Scale bars, 100 µm. **d**, **h**, **l**, Implant sites (dashed lines) above the PVH (**d**), LH (**e**), and PVT (**l**). Scale bars, 100 µm. **e**, **i**, **m**, Cumulative drinking (left) and total drinking during photostimulation (right) for terminal stimulation in the PVH (**e**; $n$ = 6 ChR2, $n$ = 5 GFP), LH (**i**; $n$ = 5 ChR2, $n$ = 7 GFP), and PVT (**m**; $n$ = 9 ChR2, $n$ = 4 GFP). **f**, **j**, **n**, Change in mean arterial blood pressure over time (left) and average photostimulation-induced change (right) for terminal stimulation in the PVH (**f**; $n$ = 3 ChR2, $n$ = 5 GFP), LH (**j**; $n$ = 5 ChR2, $n$ = 7 GFP), and PVT (**n**; $n$ = 7 ChR2, $n$ = 5 GFP). **g**, **k**, **o**, Percent time spent in photostimulation-paired chamber for terminal stimulation in the PVH (**g**; $n$ = 4 ChR2, $n$ = 5 GFP), LH (**k**; $n$ = 5 ChR2, $n$ = 7 GFP), and PVT (**o**; $n$ = 5 ChR2, $n$ = 4 GFP). Values are reported as mean ± s.e.m. *$P$ < 0.05, **$P$ < 0.01, ***$P$ < 0.001, ****$P$ < 0.0001.

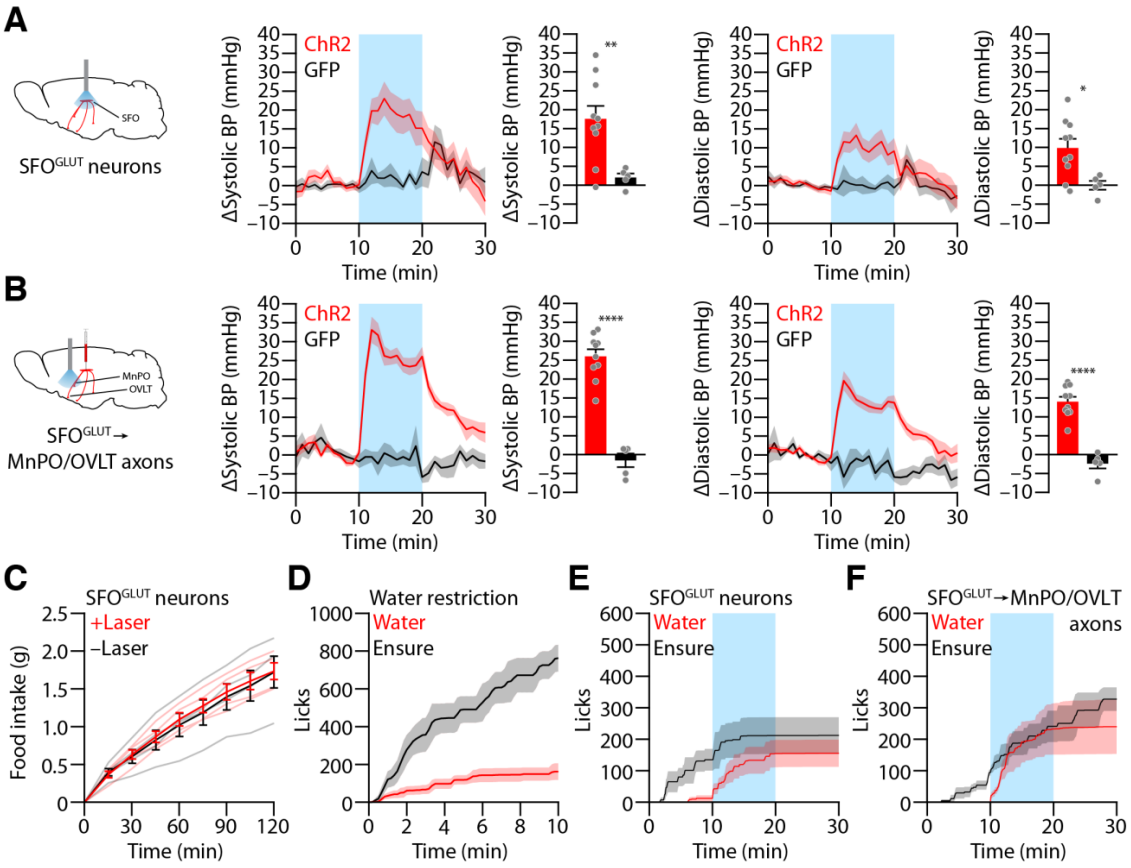


**Figure 3.5 | Photostimulation of SFO$^{GLUT}$ neurons increases blood pressure but has no effect on food intake.**

**a**, **b**, Photostimulation of SFO$^{GLUT}$ neurons (**a**; $n$ = 11 ChR2, $n$ = 5 GFP) and SFO$^{GLUT}$→MnPO/OVLT axons (**b**; $n$ = 10 ChR2, $n$ = 5 GFP) increases systolic and diastolic blood pressure in ChR2 but not GFP mice. **c**, Photostimulation of SFO$^{GLUT}$ neurons ($n$ = 4) does not influence fasting-induced feeding. **d**, Drinking of water and Ensure in a two-bottle assay following 24-h water restriction ($n$ = 4). **e**, **f**, Drinking of water and Ensure in a two-bottle assay with photostimulation of SFO$^{GLUT}$ neurons (**e**; $n$ = 5) or SFO$^{GLUT}$→MnPO/OVLT axons (**f**; $n$ = 4). Values are reported as mean ± s.e.m. *$P$ < 0.05, **$P$ < 0.01, ****$P$ < 0.0001.

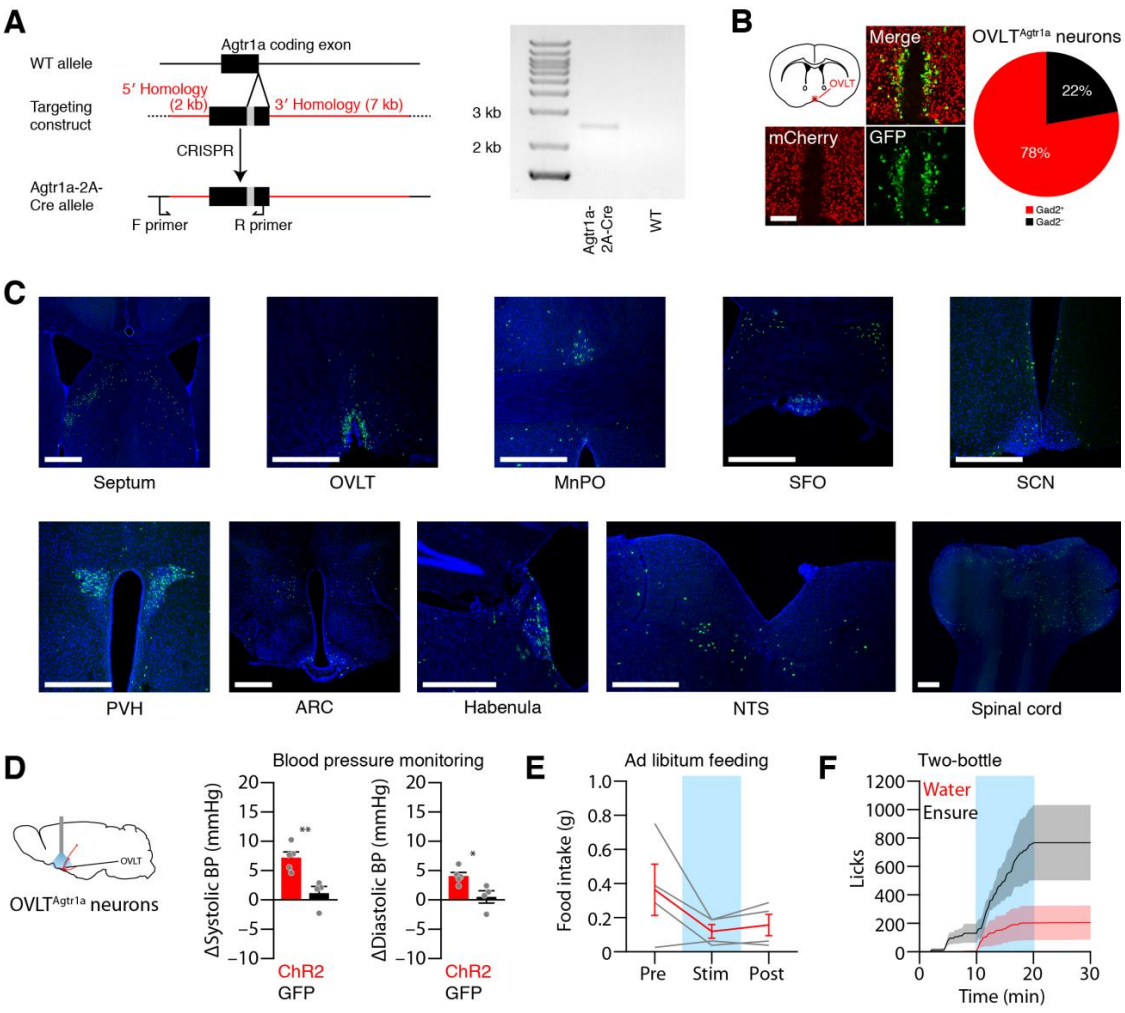


**Figure 3.6 | Characterization of the Agtr1a-2A-Cre mouse line and additional OVLT$^{Agtr1a}$ photostimulation experiments.**

**a**, Presence of the Agtr1a-2A-Cre knock-in allele was verified by long range PCR (expected amplicon size 2496 bp) using a forward PCR primer located in the wild type mouse genome upstream of targeting construct 5′ homology arm and a reverse PCR primer located in the Cre sequence. **b**, Histology showing colocalization of Agtr1a::GFP and Gad2::mCherry in the OVLT of Agtr1a-2A-Cre mice crossed to both a GFP reporter line and a Gad2-mCherry line (left; scale bar, 100 µm). Quantification (right; $n$ = 176 cells from 1 mouse). This suggests that while the majority of OVLT$^{Agtr1a}$ neurons are glutamatergic (Figure 3.2j), many of these cells also express components of the GABA synthesis pathway (but not Vgat). This is consistent with recent single-cell sequencing data indicating that many hypothalamic cell types co-express glutamatergic and GABAergic markers[35]. **c**, Brain-wide atlas of Agtr1a expression from Agtr1a-2A-Cre mice crossed to a GFP reporter line (scale bars, 500 µm). We also observed sparse labeling throughout other brain regions. **d**, Photostimulation of OVLT$^{Agtr1a}$ neurons ($n$ = 5 ChR2 mice; $n$ = 4 GFP mice) increases systolic and diastolic blood pressure in ChR2 but not GFP mice. **e**, Photostimulation of OVLT$^{Agtr1a}$ neurons ($n$ = 4) does not influence ad libitum feeding. **f**, Drinking of water and Ensure in a two-bottle assay with photostimulation of OVLT$^{Agtr1a}$ neurons ($n$ = 4). ARC, arcuate nucleus; MnPO, median preoptic nucleus; NTS, nucleus of the solitary tract; OVLT, organum vasculosum of the lamina terminalis; PVH, paraventricular nucleus of the hypothalamus; SCN,

suprachiasmatic nucleus; SFO, subfornical organ. Values are reported as mean ± s.e.m. $^{*}P < 0.05$, $^{**}P < 0.01$.

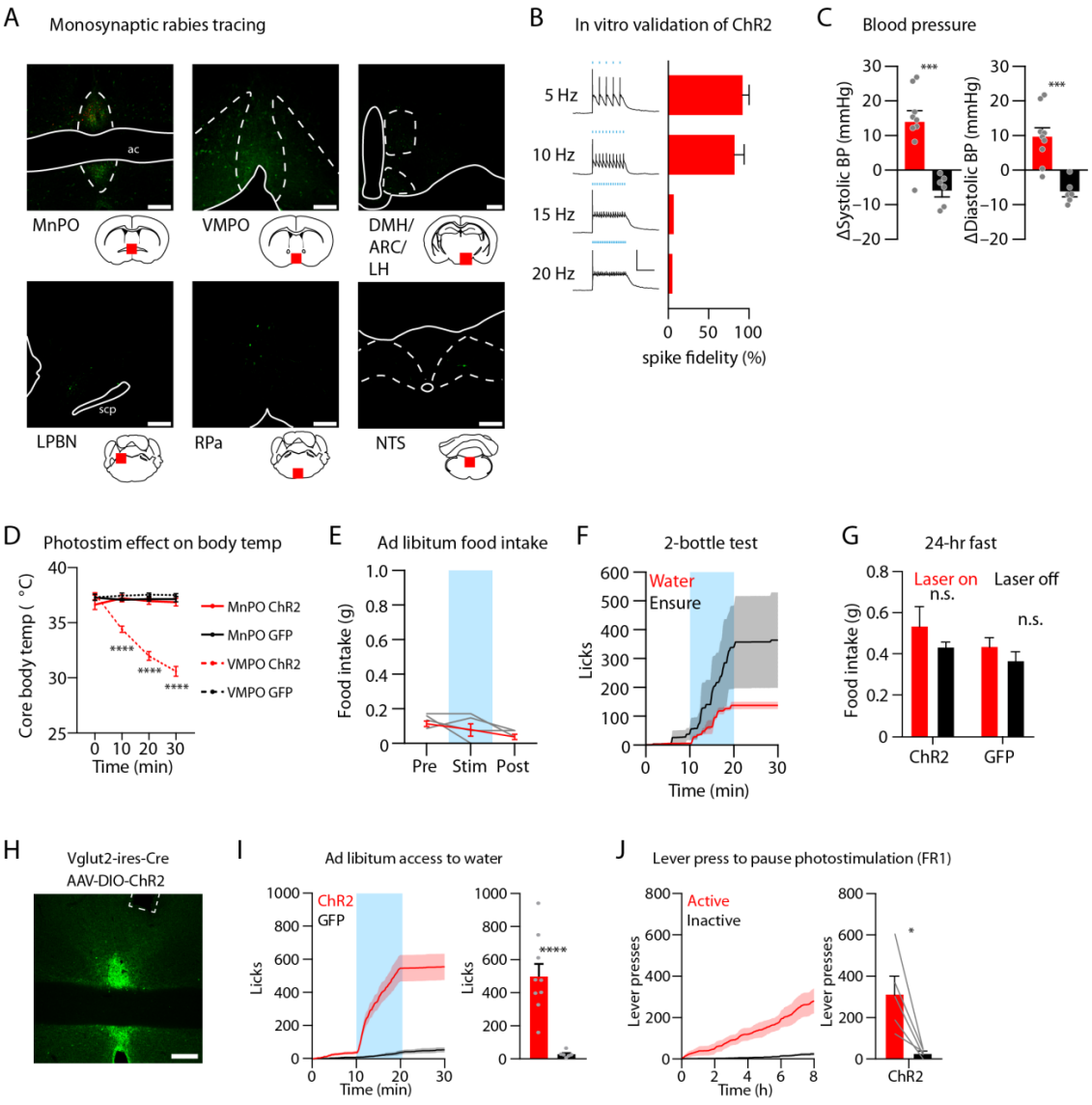


**Figure 3.7 | Additional characterization of MnPO$^{Adcyap1}$ and MnPO$^{Vglut2}$ neurons.**
**a**, Example injection site for monosynaptic rabies tracing from MnPO$^{Adcyap1}$ neurons (top left) and additional monosynaptic inputs to MnPO$^{Adcyap1}$ neurons. Helper virus is shown in red; rabies in green. All images representative of 3 mice, except NTS (1 cell/3 mice). Scale bars, 200 μm. **b**, In vitro electrophysiological validation of ChR2 activation of MnPO$^{Adcyap1}$ neurons ($n$ = 10 cells per frequency). Scale bar, 50 mV and 0.5 s. **c**, Effect of photostimulation of MnPO$^{Adcyap1}$ neurons ($n$ = 9 ChR2, $n$ = 6 GFP) on systolic and diastolic blood pressure. **d**, Core body temperature during photostimulation of MnPO$^{Adcyap1}$ ChR2 ($n$ = 4), MnPO$^{Adcyap1}$ GFP ($n$ = 4), VMPO$^{Adcyap1}$ ChR2 ($n$ = 5), and VMPO$^{Adcyap1}$ GFP ($n$ = 3) mice. **e**, Effect of photostimulation of MnPO$^{Adcyap1}$neurons ($n$ = 4) on ad libitum food intake. **f**, Effect on water and Ensure consumption in a two-bottle assay of photostimulation of MnPO$^{Adcyap1}$ neurons ($n$ = 3). **g**, Food intake after 24-h food deprivation with and without photostimulation of MnPO$^{Adcyap1}$ neurons targeted with ChR2 ($n$ = 4) and GFP ($n$ = 4). **h**, Expression of ChR2 at the injection site in MnPO$^{Vglut2}$ mice. Implant site is indicated by dashed lines. Scale bar, 200 μm. **i**, Cumulative drinking (left) and total drinking during photostimulation (right) by MnPO$^{Vglut2}$ ChR2 ($n$ = 9) and GFP ($n$ = 6) mice. **j**, Cumulative lever

pressing to pause photostimulation (left) and total lever presses during photostimulation (right) by $MnPO^{Vglut2}$ ChR2 mice ($n$ = 5) (left). Total lever presses by ChR2 ($n$ = 5) mice. Values are reported as mean ± s.e.m. *$P$ < 0.05, ***$P$ < 0.001, ****$P$ < 0.0001.

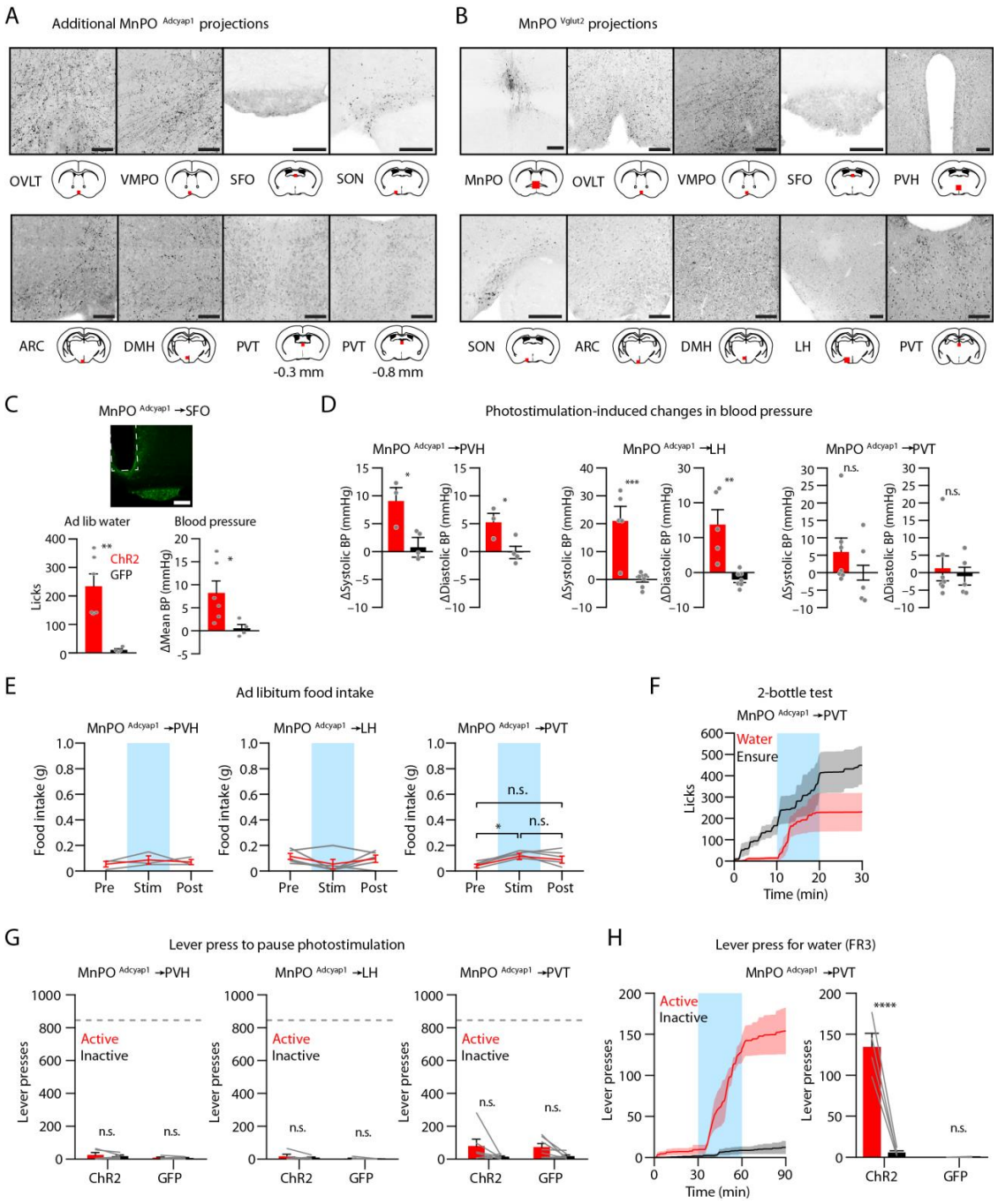


**Figure 3.8 | MnPO$^{Adcyap1}$ and MnPO$^{Vglut2}$ projections and terminal photostimulation.** **a**, Additional MnPO$^{Adcyap1}$ projections labeled by AAV-DIO-synaptophysin-GCaMP6s. Scale bars, 100 µm. **b**, MnPO$^{Vglut2}$ injection site (top left; scale bar, 200 µm) and projections (remaining panels; scale bars, 100 µm). All images are representative of 3 mice. **c**, Implant site (dashed lines) for terminal stimulation of MnPO$^{Adcyap1}$ axons in the SFO. Scale bar, 100 µm. **d**, Effects on systolic and diastolic blood pressure of photostimulation of MnPO$^{Adcyap1}$ axons in PVH (left; $n$ = 3 ChR2, $n$ = 4 GFP), LH axon photostimulation (middle; $n$ = 5 ChR2, $n$ = 7 GFP mice), and PVT (right; $n$ = 7 ChR2, $n$ = 5 GFP). **e**, Effect on ad libitum food intake of photostimulation of MnPO$^{Adcyap1}$ axons in PVH (left; $n$ = 3), LH (middle; $n$ = 5), and PVT (right; $n$ = 5). **f**, Effect on consumption of

water and Ensure of photostimulation of MnPO$^{Adcyap1}$ axons in PVT ($n$ = 4). **g**, Lever presses to pause photostimulation of MnPO$^{Adcyap1}$ axons in PVH (left; $n$ = 5 ChR2, $n$ = 5 GFP), LH (middle; $n$ = 5 ChR2, $n$ = 7 GFP), and PVT (right; $n$ = 6 ChR2, $n$ = 7 GFP). The dashed lines indicate the average number of active lever presses in the same experiment for MnPO$^{Adcyap1}$ cell body photostimulation. **h**, Cumulative lever pressing for water delivery (left) and total lever presses during photostimulation (right) by MnPO$^{Adcyap1}\rightarrow$PVT ChR2 mice ($n$ = 4). Values are reported as mean ± s.e.m. $^{*}P < 0.05$, $^{**}P < 0.01$, $^{***}P < 0.01$, $^{****}P < 0.0001$.

## METHODS

Experimental protocols were approved by the University of California, San Francisco IACUC following the NIH Guide for the Care and Use of Laboratory Animals.

### Reagents

Wild-type mice (C57BL/6J, strain 000664), Slc17a6-IRES-Cre mice (Slc17a6$^{tm2(cre)Lowl}$/J, strain 016963), Nos1-IRES-Cre mice (Nos1$^{tm1(Cre)Mgmj}$, strain 017526), Gad2-2A-NLS-mCherry mice (B6;129S-Gad2$^{tm1.1Ksvo}$/J, strain 023140), Rosa26-LSL-hChR2(H134R)-eYFP mice (Ai32; B6.129S-Gt(ROSA)26Sor$^{tm32(CAG-COP4*H134R/EYFP)Hze}$/J, strain 012569), Rosa26-LSL-LSL-ArchT-eGFP (Ai40D; B6.Cg-Gt(ROSA)26Sor$^{tm40.1(CAG-aop3/EGFP)Hze}$/J, strain 021188), and Rosa26-LSL-GFPL10 mice (B6.129S4-Gt(ROSA)26Sor$^{tm1(CAG-EGFP/Rpl10a,-birA)Wtp}$/J, strain 022367) were obtained from the Jackson Laboratory. Adcyap1-2A-Cre mice were obtained from the Allen Institute. Agtr1a-GFP mice (Tg(Agtr1aEGFP)NZ44Gsat, strain 033059) were obtained from MMRRC.

All animals were maintained on a 12-h light/dark cycle and given ad libitum access to chow (PicoLab Rodent Diet 5053) and water. All transgenic mice used in these studies were on the C57BL/6J background, except Agtr1a-2A-Cre mice that were maintained on a mixed FVB/C57BL/6J background. Unless otherwise stated, all studies employed a mixture of male and female mice and no differences between sexes were observed. All procedures were conducted during the light cycle unless otherwise noted.

Recombinant AAVs expressing hChR2(H134R) (AAV5-Ef1a-DIO-hChR2(H134R)-eYFP), hChR2(E123T/T159C) (AAV5-Camk2-hChR2(E123T/T159C)-2A-mCherry, AAV5-Ef1a-DIO-hChR2(E123T/T159C)-2A-mCherry), and GFP (AAV5-Camk2-GFP) were obtained from the UNC Vector Core. Recombinant EnvA-pseudotyped G-deficient rabies virus expressing GFP (RV-EnvA-ΔG-GFP) was obtained from the Salk Institute. Plasmids encoding synaptophysin-GCaMP6s and GFP-RPL10a fusion proteins were generated in-house, and recombinant AAVs

containing these plasmids (AAV5-EF1a-DIO-synaptophysin-GCaMP6s; AAV2-EF1a-FLEX-GFP-RPL10a) were commercially produced by the UNC Vector Core[16,25]. Rabies helper viruses (AAV1-CAG-DIO-TVA-mCherry; AAV1-CAG-DIO-G) were obtained from the laboratory of N. Shah.

**Generation of the Agtr1a-2a-Cre mouse line**

The bicistronic Agtr1a-2A-Cre allele was generated by homologous recombination at the endogenous *Agtr1a* locus, aided by targeted CRISPR endonuclease activity. Briefly, homology regions were captured into a plasmid from a BAC containing the *Agtr1a* locus by recombineering. The T2A-Cre sequence was inserted immediately upstream of the endogenous stop codon. The final targeting vector contained ~2 kb (5′) and ~7 kb (3′) homology arms and was verified by restriction digest and sequencing. To generate site-specific double stranded breaks using CRISPR, an sgRNA sequence (TTGTTCTGAGGTGGAGTGAC) was selected such that the guide sequence would be separated from the PAM site in the genomic DNA by the 2A-Cre insertion. This ensured that the targeting vector and recombined *Agtr1a-2a-Cre* allele were protected from Cas9 nuclease activity. Super-ovulated female FVB/N mice were mated to FVB/N stud males, and fertilized zygotes were collected from oviducts. Cas9 protein (100 ng/μL), sgRNA (250 ng/μL) and targeting vector DNA (100 ng/μL) were mixed and injected into the pronucleus of fertilized zygotes. 125 injected zygotes were implanted into oviducts of pseudopregnant CD1 female mice. 18 out of 35 pups genotyped were positive for the knock-in allele, and 16 of these also contained the targeting vector inserted randomly as a transgene. Two independent knock-in lines were crossed to reporter mice, and reporter expression patterns from these lines were identical. All Agtr1a-2A-Cre mice used here were maintained on mixed FVB/C57BL/6J background. Founder pups and offspring were genotyped for the presence of the knock-in allele by qPCR. Presence of the knock-in allele was also verified by long range PCR (expected amplicon size 2496 bp) using a forward PCR primer upstream of the 5′ homology arm

(CGAGCCTGTGAGGTTAAAGAT) and a reverse PCR primer inside the Cre sequence (GCGCGCCTGAAGATATAGAA).

**Stereotaxic surgery**

Surgeries were conducted on a stereotaxic frame (Kopf). Mice were anesthetized with isoflurane and received bupivacaine, carprofen, and buprenorphine during surgery in accordance with UCSF IACUC guidelines. Injections were performed with pulled glass pipets and 10-µL Hamilton syringes controlled by a micropump (Kopf). Homemade fiberoptic implants were secured to the skull with Vetbond (SCB, sc-361931) and dental cement (A-M Systems, 526000). Following surgery, incisions were closed using Vetbond.

All SFO virus injections were in wild type mice (unless otherwise noted) using the following coordinates: 0 mm M/L, –0.50 mm A/P, –2.75 mm below the surface of the skull. Implants above the SFO were placed using the same coordinates but –2.45 mm below the surface of the skull. Implants above the MnPO were placed at the following coordinates: 0 mm M/L, +0.45 mm A/P,–3.70 mm below the surface of the skull. Wild-type mice were injected with 100–200 nL of AAV5-Camk2-hChR2(E123T/T159C)-2A-mCherry or AAV5-Camk2-GFP. For fasting-refeeding experiments, Nos1-IRES-Cre mice were injected with 100–200 nL of AAV5-Ef1a-DIO-hChR2(E123T/T159C)-2A-mCherry.

All OVLT virus injections were in Agtr1a-2A-Cre mice using the following coordinates: 0 mm M/L, +0.40 mm A/P, and –4.75 mm below the surface of the skull. Implants above the OVLT were placed using the same coordinates but –4.55 mm below the surface of the skull. Mice intended for optogenetics experiments were injected with 100 nL of AAV5-Ef1a-DIO-hChR2(H134R)-eYFP ($n$ = 6 mice) or crossed to the Rosa26-LSL-hChR2(H134R)-eYFP reporter line ($n$ = 3 mice). Control mice were crossed to the Rosa26-LSL-GFP-RPL10 reporter line.

All MnPO virus injections were in Adcyap1-2a-Cre mice (unless otherwise noted), angled at 15°, and used the following coordinates: +1.0 mm M/L, +0.45 mm A/P, –4.3 mm below the surface of the skull. Implants above the MnPO were placed using the same angle and coordinates but –3.7 mm below the surface of the skull. Implants for MnPO projection stimulation were placed at the following coordinates: PVH (no angle, –0.3 mm M/L, –0.6 mm A/P, –4.75 mm below the surface of the skull); LH (no angle, –1.0 mm M/L, –1.4 mm A/P, –5.0 mm below the surface of the skull); PVT (15°, +0.8, –0.9 mm A/P, –3.2 mm below the surface of the skull); SFO (15°, +0.8 mm M/L, –0.55 mm A/P, –2.6 mm below the surface of the skull). For Fos/GFP colocalization, 1500 nL of AAV2-Ef1a-FLEX-GFP-RPL10a was injected into Adcyap1-2A-Cre or Vglut2-IRES-Cre mice. Mice intended for optogenetics experiments were injected with 100 nL of AAV5-Ef1a-DIO-hChR2(H134R)-eYFP or AAV2-Ef1a-FLEX-GFP-RPL10a. For rabies tracing, 75 nL of a 1:1 mix of AAV1-CAG-DIO-TVA-mCherry and AAV1-CAG-DIO-G was injected. After two weeks, 200 nL of recombinant EnvA-pseudotyped G-deficient rabies virus expressing GFP was injected. After one additional week, mice were euthanized and processed for histology. For anterograde tracing, 50 nL of AAV5-Ef1a-DIO-synaptophysin-GCaMP6s was injected.

**GFP-reporter labeling and cell counts**

To quantify Fos/GFP overlap, 20× Z stack images from 40-μm coronal slices (bregma +0.1 to +0.2 mm) were taken, and the numbers of Fos/GFP double positive or singly positive cells were counted in Fiji.

**Virus validation by acute slice electrophysiology**

Acute hypothalamic slices were prepared from Adcyap1-2A-Cre mice expressing AAV5-Ef1a-DIO-hChR2(H134R)-eYFP as previously described[16]. Briefly, spike fidelity was measured in current clamp with LED light stimulation at 5, 10, 15, and 20 Hz.

**Photostimulation *in vivo***

All experiments were performed in behavioral chambers (Coulbourn Instruments, Habitest Modular System), and water consumption was monitored with contact lickometers[36]. Mice were acclimated to the behavioral chamber for at least 15 min before the beginning of each testing session. For SFO and OVLT optogenetics experiments, mice were photostimulated with 10-ms pulses at 10 Hz and 10–15 mW laser power, measured from the tip, using a DPSS 473-nm laser (Shanghai Laser and Optics Century), except for negative-reinforcement experiments (5 Hz and 10–15 mW laser power) and fasting-refeeding experiments (20 Hz and 10–15 mW laser power). For MnPO soma, MnPO$^{Adcyap1}$→PVT, and MnPO$^{Adcyap1}$→SFO optogenetics experiments, mice were photostimulated with 10-ms pulses at 5 Hz and 5–10 mW laser power. For MnPO$^{Adcyap1}$→PVH optogenetics experiments, mice were stimulated at 10 Hz and 10 mW. For MnPO$^{Adcyap1}$→LH optogenetics experiments, mice were stimulated at 20 Hz and 20 mW. The increases in frequency in PVH/LH and laser power in LH photostimulation were the minimum to produce reliable drinking in these mice. To test whether acute photostimulation could induce drinking, mice were provided with constant access to water and monitored for 10 min (pre-stim), then photostimulated for 10 min, and then monitored for another 10 min (post-stim). For NaCl drinking experiments, the same model was used except that mice were provided with access to various NaCl solutions. For negative-reinforcement experiments, mice were photostimulated constantly during the dark cycle. Pressing the active lever turned off the laser for 10 s. For lever pressing for water reward, mice were first trained to receive 5 μL of water for one active lever press (FR1) for at least three nights and then for 3 active lever presses (FR3) for three nights. Then, during the light cycle, lever presses were measured during 30-min pre-stim, stim, and post-stim periods. For SFO$^{GLUT}$ fasting-refeeding experiments, mice were food deprived for 24 h, then given access to food and water. For ad libitum feeding experiments, mice were given access to food but not water, and their food intake was measured during 30-min pre-stim, stim,

and post-stim periods. For MnPO$^{Adcyap1}$ fasting-refeeding experiments, mice were food deprived for 24 h then given access to food but no water for 30 min.

**Blood pressure measurements**

For blood pressure measurements, mice were sedated with medetomidine (50 µg/kg, ApexBio). The sedated mice were then restrained, placed on a warming platform, and their blood pressure measured using the CODA-HT4 Noninvasive Blood Pressure System (Kent Scientific). After a 10-min habituation period, blood pressure was measured once per minute during 10-min pre-stim, stim, and post-stim periods. Data were analyzed using an in-house MATLAB script that subtracted baseline blood pressure for each mouse and compared the change in blood pressure from the pre-stim to stim periods (averaged during the 4$^{th}$ to 10$^{th}$ minute of each period).

**Real-time, place-preference**

A custom two-chamber apparatus (30 cm × 15 cm) was used. The two sides differed in floor texture and wall markings, and the mice were free to move between both sides throughout all experiments. First, baseline preference was recorded for 15 min. During 15 min sessions on the next 3 days, a custom MATLAB script was used to track the mice and pair one side of the chamber with photostimulation. Using a custom MATLAB script, preferences were calculated as percent time spent in the chamber paired with photostimulation.

**Immunohistochemistry**

Mice were transcardially perfused with PBS followed by formalin. Brains were postfixed overnight in formalin at 4 °C and washed with PBS. Free floating sections (40 µm) were prepared with a cryostat, blocked (3% BSA, 2% NGS and 0.1% Triton-X in PBS for two hours), and then incubated with primary antibody overnight at 4 °C. Samples were washed three times with wash

buffer (1× PBS + 0.1% Triton-X), incubated with secondary antibody for one hour at room temperature, washed again, and then mounted and imaged by confocal microscopy. Primary antibodies used were: anti-GFP (Abcam, ab13970, 1:1000), anti-FOS (SCB, sc-52 and sc-52-G), and anti-RFP (Chromotek 5F8, 1:1000).

### *In situ* hybridization

*In situ* hybridization was performed using RNAscope Fluorescent Multiplex Kit (Advanced Cell Diagnostics). Mouse brain tissue was freshly frozen in Tissue-Tek O.C.T Compound, then sectioned into 20-µm sections by cryostat and mounted on Superfrost Plus slides. The sections were fixed in 4% paraformaldehyde (15 min at 4 °C), then dehydrated in a series of ethanol washes following the manufacturer's instructions. The sections were treated with Protease IV in a HybEZ Humidity Control Tray (30 min at RT) and then incubated with target probes in a HybEZ Oven (2 h at 40 °C). For the MnPO, tissues were probed for *Adcyap1* in C1, *Slc17a6* in C2, and *Slc32a1* in C3. For the OVLT, tissues were probed for *Slc32a1* in C1, *Slc17a6* in C2, and e*GFP* in C3. The sections were treated with Hybridize Amp 1-4 then stained with DAPI Fluoromount-G. The sections were then imaged with a confocal microscope and co-localization manually counted from 20× Z stacks.

### Quantification and statistical analysis

Statistical parameters including sample sizes (*n* = number of animal subjects per group), the definition of center, and dispersion and precision measures are reported in the figures and the figure legends. Unless otherwise indicated, values are reported as mean ± s.e.m. (error bars or shaded area). *P* values for pair-wise comparisons were performed using a two-tailed Student's *t*-test. *P* values for all other comparisons were performed using one-way or two-way ANOVA followed by post hoc pair-wise comparisons using Holm-Šídák multiple comparisons test. All

optogenetic trials involved age-matched littermates as controls where possible. Mice were randomly assigned before surgery to either ChR2 or control groups. Data were judged to be statistically significant when $P < 0.05$. In figures, asterisks denote statistical significance $^{*}P < 0.05$, $^{**}P < 0.01$, $^{***}P < 0.001$, $^{****}P < 0.0001$. All statistical analysis was performed using GraphPad Prism 7 software.

## REFERENCES


1 Berridge, K. C. Motivation concepts in behavioral neuroscience. *Physiol. Behav.* **81**, 179–209 (2004).

2 Cabanac, M. Physiological role of pleasure. *Science* **173**, 1103–1107 (1971).

3 Toates, F. M. *Motivational Systems*. (Cambridge University Press, 1986).

4 Hull, C. L. *Principles of Behavior: An Introduction to Behavior Theory*. (Appleton-Century-Crofts, 1943).

5 Spence, K. W. *Behavior Theory & Conditioning*. (Yale University Press, 1956).

6 McKinley, M. J. *et al.* The sensory circumventricular organs of the mammalian brain. *Adv. Anat. Embryol. Cell Biol.* **172**, 1–127 (2003).

7 McKinley, M. J. *et al.* The median preoptic nucleus: front and centre for the regulation of body fluid, sodium, temperature, sleep and cardiovascular homeostasis. *Acta Physiol.* **214**, 8–32 (2015).

8 McKinley, M. J. & Johnson, A. K. The physiological regulation of thirst and fluid intake. *News Physiol. Sci.* **19**, 1–6 (2004).

9 Bourque, C. W. Central mechanisms of osmosensation and systemic osmoregulation. *Nat. Rev. Neurosci.* **9**, 519–531 (2008).

10 Noda, M. & Sakuta, H. Central regulation of body-fluid homeostasis. *Trends Neurosci.* **36**, 661–673 (2013).

11 Zimmerman, C. A., Leib, D. E. & Knight, Z. A. Neural circuits underlying thirst and fluid homeostasis. *Nat. Rev. Neurosci.* **18**, 459–469 (2017).

12 Abbott, S. B. G., Machado, N. L. S., Geerling, J. C. & Saper, C. B. Reciprocal control of drinking behavior by median preoptic neurons in mice. *J. Neurosci.* **36**, 8228–8237 (2016).

13 Oka, Y., Ye, M. & Zuker, C. S. Thirst driving and suppressing signals encoded by distinct neural populations in the brain. *Nature* **520**, 349–352 (2015).

14 Betley, J. N. *et al.* Neurons for hunger and thirst transmit a negative-valence teaching signal. *Nature* **521**, 180–185 (2015).

15 Nation, H. L., Nicoleau, M., Kinsman, B. J., Browning, K. N. & Stocker, S. D. DREADD-induced activation of subfornical organ neurons stimulates thirst and salt appetite. *J. Neurophysiol.* **115**, 3123–3129 (2016).

16 Zimmerman, C. A. *et al.* Thirst neurons anticipate the homeostatic consequences of eating and drinking. *Nature* **537**, 680–684 (2016).

17 Matsuda, T. *et al.* Distinct neural mechanisms for the control of thirst and salt appetite in the subfornical organ. *Nat. Neurosci.* **20**, 230–241 (2017).

18 Teitelbaum, P. in *Operant Behavior: Areas of Research & Application* (ed Honig, W. K.) 565–608 (Appleton-Century-Crofts, 1966).

19 Mangiapane, M. L. & Simpson, J. B. Subfornical organ: forebrain site of pressor and dipsogenic action of angiotensin II. *Am. J. Physiol. Regul. Integr. Comp. Physiol.* **239**, R382–R389 (1980).

20 Buggy, J. & Jonhson, A. K. Preoptic-hypothalamic periventricular lesions: thirst deficits and hypernatremia. *Am. J. Physiol. Regul. Integr. Comp. Physiol.* **233**, R44–R52 (1977).

21 Lenkei, Z., Palkovits, M., Corvol, P. & Llorens-Cortès, C. Expression of angiotensin type-1 (AT1) and type-2 (AT2) receptor mRNAs in the adult rat brain: a functional neuroanatomical review. *Front. Neuroendocrinol.* **18**, 383–439 (1997).

22 Gonzalez, A. D. *et al.* Distribution of angiotensin type 1a receptor-containing cells in the brains of bacterial artificial chromosome transgenic mice. *Neuroscience* **226**, 489–509 (2012).

23 Crews, E. C. & Rowland, N. E. Role of angiotensin in body fluid homeostasis of mice: effect of losartan on water and NaCl intakes. *Am. J. Physiol. Regul. Integr. Comp. Physiol.* **288**, R638–R644 (2005).

24 Allen, W. E. *et al.* Thirst-associated preoptic neurons encode an aversive motivational drive. *Science* **357**, 1149–1155 (2017).

25 Tan, C. L. *et al.* Warm-sensitive neurons that control body temperature. *Cell* **167**, 47–59 (2016).

26 Olds, J. & Milner, P. Positive reinforcement produced by electrical stimulation of septal area and other regions of rat brain. *J. Comp. Physiol. Psychol.* **47**, 419–427 (1954).

27 Stuber, G. D. & Wise, R. A. Lateral hypothalamic circuits for feeding and reward. *Nat. Neurosci.* **19**, 198–205 (2016).

28 Jennings, J. H., Rizzi, G., Stamatakis, A. M., Ung, R. L. & Stuber, G. D. The inhibitory circuit architecture of the lateral hypothalamus orchestrates feeding. *Science* **341**, 1517–1521 (2013).

29 Chen, Y., Lin, Y. C., Zimmerman, C. A., Essner, R. A. & Knight, Z. A. Hunger neurons drive feeding through a sustained, positive reinforcement signal. *eLife* **5**, e18640 (2016).

30 Douglass, A. M. *et al.* Central amygdala circuits modulate food consumption through a positive-valence mechanism. *Nat. Neurosci.* **20**, 1384–1394 (2017).

31 Mandelblat-Cerf, Y. *et al.* Bidirectional anticipation of future osmotic challenges by vasopressin neurons. *Neuron* **93**, 57–65 (2017).

32 Chen, Y., Lin, Y. C., Kuo, T. W. & Knight, Z. A. Sensory detection of food rapidly modulates arcuate feeding circuits. *Cell* **160**, 829–841 (2015).

33 Mandelblat-Cerf, Y. *et al.* Arcuate hypothalamic AgRP and putative POMC neurons show opposite changes in spiking across multiple timescales. *eLife* **4**, e07122 (2015).

34 Leib, D. E., Zimmerman, C. A. & Knight, Z. A. Thirst. *Curr. Biol.* **26**, R1260–R1265 (2016).

35 Romanov, R. A. *et al.* Molecular interrogation of hypothalamic organization reveals distinct dopamine neuronal subtypes. *Nat. Neurosci.* **20**, 176–188 (2017).

36 Slotnick, B. A simple 2-transistor touch or lick detector circuit. *J. Exp. Anal. Behav.* **91**, 253–255 (2009).

*IV. A gut-to-brain signal of fluid osmolarity controls thirst satiation*

---

The material in this chapter is reprinted from:

> Christopher A. Zimmerman, Erica L. Huey, Jamie S. Ahn, Lisa R. Beutler, Chan Lek Tan, Seher Kosar, Ling Bai, Yiming Chen, Timothy V. Corpuz, Linda Madisen, Hongkui Zeng, Zachary A. Knight. A gut-to-brain signal of fluid osmolarity controls thirst satiation. *Nature* 568, 98–102, 2019.

C.A.Z. and Z.A.K. conceived the project and designed the experiments. C.A.Z, E.L.H. and S.K. performed stereotaxic surgery. J.S.A. and L.R.B. performed intragastric surgery. J.S.A. performed vagotomy surgery. C.L.T. generated the *Nxph4-2a-Cre* mouse line. L.M. and H.Z. generated the *Ai148D* mouse line. C.A.Z., E.L.H., S.K., L.B. and Z.A.K. performed histology. E.L.H., J.S.A. and T.V.C. helped to conduct experiments. Y.C. generated code. C.A.Z. conducted the experiments, analyzed the data and generated the figures. C.A.Z. and Z.A.K. prepared the manuscript with input from all authors.

## ABSTRACT

Satiation is the process by which eating and drinking reduce appetite. For thirst, oropharyngeal cues have a critical role in driving satiation by reporting to the brain the volume of fluid that has been ingested[1–12]. By contrast, the mechanisms that relay the osmolarity of ingested fluids remain poorly understood. Here we show that the water and salt content of the gastrointestinal tract are precisely measured and then rapidly communicated to the brain to control drinking behaviour in mice. We demonstrate that this osmosensory signal is necessary and sufficient for satiation during normal drinking, involves the vagus nerve and is transmitted to key forebrain neurons that control thirst and vasopressin secretion. Using microendoscopic imaging, we show that individual neurons compute homeostatic need by integrating this gastrointestinal osmosensory information with oropharyngeal and blood-borne signals. These findings reveal how the fluid homeostasis system monitors the osmolarity of ingested fluids to dynamically control drinking behaviour.

## INTRODUCTION

Drinking influences the volume and composition of the blood[1–4]. However, ingestion of water and salt have opposing consequences for fluid balance, which raises the question of how the brain monitors the osmolarity of ingested fluids.

One way in which the brain controls drinking is by tracking the passage of fluids through the mouth and throat. Classic experiments have demonstrated that drinking temporarily satiates thirst even if the ingested water is immediately drained from the oesophagus[5–8]; recent work has identified specific populations of forebrain neurons that receive this rapid oropharyngeal signal during drinking[9–12]. This mechanism allows the brain to track fluid intake in real time, and thereby quench thirst and inhibit the secretion of vasopressin in anticipation of water absorption into the bloodstream (which occurs gradually over tens of minutes).

Nevertheless, this oropharyngeal signal communicates to the brain only the volume of fluid ingested and not its composition[9,12], which suggests that a distinct mechanism tracks fluid osmolarity during drinking. Taste aversion prevents the consumption of highly concentrated salt solutions[13,14], but there is little evidence that taste fine-tunes fluid consumption to match homeostatic need. The infusion of fluids into the gastrointestinal tract and hepatic portal circulation has previously been reported to influence drinking behaviour and vasopressin secretion in some studies and species but not others[5–8,15–17], and it remains unclear where pre-absorptive fluids are monitored in the periphery, what exactly is sensed, which neurons in the brain receive this information and how they use it to regulate behaviour[1–4]. A fundamental source of ambiguity in these experiments is that traditional behavioural and physiologic readouts vary on the same timescale as fluid absorption (minutes), which makes it difficult to disentangle pre-absorptive signals that are sensed remotely in the periphery from systemic signals that are sensed directly in the brain.

## RESULTS

To gain insight into these longstanding questions, we set out to monitor directly the dynamics of thirst-promoting neurons in the brain while simultaneously manipulating the fluids that were ingested or infused into peripheral tissues. We first measured how fluid osmolarity influences drinking behaviour and thirst neuron activity. Mice were equipped for fibre photometry recordings[18] of glutamatergic neurons in the subfornical organ[9,19,20] (SFO$^{Nos1}$ neurons; defined by expression of *Nos1*) that promote drinking and directly monitor blood osmolarity (Figure 4.1a). These mice were dehydrated and then given access to either water or hypertonic saline. As previously shown[9], the ingestion of either fluid resulted in rapid inhibition of SFO$^{Nos1}$ neurons that was time-locked to the act of drinking (Figure 4.1b). SFO$^{Nos1}$ neurons remained inhibited after bouts of water consumption, but their activity increased to pre-ingestion levels after each bout

of saline consumption terminated (Figure 4.1c). On the basis of the kinetics of this neural activity rebound, we hypothesized that SFO$^{Nos1}$ neurons may receive a signal from the gastrointestinal tract that depends on the osmolarity of the ingested fluid. Consistent with this, we found that isolated changes in gastrointestinal osmolarity were sufficient to influence salt preference and drinking behaviour (Figure 4.6).

To investigate how information about the water and salt content of the gastrointestinal tract is communicated to the brain, we prepared mice with intragastric catheters for fluid infusion into the stomach[21] as well as fibre photometry implants for recording SFO$^{Nos1}$ neuron dynamics (Figure 4.1d). Notably, intragastric infusion of water rapidly inhibited SFO$^{Nos1}$ neurons (latency 105 ± 13 s, mean ± s.e.m.), whereas intragastric infusion of hypertonic saline activated the same population of neurons (Figure 4.1e). Infusions of a range of NaCl concentrations revealed a linear correlation between the osmolarity of the infused fluid and the modulation of SFO$^{Nos1}$ neuron activity (Figure 4.1f). This response was independent of the initial hydration state of the mouse (Figure 4.1g) or the identity of the infused osmolyte (Figure 4.7), and was complete before any detectable change in blood osmolarity occurred (Figure 4.7), which indicates that this response reflects local sensing within the gastrointestinal tract (probably in the proximal small intestine rather than the stomach itself) or hepatic portal circulation[3,15–17]. Consistent with this, intragastric infusion of hypertonic solutions strongly activated SFO$^{Nos1}$ neurons regardless of whether the infused osmolyte could be absorbed into the bloodstream (Figure 4.7). Together, these data reveal that osmolarity is precisely measured within the gastrointestinal tract and then communicated to thirst neurons in the brain.

We next investigated the importance of this gut–brain communication for thirst satiation. In dehydrated mice, intragastric infusion of water rapidly inhibited SFO$^{Nos1}$ neurons (latency 107 ± 15 s, mean ± s.e.m.) and abolished drinking when water was subsequently presented (Figure 4.2a, b, Figure 4.8). This indicates that changes in gastrointestinal osmolarity (but not

distension) are sufficient to satiate thirst and, conversely, that oropharyngeal cues are not required. The behavioural response to changes in gastrointestinal osmolarity—but not to systemic changes in osmolarity—was dependent on hydration state: the intragastric infusion of salt did not stimulate drinking in mice that were hydrated, but did cause an increase in water consumption by dehydrated mice (Figure 4.2b, c, Figure 4.8). This state-dependent effect is reminiscent of how the inhibition of satiation signals for feeding (such as cholecystokinin) can increase meal size in hungry animals, but does not typically trigger the initiation of feeding in animals that are well-fed[22].

One mechanism by which gastrointestinal osmolarity could regulate satiation is by acting as a 'stabilization signal' that determines whether SFO$^{Nos1}$ neurons remain inhibited when drinking terminates (Figure 4.1b, c). If this were true, then delivery of salt to the gastrointestinal tract should cause the activity of SFO$^{Nos1}$ neurons to rebound even after mice drink pure water. To test this, we gave dehydrated mice an intragastric infusion of salt and then analysed the dynamics of SFO$^{Nos1}$ neurons during early bouts of water drinking (Figure 4.2d–f). Indeed, we found that the activity of SFO$^{Nos1}$ neurons rebounded when drinking stopped, such that the neural dynamics during water ingestion now resembled those observed during the ingestion of hypertonic saline (Figure 4.1b, c). This response was specific to salt infused into the stomach, as an identical dose of salt delivered by systemic injection produced no equivalent effect. This suggests that gastrointestinal osmosensation specifies whether the rapid inhibition of thirst neurons by oropharyngeal cues during drinking is transient or durable.

We next investigated whether the inhibition of SFO$^{Nos1}$ neurons by the gastrointestinal osmosensory signal is required for thirst satiation. We surgically equipped mice for intragastric infusion combined with simultaneous optogenetic activation[23] of SFO$^{Nos1}$ neurons (Figure 4.2g). As expected, brief (3 min) intragastric infusion of water into dehydrated mice eliminated drinking when water was subsequently presented. However, optogenetic re-activation of SFO$^{Nos1}$ neurons

during and after water infusion completely blocked this satiating effect (Figure 4.2h, i). This indicates that the SFO is a necessary site in the brain at which the osmosensory signal from the gastrointestinal tract is received to control the termination of drinking.

The peripheral mechanisms that communicate gastrointestinal osmolarity to the brain are unknown. To begin to address this question, we investigated the role of the vagus nerve (cranial nerve X), which densely innervates the stomach and intestines[24]. Subdiaphragmatic vagotomy significantly attenuated the satiating effect of intragastric water infusion and, furthermore, greatly reduced the ability of intragastric water or salt to modulate the activity of SFO$^{Nos1}$ neurons (Figure 4.9a–d). Genetic ablation of a subset of vagal sensory neurons had similar effects (Figure 4.9e–i). Together, these experiments indicate that vagal afferents are an essential part of the pathway by which gastrointestinal osmolarity is communicated to the brain, although they do not rule out an additional role for circulating signals released from the gut following fluid ingestion (Figure 4.9j).

We next investigated how information about the water and salt content of the gastrointestinal tract is represented within the broader neural circuit that controls fluid homeostasis. We first recorded, using fibre photometry, the dynamics of vasopressin-secreting neurons in the supraoptic nucleus (SON$^{Avp}$ neurons; defined by expression of *Avp*) (Figure 4.3a). We confirmed that, similar to SFO$^{Nos1}$ neurons[9], these cells are activated by increases in blood osmolarity (Figure 4.3b) and are rapidly inhibited during drinking[7,10,25] (Figure 4.3c). By combining intragastric infusions with neural recordings, we found that SON$^{Avp}$ neurons are also bidirectionally regulated by gastrointestinal osmolarity, with kinetics similar to those of SFO$^{Nos1}$ neurons (Figure 4.3d, Figure 4.10). This gastrointestinal signal may function in coordination with oropharyngeal cues[10] to pre-emptively regulate the secretion of vasopressin during eating and drinking.

The median preoptic nucleus (MnPO) is a crucial node in the fluid homeostasis system of the brain[1,2] (Figure 4.4a); the MnPO is bidirectionally connected to the SFO through glutamatergic neurons that promote drinking[11,12,26,27] (defined by expression of *Adcyap1*, *Agtr1a* and *Nxph4*) and GABAergic (γ-aminobutyric-acid-releasing) neurons that inhibit drinking[12,26] (defined by expression of *Glp1r*). Given that this classification understates the heterogeneity of MnPO cell types[28] and that the single-cell dynamics of these neurons during behaviour remain unknown, we used microendoscopic imaging[29] to investigate how these neurons encode aspects of fluid balance.

To gain genetic access to thirst-promoting, glutamatergic neurons in the MnPO, we generated knock-in mice that express Cre recombinase from the *Nxph4* locus (*Nxph4-2a-cre* mice) (Figure 4.4b, Figure 4.11). We then targeted the fluorescent calcium indicator GCaMP to these neurons, and implanted a gradient-index lens above the MnPO to record their dynamics in awake, behaving mice (Figure 4.4c). We first tested mice in a paradigm in which they were injected with isotonic saline, then 10 min later injected with salt to induce thirst and—another 10 min later—given access to water (Figure 4.4d, e). Analysis of neural dynamics in this paradigm by *k*-means clustering revealed three distinct subpopulations of MnPO$^{Nxph4}$ neurons (defined by expression of *Nxph4*; Figure 4.12). One subpopulation (cluster 1, 17%) had no response to isotonic saline injection but showed marked and sustained activation after salt challenge, which suggests that these neurons encode blood osmolarity. These same neurons were rapidly and uniformly inhibited during drinking. By contrast, neurons from cluster 2 (34%) showed only transient responses that we interpret as probably representing stress or pain, whereas neurons from cluster 3 (49%) were largely unresponsive. We then investigated how these neurons respond to changes in gastrointestinal osmolarity. Intragastric infusion of water into dehydrated mice inhibited a subset of MnPO$^{Nxph4}$ neurons (24–26%), whereas infusion of hypertonic saline into hydrated mice activated a similar proportion of cells (34%) (Figure 4.4f, g, Figure 4.12).

Registration of neurons across trials revealed that these two populations were largely overlapping, which indicates that a specific subpopulation of MnPO$^{Nxph4}$ neurons is bidirectionally modulated by gastrointestinal signals. Moreover, the majority of gastrointestinal-tuned (inhibited by ≥ 1σ after intragastric infusion of water) MnPO$^{Nxph4}$ neurons were robustly activated during thirst (Figure 4.4h, Figure 4.12). This reveals that individual MnPO$^{Nxph4}$ neurons receive ingestion signals from the oropharynx, satiation signals from the gastrointestinal tract and homeostatic signals from the blood, which they integrate to estimate physiological state. Experiments that combined chemogenetic silencing[30] with fibre photometry recordings suggest that these MnPO neurons are required for relaying gastrointestinal osmolarity information to the SON but not to the SFO (Figure 4.13).

In contrast to MnPO$^{Nxph4}$ neurons, microendoscopic imaging of intermingled GABAergic MnPO$^{Glp1r}$ neurons (defined by expression of *Glp1r*) showed only weak and transient responses during salt challenge (Figure 4.5a, Figure 4.14), which indicates that these cells do not encode blood osmolarity in their baseline activity. We therefore recorded the dynamics of these neurons during re-access to water after dehydration, which revealed strong responses during drinking (Figure 4.5b–d, Figure 4.14). The majority of MnPO$^{Glp1r}$ neurons were either activated (28%) or inhibited (36%) during water ingestion; these responses were time-locked to the act of drinking, such that their activity returned to baseline when ingestion stopped. The cells that exhibited these varied responses were spatially intermingled (Figure 4.5c), which suggests that the functional diversity of the MnPO is not anatomically organized at the scale of our recordings (500 μm). Of note, a previous study using fibre photometry detected only activation of MnPO$^{Glp1r}$ neurons during drinking[12], which suggests that bulk fluorescence measurements masked the existence of an equal proportion of ingestion-inhibited cells. In addition, we observed smaller subsets of MnPO$^{Glp1r}$ neurons that were activated or inhibited by water access alone (Figure 4.5b) or by intragastric infusion of either water or hypertonic saline (Figure 4.5e–g, Figure 4.14).

Together, these data indicate that the majority of GABAergic MnPO neurons are strongly modulated during ingestion, with smaller subsets that encode diverse signals that are relevant to fluid balance (such as water availability, stress and gastrointestinal osmolarity).

## DISCUSSION

Understanding how eating and drinking reduce appetite is one of the fundamental challenges in physiology. Traditionally, this problem has been studied by measuring the effect of peripheral manipulations on behaviour[31,32]. Here we have taken a complementary approach that uses the dynamics of appetite-promoting neurons in the brain as a readout to monitor, in real time, the functional implications of manipulations to peripheral tissues. Using this strategy, we have shown that the water and salt content of the gastrointestinal tract is precisely measured during drinking and then communicated to key neurons in the brain that control fluid balance. Furthermore, we have shown that this gut-to-brain signal requires the vagus nerve, and is necessary and sufficient for the satiation of thirst and regulation of vasopressin secretion during normal behaviour.

The gastrointestinal osmosensory signal described here operates alongside oropharyngeal and blood-borne cues to regulate drinking behaviour. We propose that these anatomically and temporally distinct signals cooperate to promote satiation in three steps (Figure 4.15). First, detection of liquid in the mouth generates a rapid signal that reports the volume of fluid ingested[9–12]. This early estimate of volume inhibits forebrain thirst neurons during the act of drinking, but is transient. Next, detection in the gastrointestinal tract generates a second signal that reports the osmolarity of the ingested fluid. This early estimate of osmolarity stabilizes the inhibition of forebrain thirst neurons if water was consumed, or causes their activity to rebound if the ingested fluid was hypertonic. Finally, absorption of water into the bloodstream alters fluid balance throughout the body, which leads to sustained changes in well-characterized signals (such as blood osmolarity) that are monitored by the brain directly[1–4]. This three-step

mechanism enables the brain to dynamically adjust drinking behaviour to match the level of homeostatic need, regardless of the composition of ingested fluids.

The concept of a ‘set point’ or ‘balance point’ has had a dominant role in shaping how we think about homeostasis[33,34]. Inherent to this concept is the idea that there is an anatomical site at which measurements from the body are integrated to estimate the level of a physiological variable. Although this is commonly assumed to happen in specific neurons in the brain, it has rarely—if ever—been directly observed in vivo. We have shown here that individual, genetically defined thirst neurons in the MnPO integrate information about fluid balance that arises from the oropharynx, gastrointestinal tract and blood. This reveals that homeostatic need can be computed at the level of single neurons in a living animal. Further study of this single-cell integration may provide insights into the origin of the enigmatic set-points that characterize physiological systems.

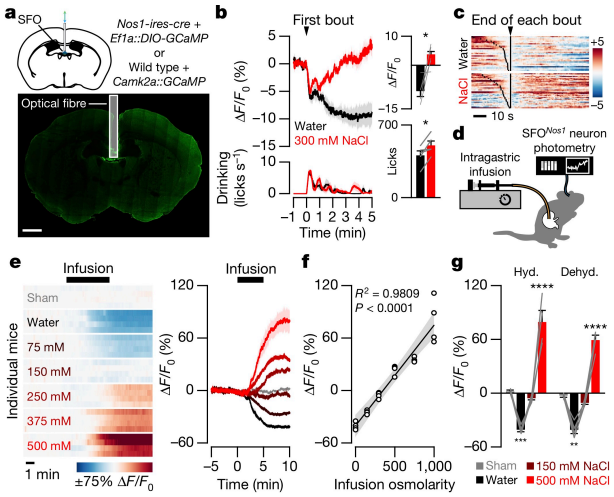


**Figure 4.1 | Gastrointestinal osmolarity modulates drinking behaviour and SFO thirst neuron activity.**

**a**, Schematic for fibre photometry recording of SFO neurons. Scale bar, 1 mm. **b**, Left, average SFO activity and drinking behaviour after dehydration. Right, quantification ($n$ = 5 mice, two-tailed Student's $t$-tests). **c**, SFO neuron dynamics during individual water (29 bouts) or NaCl (37 bouts) drinking bouts. **d**, Schematic for intragastric infusion during fibre photometry recording. **e**, Left, SFO neuron dynamics of individual mice during infusions of water or NaCl, while hydrated. Right, average SFO activity during infusions ($n$ = 4 mice). **f**, Correlation between infusion osmolarity (mOsm $l^{-1}$) and change in SFO activity ($n$ = 4 mice, linear regression). **g**, SFO activity change after infusion while hydrated or dehydrated ($n$ = 4 mice, two-way analysis of variance (ANOVA), Holm–Šídák correction). Hyd., hydrated; dehyd., dehydrated. Error bars represent mean ± s.e.m. Shaded areas in **b**, **e** represent mean ± s.e.m., and in **f** represent 95% confidence interval for the line of best fit. *$P$ < 0.05, **$P$ < 0.01, ***$P$ < 0.001, ****$P$ < 0.0001. The mouse brain in this figure has been reproduced with permission from ref. 35.

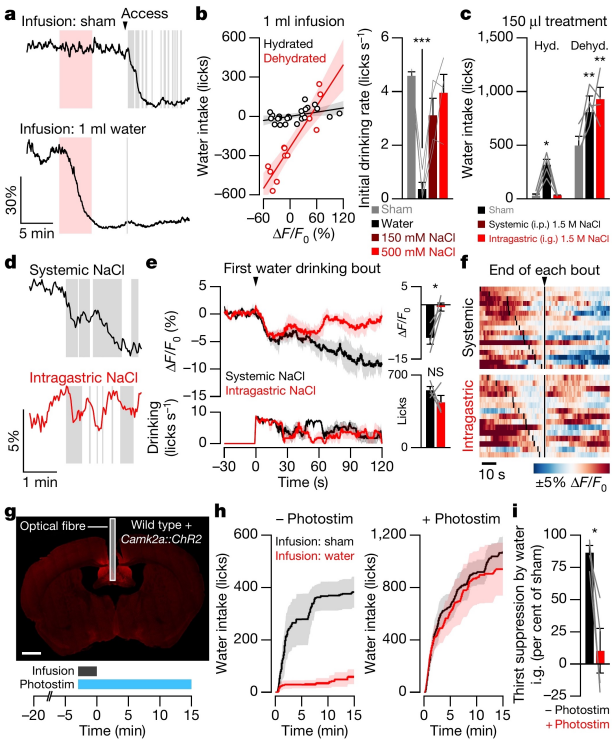


**Figure 4.2 | The gut-to-brain osmosensory signal controls thirst satiation.**
**a**, Example of SFO neuron dynamics during intragastric infusion after dehydration. **b**, Left, correlation between SFO activity change and water intake (relative to sham infusion) after 1-ml infusions into hydrated (black; $n = 24$ experiments from 4 mice, linear regression, $R^2 = 0.2084$, $P = 0.0249$) or dehydrated (red; $n = 12$ experiments from 4 mice, linear regression, $R^2 = 0.8493$, $P < 0.0001$) mice. Right, initial drinking rate of dehydrated mice after infusion ($n = 4$ mice, one-way ANOVA, Holm–Šídák correction). **c**, Water intake after systemic (intraperitoneal (i.p)) or intragastric (i.g.) treatment with 150 µl NaCl ($n = 4$ mice, one-way ANOVA, Holm–Šídák correction). **d**, Example of SFO neuron dynamics during water drinking after treatment with 150 µl NaCl in dehydrated mice. **e**, Left, average SFO activity and drinking behaviour after treatment with 150 µl NaCl in dehydrated mice. Right, quantification ($n = 4$ mice, two-tailed Student's *t*-tests). **f**, SFO neuron dynamics during individual water drinking bouts after systemic (17 bouts) or intragastric (15 bouts) treatment with 150 µl NaCl. **g**, Schematic for intragastric infusion during optogenetic activation. Scale bar, 1 mm. **h**, Dehydration-induced drinking after intragastric infusion either with (right) or without (left) simultaneous photostimulation of SFO neurons ($n = 4$ mice). **i**, Quantification of **h** ($n = 4$ mice, two-tailed Student's *t*-test). Error bars represent mean ± s.e.m. Shaded areas in **a**, **d** represent intragastric infusion (red) or individual licks (grey); shaded areas in **b** represent 95% confidence interval for the line of best fit; shaded areas in **e**, **h** represent mean ± s.e.m. NS, not significant, $^*P < 0.05$, $^{**}P < 0.01$, $^{***}P < 0.001$.

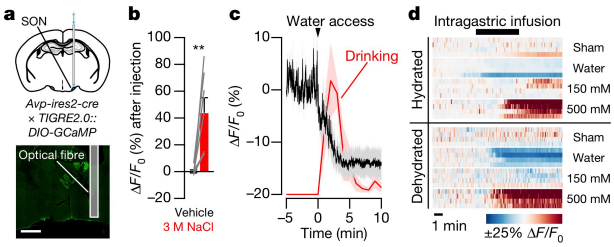


**Figure 4.3 | Vasopressin neurons bidirectionally encode gastrointestinal osmolarity.** **a**, Schematic for fibre photometry recording of SON vasopressin neurons. Scale bar, 1 mm. **b**, Vasopressin neuron response to vehicle or 3 M NaCl intraperitoneal injection ($n = 7$ mice; two-tailed Student's $t$-test). **c**, Average vasopressin neuron activity and drinking behaviour after dehydration ($n = 5$ mice). **d**, Vasopressin neuron dynamics of individual mice during intragastric infusions of water or NaCl ($n = 4$ mice). Error bars and shaded areas represent mean ± s.e.m. $^{**}P < 0.01$. The mouse brain in this figure has been reproduced with permission from ref. 35.

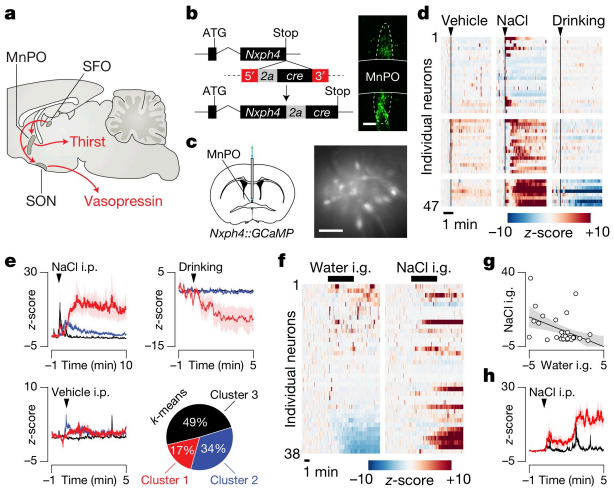


**Figure 4.4 | Individual glutamatergic MnPO neurons integrate information from the oropharynx, gastrointestinal tract and blood.**

**a**, Illustration of the neural circuit that controls fluid homeostasis. **b**, Schematic for generation of the *Nxph4-2a-cre* mouse line (left) and GFP reporter recombination in the MnPO (right). Scale bar, 100 μm. **c**, Schematic for microendoscope imaging of glutamatergic MnPO neurons. Scale bar, 100 μm. **d**, Dynamics of individual neurons tracked during vehicle intraperitoneal injection, 3 M NaCl intraperitoneal injection and water drinking. **e**, Average responses of neuron clusters ($n$ = 47 neurons; see Figure 4.12a). **f**, Dynamics of individual neurons tracked during intragastric infusion of water after dehydration (left), and during 500 mM NaCl intragastric infusion while hydrated (right). **g**, Correlation between the responses ($z$-score) of individual neurons to intragastric infusion of water or 500 mM NaCl ($n$ = 38 neurons; linear regression, $R^2$ = 0.2154, $P$ = 0.0033). **h**, Average response to 3 M NaCl intraperitoneal injection of neurons that were inhibited (red; 26% inhibited ≥ 1σ after infusion) or un-modulated (black; 74%) by intragastric infusion of water ($n$ = 53 neurons; see Figure 4.12d). Shaded areas in **e**, **h** represent mean ± s.e.m., and in **g** represent 95% confidence interval for the line of best fit. The mouse brain in this figure has been reproduced with permission from ref. 35.

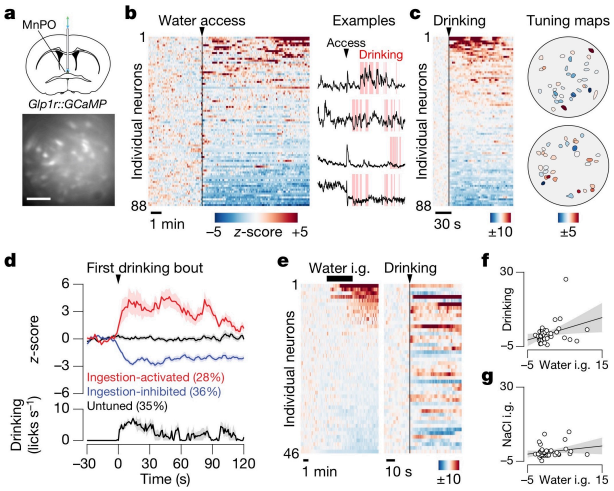


**Figure 4.5 | GABAergic MnPO neurons bidirectionally encode fluid ingestion.**
**a**, Schematic for microendoscope imaging of GABAergic MnPO neurons. Scale bar, 100 μm. **b**, Dynamics of individual neurons during water access after dehydration. **c**, Left, dynamics during drinking. Right, examples of tuning maps. **d**, Average responses of ingestion-activated (modulated ≥ 1σ during first minute of drinking), ingestion-inhibited (modulated ≤ –1σ) and untuned neurons during drinking ($n$ = 77 neurons). **e**, Dynamics of individual neurons tracked during intragastric infusion of water while hydrated (left), and during drinking after dehydration (right). **f**, Correlation between the responses ($z$-score) of individual neurons to intragastric infusion of water or drinking ($n$ = 46 neurons; linear regression, $R^2$ = 0.1062, $P$ = 0.0271). **g**, Correlation between the responses ($z$-score) to intragastric infusion of water or 500 mM NaCl ($n$ = 45 neurons; linear regression, $R^2$ = 0.0467, $P$ = 0.1514). Shaded areas in **b** represent individual licks; shaded areas in **d** represent mean ± s.e.m.; shaded areas in **f**, **g** represent 95% confidence interval for the line of best fit. The mouse brain in this figure has been reproduced with permission from ref. 35.

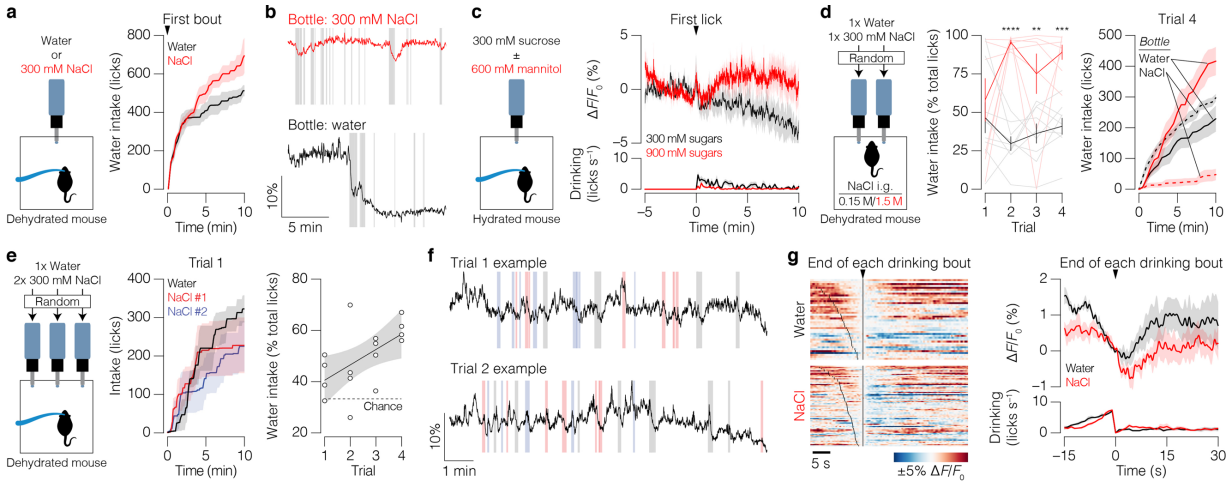


**Figure 4.6 | Gastrointestinal osmolarity influences drinking behaviour and biases salt preference.**

**a**, **b**, Additional data related to Figure 4.1b, c. **a**, Cumulative water or 300 mM NaCl intake after dehydration ($n$ = 5 mice). **b**, Example of SFO neuron dynamics during drinking after dehydration. **c**, Ingestion of hypertonic fluids activates SFO neurons regardless of hydration state. Average SFO activity and drinking behaviour of hydrated mice given ad libitum access to isotonic (300 mM sucrose) or hypertonic (300 mM sucrose + 600 mM mannitol) sugar solutions of similar sweetness ($n$ = 5 mice). **d**, Increases in gastrointestinal osmolarity bias salt and water preference. Left, preference in a two-bottle test after intragastric treatment with hypertonic (red; $n$ = 8 mice) or isotonic (black; $n$ = 9 mice) NaCl (two-way ANOVA, Holm–Šídák correction). Right, cumulative water (solid lines) and 300 mM NaCl (dashed lines) intakes in the same two-bottle test. **e**–**g**, Post-ingestive SFO neuron activity does not reflect the delayed consequences of taste or sensorimotor experience associated with an individual drinking bout. **e**, Mice initially do not distinguish between bottles that contain water and bottles that contain 300 mM NaCl in a three-bottle test after dehydration ($n$ = 4 mice, linear regression, $R^2$ = 0.3163, $P$ = 0.0233). **f**, Example of SFO neuron dynamics during drinking from water (black) and 300 mM NaCl (blue, red) bottles after dehydration. **g**, Left, SFO neuron dynamics during individual water (42 bouts) or NaCl (71 bouts) drinking bouts in trials 1 and 2 of the three-bottle test. Right, average SFO activity after individual drinking bouts ($n$ = 4 mice). In this experiment (**e**–**g**), gastrointestinal osmolarity quickly becomes hypertonic as the dehydrated mice alternate between drinking from water and NaCl bottles, such that SFO neuron activity rebounds even after water-drinking bouts; this suggests that the stabilization signal that either quenches or re-activates SFO neurons after ingestion reflects gastrointestinal osmolarity. Error bars represent mean ± s.e.m. Shaded areas in **a**, **c**–**e**, **g** represent mean ± s.e.m.; shaded areas in **b** represent individual licks; shaded area in the linear regression (right) in **e** represents 95% confidence interval for the line of best fit; shaded areas in **f** represent individual drinking bouts. $^{**}P < 0.01$, $^{***}P < 0.001$.

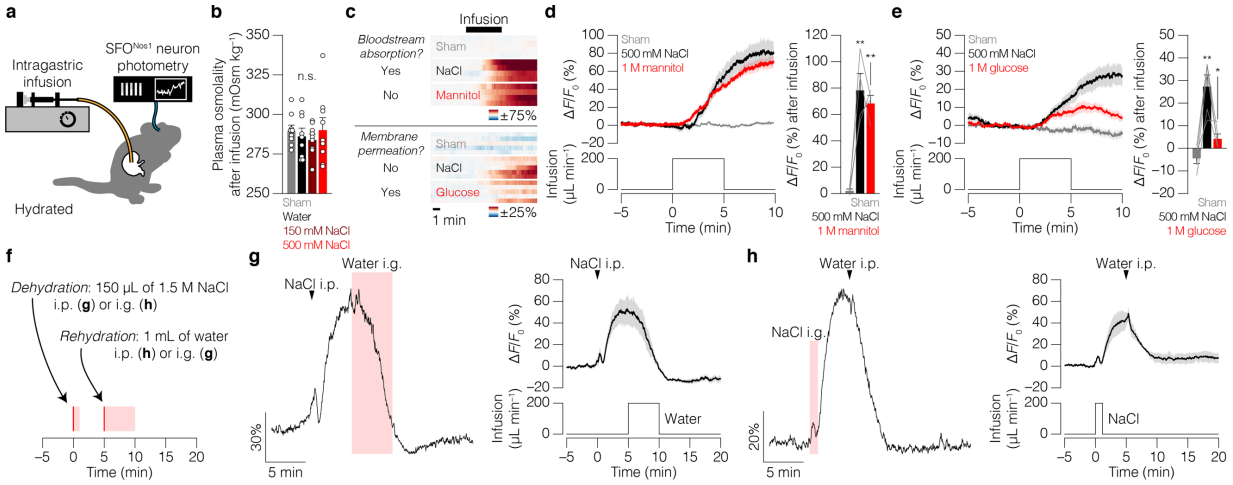


**Figure 4.7 | The gut-to-brain osmosensory signal depends on fluid tonicity but not osmolyte identity.**

**a**, **b** Intragastric infusion does not rapidly alter the state of the blood. **a**, Schematic. **b**, Plasma osmolality of samples collected during approximately 3–6 min after the start of the 5-min intragastric infusion ($n$ = 9 mice per group, one-way ANOVA, Holm–Šídák correction). **c**–**e**, The gut-to-brain osmosensory signal depends on fluid tonicity but not osmolyte identity. **c**, Top, SFO neuron dynamics of individual mice in response to intragastric infusion of equiosmotic concentrations of NaCl, which is absorbed into the bloodstream from the gastrointestinal tract, and mannitol, which is not absorbed ($n$ = 4 mice). Bottom, SFO neuron dynamics of a separate cohort of individual mice in response to intragastric infusion of equiosmotic concentrations of NaCl, which does not permeate cell membranes and has high tonicity, and glucose, which does permeate cell membranes and has low tonicity ($n$ = 5 mice). **d**, Left, average SFO activity during intragastric infusion of NaCl or mannitol. Right, quantification ($n$ = 4 mice, one-way ANOVA, Holm–Šídák correction). **e**, Left, average SFO activity during intragastric infusion of NaCl or glucose. Right, quantification ($n$ = 5 mice, one-way ANOVA, Holm–Šídák correction). **f**–**h**, SFO neurons encode systemic and gastrointestinal osmosensory signals additively rather than hierarchically. **f**, Schematic. **g**, Example (left) and average (right; $n$ = 4 mice) of SFO neuron dynamics during 1.5 M NaCl intraperitoneal injection followed by intragastric infusion of water. **h**, Example (left) and average (right; $n$ = 3 mice) of SFO neuron dynamics during 1.5 M NaCl intragastric infusion followed by intraperitoneal injection of water. Error bars represent mean ± s.e.m. Shaded areas in summary traces (**d**, **e**, **g**, **h**) represent mean ± s.e.m., and in example traces (**g**, **h**) represent intragastric infusion. NS, not significant, $^{*}P < 0.05$, $^{**}P < 0.01$.

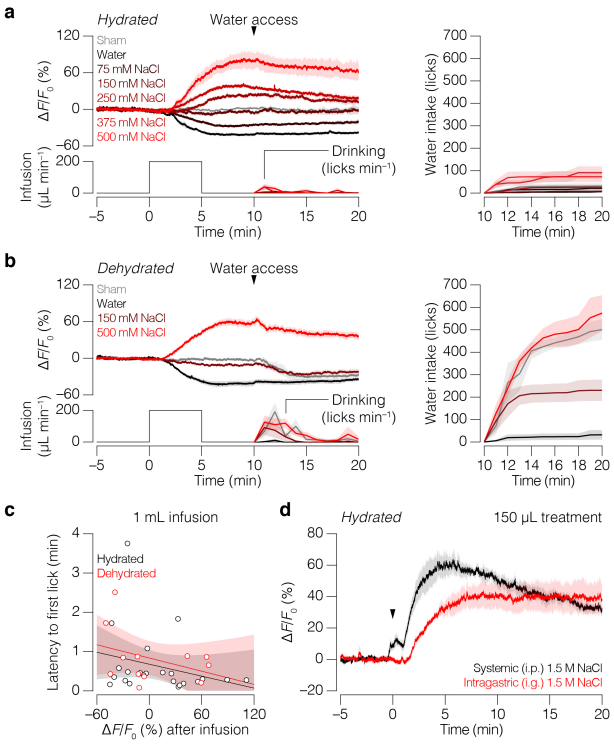


**Figure 4.8 | The gut-to-brain osmosensory signal completely satiates, but only mildly stimulates, thirst.**

**a**, **b**, Additional data related to Figure 4.1e–g and Figure 4.2a, b. **a**, Left, average SFO activity during intragastric infusions and subsequent drinking while hydrated. Right, cumulative water intake ($n$ = 4 mice). **b**, Left, average SFO activity during intragastric infusions and subsequent drinking after dehydration. Right, cumulative water intake ($n$ = 4 mice). **c**, Correlation between SFO activity change and latency to drinking after 1-ml infusions into hydrated (black; $n$ = 23 experiments from 4 mice, linear regression, $R^2$ = 0.0705, $P$ = 0.2208) or dehydrated (red; $n$ = 12 experiments from 4 mice, linear regression, $R^2$ = 0.1321, $P$ = 0.2456) mice. **d**, Additional data related to Figure 4.2c. Average SFO activity after systemic (intraperitoneal) or intragastric treatment with 150 μl NaCl while hydrated. Shaded areas in **a**, **b**, **d** represent mean ± s.e.m., and in **c** represent 95% confidence interval for the line of best fit.

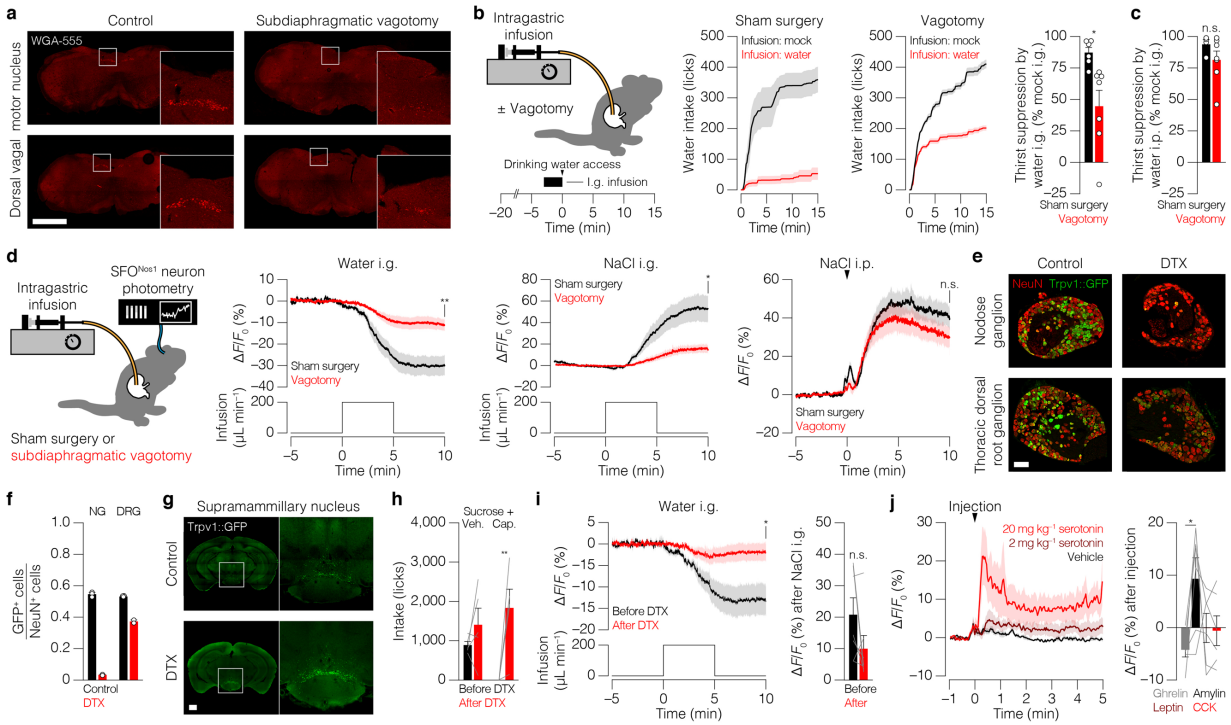


**Figure 4.9 | The gut-to-brain osmosensory signal involves the vagus nerve.**
**a**–**d**, The gut-to-brain osmosensory signal is disrupted by subdiaphragmatic vagotomy. **a**, Vagal motor neuron somas (located in the brainstem and labelled by intraperitoneal injection of wheat germ agglutinin (WGA-555)) were largely absent following subdiaphragmatic vagotomy (two examples per condition). Scale bar, 1 mm. **b**, Drinking after dehydration was less suppressed by intragastric infusion of water in vagotomized mice (middle; $n = 7$ mice) compared to sham mice (left; $n = 6$ mice). Right, quantification (two-tailed Student's $t$-test). **c**, Drinking was similarly suppressed in both groups by systemic (intraperitoneal) delivery of water ($n = 4$ sham and 7 vagotomy mice, two-tailed Student's $t$-test). **d**, SFO modulation by water and 500 mM NaCl intragastric infusions, but not by 1.5 M NaCl intraperitoneal injection, was attenuated in vagotomized mice compared to sham mice ($n = 8$ mice per group, two-tailed Student's $t$-tests). **e**–**i**, The gut-to-brain osmosensory signal involves *Trpv1*-positive sensory neurons. **e**, To specifically ablate *Trpv1*-positive sensory neurons, we treated mice that contain a BAC transgene expressing GFP and the diphtheria toxin (DTX) receptor from the *Trpv1* gene start codon (*Trpv1-Gfp-2a-Dtr* mice) with DTX. Scale bar, 100 μm. **f**, Quantification ($n = 3$ control and 2 DTX mice). NG, nodose ganglion; DRG, dorsal root ganglion. **g**, Treatment with DTX did not ablate *Trpv1*-positive neurons in the brain. Scale bar, 1 mm. **h**, Hydrated mice avoided drinking 300 mM sucrose that contained 100 μM capsaicin (cap.) before—but not after—DTX ablation of *Trpv1*-positive sensory neurons ($n = 5$ mice, two-way ANOVA, Holm–Šídák correction). Veh., vehicle. **i**, SFO modulation by intragastric infusion of water was significantly attenuated after DTX ablation of *Trpv1*-positive sensory neurons, and modulation by intragastric infusion of 500 mM NaCl was slightly attenuated ($n = 7$ mice, two-tailed Student's $t$-tests). **j**, The response of SFO neurons to serotonin and other visceral hormones. **j**, SFO neuron dynamics during injection of two doses of serotonin (left; $n = 5$ mice) and to a single dose (2 mg $kg^{-1}$) of amylin, cholecystokinin (CCK), ghrelin or leptin (right; $n = 6$ mice, one-way ANOVA, Holm–Šídák correction) in hydrated mice. Error bars and shaded areas represent mean ± s.e.m. NS, not significant, $^{*}P < 0.05$, $^{**}P < 0.01$.

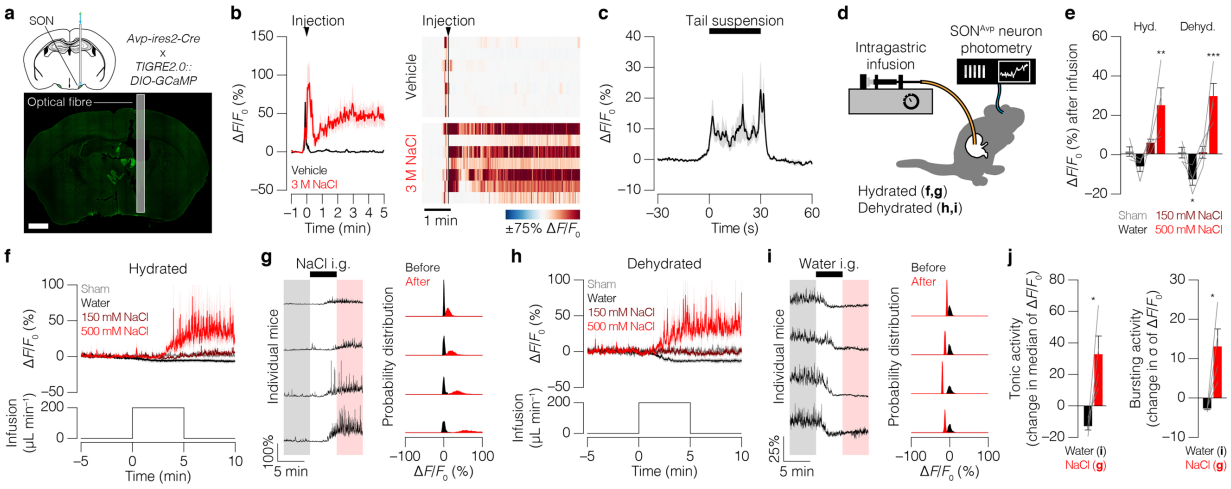


**Figure 4.10 | Vasopressin neurons integrate systemic and gastrointestinal osmosensory signals and are stress-responsive.**

**a**, **b**, Additional data related to Figure 4.3a, b. **a**, Schematic for fibre photometry recording of vasopressin neurons. Scale bar, 1 mm. **b**, Vasopressin neuron dynamics (average, left; individual mice, right) during vehicle or NaCl intraperitoneal injection ($n$ = 7 mice). **c**, Vasopressin neurons are stress-responsive. Vasopressin neuron activity during tail suspension ($n$ = 7 mice). **d–j**, Additional data related to Figure 4.3d. **d**, Schematic. **e**, Change in vasopressin neuron activity after infusion, while hydrated or dehydrated ($n$ = 4 mice, two-way ANOVA, Holm–Šídák correction). **f**, Vasopressin neuron activity during intragastric infusions, while hydrated ($n$ = 4 mice). **g**, Vasopressin neuron dynamics of individual mice (left) and distribution of $\Delta F/F_0$ values before and after intragastric infusion with 500 mM NaCl (right). **h**, Vasopressin neuron dynamics during intragastric infusions after dehydration ($n$ = 4 mice). **i**, Vasopressin neuron activity of individual mice (left) and distribution of $\Delta F/F_0$ values before and after intragastric infusion with water (right). **j**, Gastrointestinal osmolarity modulates both the median of $\Delta F/F_0$ (left; used here as a proxy for tonic activity) and the standard deviation ($\sigma$) of $\Delta F/F_0$ (right; used here as a proxy for bursting activity) of vasopressin neurons ($n$ = 4 mice, two-tailed Student's $t$-tests). Error bars represent mean ± s.e.m. Shaded areas in **b**, **c**, **f**, **h** represent mean ± s.e.m., and in **g**, **i** represent 'before' and 'after' infusion periods. $^*P < 0.05$, $^{**}P < 0.01$, $^{***}P < 0.001$. The mouse brain in this figure has been reproduced with permission from ref. 35.

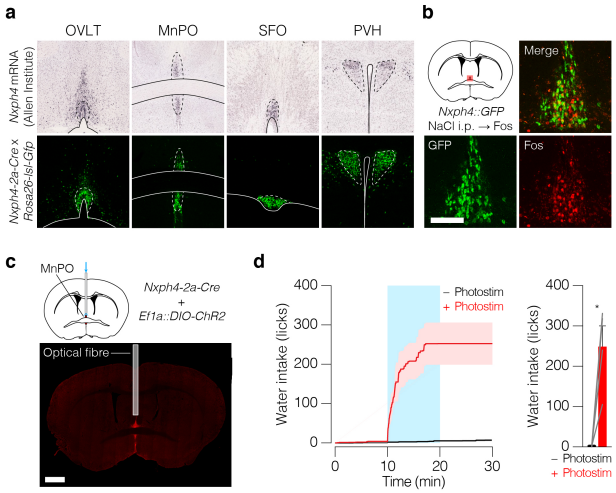


**Figure 4.11 | *Nxph4*-expressing MnPO neurons are activated by dehydration and drive thirst.**

**a**, Additional data related to Figure 4.4b. **a**, The *Nxph4-2a-cre* recombination pattern (bottom; crossed to a GFP reporter line) recapitulates the endogenous *Nxph4* mRNA expression pattern (top; Allen Institute for Brain Science ISH #73521000) in the organum vasculosum of the lamina terminalis (OVLT), MnPO, SFO and paraventricular hypothalamus (PVH). **b**, MnPO$^{Nxph4}$ neurons are activated by dehydration. *Nxph4-2a-cre* recombination (green; crossed to a GFP reporter line) and the immediate early gene product FOS (red; induced by 3 M NaCl intraperitoneal injection) co-localize in the MnPO during dehydration. Scale bar, 100 µm. **c**, **d**, MnPO$^{Nxph4}$ neurons drive thirst. **c**, Schematic for optogenetic activation of MnPO$^{Nxph4}$ neurons. Scale bar, 1 mm. **d**, Left, water intake in response to photostimulation. Right, quantification ($n$ = 4 mice, two-tailed Student's $t$-test). Error bars and shaded areas represent mean ± s.e.m. *$P$ < 0.05. The mouse brains in this figure have been reproduced with permission from ref. 35.

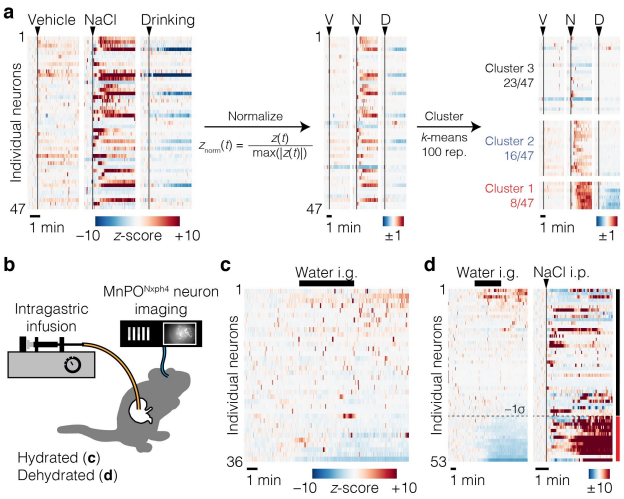


**Figure 4.12 | In vivo imaging of individual glutamatergic MnPO neurons during thirst, drinking and gastrointestinal manipulation.**

**a**, Additional data related to Figure 4.4d, e. **a**, Workflow for *k*-means clustering of individual MnPO$^{Nxph4}$ neurons based on their activity during intraperitoneal injection of vehicle or 3 M NaCl, and water drinking. **b**–**d**, Additional data related to Figure 4.4f–h. **b**, Schematic. **c**, Dynamics of individual neurons during intragastric infusion of water while hydrated. **d**, Dynamics of individual neurons tracked during intragastric infusion of water after dehydration (left) and 3 M NaCl intraperitoneal injection (right). Neurons inhibited ≥ 1σ after intragastric infusion of water were classified as 'gastrointestinal-tuned' (red; 26%) and the remaining neurons were classified as 'gastrointestinal-untuned' (black; 74%) for the time-course plotted in Figure 4.4h.

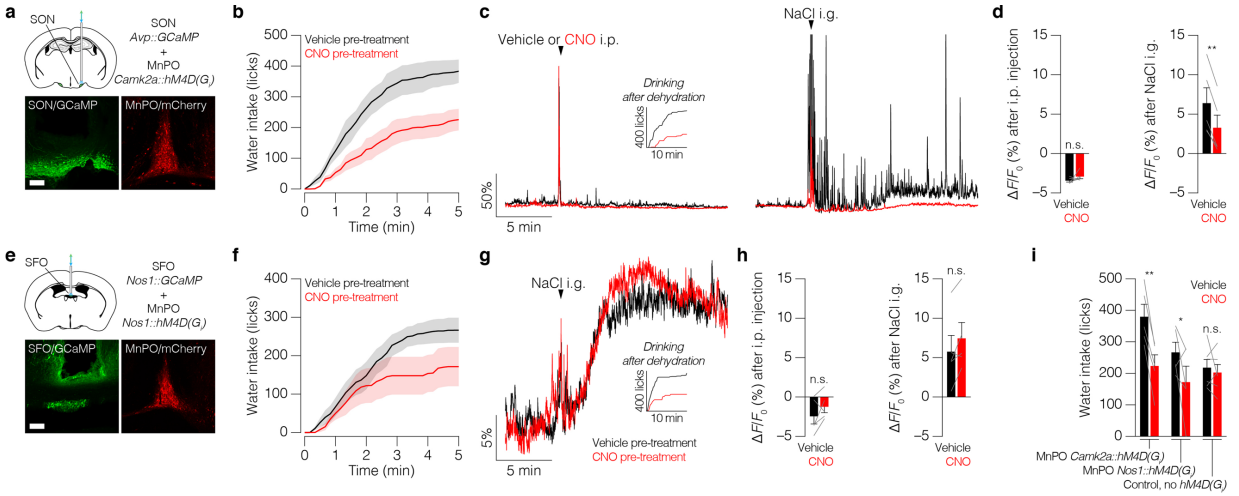


**Figure 4.13 | Glutamatergic MnPO neurons relay the gastrointestinal osmosensory signal to vasopressin neurons.**

**a**–**d**, Glutamatergic MnPO neurons are necessary for relaying gastrointestinal osmosensory information to SON vasopressin neurons. **a**, Schematic for simultaneous fibre photometry recording of vasopressin neurons and chemogenetic inhibition of glutamatergic MnPO neurons. Scale bar, 100 µm. **b**, Injection of CNO inhibited water intake after dehydration ($n = 5$ mice). **c**, Example of vasopressin neuron dynamics during intraperitoneal injection of CNO or vehicle (left) and subsequent intragastric infusion of 1.5 M NaCl by oral gavage (right). Inset, water intake after dehydration for the example mouse. **d**, Quantification of vasopressin neuron response to intraperitoneal injection (left) and NaCl intragastric infusion (right) ($n = 5$ mice, two-tailed Student's *t*-tests). **e**–**h**, Glutamatergic MnPO neurons are not necessary for relaying gastrointestinal osmosensory information to SFO thirst neurons. **e**, Schematic for simultaneous fibre photometry recording of SFO neurons and chemogenetic inhibition of glutamatergic MnPO neurons. Scale bar, 100 µm. **f**, Injection of CNO inhibited water intake after dehydration ($n = 5$ mice). **g**, Example of SFO neuron dynamics during intragastric infusion of 1.5 M NaCl by oral gavage, after intraperitoneal injection of CNO or vehicle. Inset, water intake after dehydration for the example mouse. **h**, Quantification of SFO neuron response to intraperitoneal injection (left) and intragastric infusion of NaCl (right) ($n = 5$ mice, two-tailed Student's *t*-tests). **i**, CNO inhibits drinking in mice that express the Gi-coupled human M4D designer receptor (hM4D(Gi)) in glutamatergic MnPO neurons but not in control mice that lack hM4D(Gi). **i**, Injection of CNO significantly inhibited water intake after dehydration in $MnPO^{Camk2a::hM4D(Gi)}$ + SON mice with photometry implants ($n = 5$ mice; quantified from **b**) and $MnPO^{Nos1::hM4D(Gi)}$ + SFO mice with photometry implants ($n = 5$ mice; quantified from **f**) but not in control mice ($n = 6$ mice, two-way ANOVA, Holm–Šídák correction). Error bars and shaded areas represent mean ± s.e.m. NS, not significant; $^{*}P < 0.05$, $^{**}P < 0.01$. The mouse brains in this figure have been reproduced with permission from ref. 35.

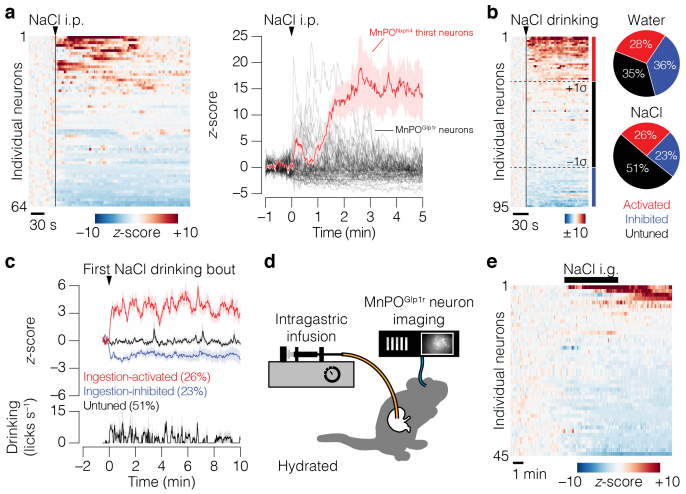


**Figure 4.14 | In vivo imaging of individual GABAergic MnPO neurons during thirst, drinking and gastrointestinal manipulation.**

**a**, Individual GABAergic MnPO neurons do not encode systemic osmolarity in their baseline activity. Left, dynamics of individual neurons during intraperitoneal injection of 3 M NaCl while hydrated. Right, comparison to thirst-activated MnPO$^{Nxph4}$ neurons (cluster 1 from Figure 4.4e). **b**, **c**, Dynamics of ingestion-tuned GABAergic MnPO neurons during hypertonic NaCl drinking. **b**, Left, dynamics of individual neurons during 300 mM NaCl drinking after dehydration (left). Right, proportion of ingestion-activated (red, modulated ≥ 1σ during first min of drinking), ingestion-inhibited (blue, modulated ≤ −1σ) and untuned (black) neurons during water (top; $n = 77$ neurons from Figure 4.5c, d) or 300 mM NaCl (bottom; $n = 95$ neurons) drinking. **c**, Average responses of ingestion-activated, ingestion-inhibited and untuned neurons during 300 mM NaCl drinking ($n = 95$ neurons). Note that ingestion of NaCl persists for much longer than ingestion of water after dehydration (see Figure 4.5d and Figure 4.6a), which may explain differences in the dynamics of ingestion-tuned GABAergic MnPO neurons when mice drink these fluids. **d**, **e**, Additional data related to Figure 4.5e–g. **d**, Schematic. **e**, Dynamics of individual neurons during intragastric infusion of 500 mM NaCl while hydrated.

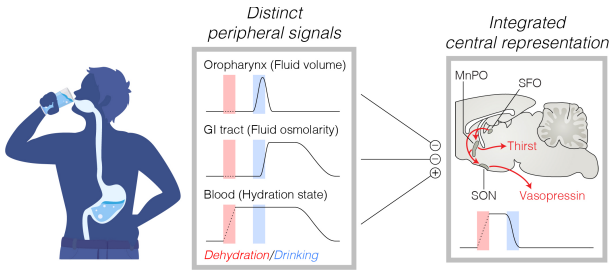


**Figure 4.15 | Model of the neural control of thirst and satiation.**
Anatomically and temporally distinct peripheral sensory signals encode information about the current hydration state of the body (blood) as well as the volume (oropharynx) and osmolarity (gastrointestinal tract) of recently ingested fluids. These signals converge on the thirst circuit of the brain to generate an integrated central representation of fluid balance at the level of individual neurons, which use this information to dynamically control drinking behaviour and vasopressin secretion in real time. Illustration from iStock/artsholic.

## METHODS

Experimental protocols were approved by the University of California, San Francisco IACUC following the NIH Guide for the Care and Use of Laboratory Animals.

### Mouse strains

Adult mice (>6 weeks old) of both sexes were used for experiments. We obtained *Nos1-ires-cre* knock-in mice[36] (*Nos1*$^{tm1(cre)Mgmj}$/J, stock no. 017526), *Avp-ires2-cre* knock-in mice[37] (*Avp*$^{tm1.1(cre)Hze}$/J, stock no. 023530), *Glp1r-ires-cre* knock-in mice[38] (*Glp1r*$^{tm1.1(cre)Lbrl}$/J, stock no. 029283), *Rosa26-lsl-Gfp-Rpl10* knock-in mice[39] (*Gt(ROSA)26Sor*$^{tm1(CAG-EGFP/Rpl10a,-birA)Wtp}$/J, stock no. 022367) and wild-type mice (C57BL/6J, stock no. 000664) from the Jackson Laboratory. We obtained *Ai148D* GCaMP6f knock-in mice[40] (*Igs7*$^{tm148.1(tetO-GCaMP6f,CAG-tTA2)Hze}$) from the Allen Institute for Brain Science, and *Trpv1-Gfp-2a-Dtr* BAC transgenic mice[41] from M. Hoon at the NIH.

We generated *Nxph4-2a-cre* knock-in mice by CRISPR–Cas9-mediated homologous recombination as previously described[27], based on published protocols[42,43]. In brief, homology regions were captured into a plasmid from a BAC containing the *Nxph4* locus by recombination-mediated genetic engineering. The T2A–Cre sequence was inserted immediately upstream of the endogenous stop codon. The final targeting vector contained ~3 kb (5′) and ~1.3 kb (3′) homology arms, and was verified by restriction digest and sequencing. To generate site-specific double-stranded breaks using CRISPR, a single-guide RNA (sgRNA) sequence (GAGTGAGACT GCGATCTGGT) was selected such that the guide sequence would be separated from the PAM site in the genomic DNA by the T2A–Cre insertion. This ensured that the targeting vector and recombined *Nxph4-2a-cre* allele were protected from Cas9 nuclease activity. Super-ovulated female FVB/N mice were mated to FVB/N stud males, and fertilized zygotes were collected from oviducts. Cas9 protein (100 ng/μl), sgRNA (50 ng/μl) and targeting vector DNA (20 ng/μl) were mixed and injected into the pronucleus of fertilized zygotes. Injected zygotes were implanted

into oviducts of pseudo-pregnant CD1 female mice. Founder pups and offspring were genotyped for the presence of the knock-in allele by quantitative PCR (qPCR). Pups positive for the knock-in allele were crossed to reporter mice, and reporter expression patterns were identical to endogenous *Nxph4* expression in the brain (Figure 4.11). All *Nxph4-2a-cre* mice used here were maintained on a mixed FVB/C57Bl/6J background. This mouse line will be made available from the Jackson Laboratory.

All mice were maintained in temperature- and humidity-controlled facilities with 12-h light–dark cycle, and ad libitum access to water and standard chow (PicoLab 5053). *Avp-ires2-cre;Ai148D* mice were fed doxycycline (80 mg/kg) chow (BioServ F7515) until they underwent stereotaxic surgery, after which they were fed standard chow. Mice were allowed at least two weeks for recovery after stereotaxic surgery before testing. For dehydration experiments, mice were water-deprived overnight (>16 h) before testing.

**Viral vectors**

We expressed channelrhodopsin-2 variants[44,45], GCaMP variants[46] and chemogenetic receptors[30] in genetically specified neurons by stereotaxic delivery of recombinant AAVs that encode Cre-dependent or *Camk2a*-promoter transgene cassettes. We obtained AAV1-CAG-FLEX-GCaMP6s, AAV5-Camk2a-GCaMP6f and AAV5-hSyn-FLEX-GCaMP6f from the Penn Vector Core. We obtained AAV5-Camk2a-hChR2(E123T/T159C)-2a-mCherry and AAV5-Ef1a-DIO-hChR2(H134R)-mCherry from the UNC Vector Core. We obtained AAV5-hSyn-DIO-hM4D(Gi)-mCherry and AAV5-Camk2a-hM4D(Gi)-mCherry from Addgene.

**Stereotaxic surgery**

We performed intracranial surgery using stereotaxic coordinates for the SFO, MnPO and SON[35] as previously described[9,27]. For delivery of recombinant AAVs, 100–200 nl of virus was injected

(100 nl/min) at the SFO (–0.60 mm antero-posterior (AP), 0 mm medio-lateral (ML), –2.80 mm dorso-ventral (DV), relative to bregma) or MnPO (+0.35 mm AP, 0 mm ML, –4.20 mm DV). For SFO and MnPO photostimulation experiments, an optical fibre with a 200-μm inner diameter (Thorlabs FT200UMT, CFLC230-10) was placed 0.30 mm above the injection site in the same surgery. For SFO fibre photometry experiments, an optical fibre with a 400-μm inner diameter (Thorlabs BFH48-400, CF440-10) was placed 0.10 mm below the injection site in the same surgery. For SON fibre photometry experiments, an optical fibre with a 400-μm inner diameter (Thorlabs BFH48-400, CF440-10) was placed unilaterally above the SON of *Avp-ires2-cre; Ai148D* mice (–0.75 mm AP, –1.20 mm ML, –5.50 mm DV). For MnPO microendoscope imaging experiments, a gradient-index (GRIN) lens with a 500-μm inner diameter (6.1-mm length; Inscopix 100-000588) was placed 0.10 mm above the injection site in the same surgery.

Optical fibres and GRIN lenses were then affixed to the skull using dental cement (A-M Systems 525000) or MetaBond adhesive cement (Parkwell S380). After at least two weeks recovery from the lens implantation surgery, mice that were going to be used for microendoscope imaging were again anaesthetized, and a baseplate (Inscopix 100-000279) was placed above the lens and affixed with MetaBond adhesive cement. When these mice were not being used for imaging, a baseplate cover (Inscopix 100-000241) was attached to prevent damage to the GRIN lens.

**Intragastric surgery and infusion**

We prepared mice for intragastric infusion as previously described[47], based on published protocols[21]. In brief, catheters were constructed from Silastic tubing (Silastic 508-003), Tygon tubing (Tygon AAD04119) and a curved metal connector (Component Supply Company NE-9019). Biologically compatible mesh was attached to the Silastic tubing and around the metal connector using adhesive (Xiameter RTV-3110 base; Dow Corning 4 catalyst), and a luer adaptor

(Instech LS20) was placed onto the Tygon tubing. Assembled catheters were sterilized using ethylene oxide. Mice with functional photometry, optogenetic or microendoscope implants were anaesthetized with ketamine–xylazine, and the intragastric catheter was surgically implanted into the stomach, as previously described[47]. Mice were allowed at least one week to recover before intragastric infusion and testing.

All intragastric infusions were delivered at a rate of 200 µl/min using a syringe pump (Harvard Apparatus 70-2001). Solutions of NaCl (75, 150, 250, 375 and 500 mM), glucose (1 M) and mannitol (1 M) were prepared using deionized water, and the 1.5 M NaCl solution was prepared using phosphate-buffered saline (PBS). Previous studies have indicated that mannitol is not absorbed into the bloodstream from the intestines[48]. We measured the latency for infused fluids to pass through the intragastric catheter itself en route to the stomach as approximately 13 s.

**Vagotomy surgery**

We prepared mice for intragastric infusion and performed bilateral subdiaphragmatic resection of the vagus nerve during a single procedure. Mice with functional photometry implants were anaesthetized with ketamine–xylazine and the intragastric catheter was surgically implanted as described above. In brief, a 5–7-mm incision was made along the medial line beginning at the distal edge of the sternum. Within a 3-mm radius around the incision site, the skin layer was separated from the muscular layer using blunt dissecting scissors. The liver was then retracted with sterile cotton swabs that had been moistened with saline so that the distal end of the oesophagus could be visualized. Using jeweler's forceps, both branches of the vagus nerve were isolated from the oesophagus and a 1–2-mm section of each branch of the nerve was resected with scissors. Bilateral subdiaphragmatic vagotomy was accompanied in the same surgery by pyloroplasty, in which some of the muscle that composes the pyloric sphincter was incised.

In brief, a 2-mm incision was made along the longitudinal axis of the pylorus without penetrating the lumen. Then, each side of the incision was carefully approximated and sutured with two simple interrupted stitches. The purpose of the pyloroplasty is to maintain gastrointestinal flow through the pylorus[49] and thereby alleviate the excessive food retention, gastric distension and morbidity that accompany subdiaphragmatic vagotomy. Control mice for vagotomy experiments underwent a sham surgery that included intragastric catheter implantation and internal organ manipulation, but not vagotomy or pyloroplasty.

To validate the subdiaphragmatic vagotomy, mice received an intraperitoneal injection of wheat germ agglutinin conjugated to Alexa Fluor 555 (WGA-555; 200 µg per mouse) and were euthanized four days later. WGA-555 is taken up by axon terminals of intact vagal motor neurons[50], the somas of which are located in the brainstem and can be visualized by histology (Figure 4.9a). Labelling in the dorsal motor nucleus of the vagus was greatly reduced—but not completely eliminated—by subdiaphragmatic vagotomy. Residual vagal fibres may be due to incomplete resection during the subdiaphragmatic vagotomy, or to regeneration after surgery[51].

**Behaviour**

We monitored mouse drinking behaviour as previously described[9,27]. All experiments were performed in sound-isolated behavioural chambers (Coulbourn Habitest Modular System) and were performed during the light cycle to control for circadian factors. Fluid consumption was monitored with an electrical lickometer and recorded using Graphic State software (v.4.2, http://www.coulbourn.com/category_s/363.html), or using LJStreamUD software during fibre photometry experiments (v.1.17, http://www.labjack.com/support/software/applications/ud-series/ljstreamud) or nVista software during microendoscope imaging experiments (v.2.0, http://www.inscopix.com/nvista). Mice were acclimated to the behavioural chamber for at least 10 min at the beginning of each testing session.

For two-bottle drinking experiments (Figure 4.6d), wild-type mice were dehydrated and then given access to two randomly placed bottles (1× water, 1× 300 mM NaCl) for >10 min before being returned to their home cages. This test was repeated four times, and the location of the bottles was randomly re-assigned on each trial. Mice were divided into two groups before testing. The first group received a gastric pre-load of hypertonic saline (1.5 M NaCl, 100 µl) by oral gavage one minute before bottle access; the second group received a gastric pre-load of isotonic saline (150 mM NaCl, 100 µl) by oral gavage one minute before bottle access.

For three-bottle drinking experiments (Figure 4.6e–g), SFO photometry mice were dehydrated and then given access to three randomly placed bottles (1× water, 2× 300 mM NaCl) for >10 min before being returned to their home cages. This test was repeated four times, and the location of the bottles was randomly re-assigned on each trial.

**Fibre photometry**

We prepared mice for in vivo fibre photometry recording as previously described[9], based on published protocols[18]. The fibre photometry signal was output to a lock-in amplifier (Stanford Research Systems SR810) with time-constant of 30 ms to allow filtering of noise at higher frequencies. The signal was then digitized (LabJack U6-Pro) and recorded using LJStreamUD software (v.1.17, http://www.labjack.com/support/software/applications/ud-series/ljstreamud) at a 250-Hz sampling rate. Photometry data were subjected to minimal processing, such as within-trial fluorescence normalization and temporal downsampling. For these experiments, intragastric infusions were given in a volume of 1 ml except for Figure 4.2c–f and Figure 4.7h (volume of 200 µl, including ~50 µl dead volume); systemic (intraperitoneal) injections were given in a volume of 150 µl (1.5 M or 3 M NaCl) using PBS as 'vehicle' or in a volume of 1 ml (water); oral gavages (Figure 4.13) were given in a volume of 150 µl. Hormones (Figure 4.9j) were delivered by intraperitoneal injection (volume of 150 µl) for serotonin (2, 20 mg/kg), cholecystokinin

(2 mg/kg), ghrelin (2 mg/kg) and leptin (2 mg/kg), and by subcutaneous injection (volume of 400 µl) for amylin (2 mg/kg) using PBS as vehicle.

**Microendoscope imaging**

We prepared mice for in vivo microendoscope imaging based on published protocols[29,52]. Videos were acquired at 20 Hz (20% LED power, 2.0 gain) using a miniature microscope (Inscopix) and nVista software (v.2.0, http://www.inscopix.com/nvista). After acquisition, videos were first pre-processed, spatially (binning factor of 2) and temporally (binning factor of 5) downsampled, and motion-corrected using Mosaic software (v.1.7, http://support.inscopix.com/mosaic-workflow). Activity traces for individual neurons were then extracted from these videos using the constrained non-negative matrix factorization (CNMF-E) pipeline[53] (http://www.github.com/zhoupc/cnmf_e) implemented in MATLAB. After initial CNMF-E segmentation, extracted neurons were manually refined to avoid potential confounding factors from uncorrected motion artefacts, region of interest duplication and over-segmentation of the same spatial components. For each experiment, activity traces for individual neurons were extracted from recordings from 3–4 mice and then pooled for subsequent analysis. For these experiments, intragastric infusions were given in a volume of 1 ml; systemic (intraperitoneal) injections were given in a volume of 100 µl (3 M NaCl) using PBS as vehicle.

**Optogenetics**

We prepared mice for in vivo photostimulation as previously described[9,27], based on published protocols[23,54]. A DPSS 473-nm laser (Shanghai Laser and Optics Century BL473-100FC) was controlled by Graphic State software (v.4.2, http://www.coulbourn.com/category_s/363.html) through a TTL signal generator (Coulbourn H03-14), and synchronized with behaviour experiments. The laser power was measured to be ~15 mW at the patch cable tip and was

delivered in 10-ms pulses at 20 Hz. For these experiments, intragastric infusions were given in a volume of 600 µl.

**Chemogenetics**

We prepared mice for in vivo chemogenetic inhibition based on published protocols[55,56]. Clozapine *N*-oxide (CNO, 1 mg/kg) was delivered by intraperitoneal injection (volume of 125 µl) with 0.6% DMSO in PBS as vehicle. For these experiments (Figure 4.13), CNO or vehicle was delivered >15 min before water access after dehydration or oral gavage of hypertonic NaCl.

**Diphtheria toxin receptor ablation**

We ablated genetically defined (*Trpv1*-positive) sensory neurons using the diphtheria toxin (DTX) receptor-based strategy described in published protocols[41,57]. In brief, *Nos1-ires-cre; Trpv1-Gfp-2a-Dtr* mice were first equipped for fibre photometry recording of SFO neurons and screened for functionality. Mice with functional photometry implants then underwent intragastric catheterization surgery and, after recovery, were tested in a series of experiments ('before DTX' in Figure 4.9h, i). Mice were then given two intramuscular injections of DTX (each injection was 50 µl of 25 µg/ml DTX), separated by three days, and were then allowed at least five additional days to recover, after which they underwent the same series of experiments ('after DTX').

We confirmed the ablation of *Trpv1*-positive sensory neurons in two ways. First, *Nos1-ires-cre;Trpv1-Gfp-2a-Dtr* mice with photometry implants and intragastric catheters were given access to a single bottle of palatable sugar solution (300 mM sucrose) that also contained either capsaicin (100 µM) or vehicle (0.15% TWEEN-80 + 1.5% DMSO). This test was conducted once before and once after DTX treatment, and intake was quantified from 1–2 h after access (Figure 4.9h). Second, *Trpv1-Gfp-2a-Dtr;hSyn-Nanobody-Rpl10* mice were used for histology of the nodose ganglion and thoracic dorsal root ganglion, after DTX treatment or no treatment. This

revealed a nearly complete ablation of *Trpv1*-positive vagal neurons and more-limited ablation of *Trpv1*-positive dorsal root ganglion neurons (Figure 4.9e, f). We also observed sparse labelling of *Trpv1*-positive neurons in the brain[58], and this was unaffected by DTX treatment (Figure 4.9g).

**Plasma osmolality**

Mice equipped with intragastric catheters were fully hydrated and received an infusion (sham, water, 150 mM NaCl or 500 mM NaCl) at 200 µl/min for 5 min. Beginning 3 min after the start of infusion, 125 µl of blood was collected from the tail vein using EDTA-coated capillary tubes (RAM Scientific 07-6011). The blood collection process took approximately 3 min per mouse. Plasma was isolated by centrifugation (1,000*g* for 10 min), diluted in deionized water and frozen until measurement. Osmolality was then measured in triplicate for each sample using a freezing point osmometer (Fiske Associates 210). Mice were allowed one week for recovery between sessions.

**Histology**

Mice were transcardially perfused with PBS followed by 10% formalin. To visualize forebrain and hindbrain nuclei, whole brains were dissected, post-fixed in 10% formalin overnight at 4 °C and then cryo-protected in 30% sucrose overnight at 4 °C. Free-floating sections (40 µm) were prepared with a cryostat, blocked (3% BSA, 2% NGS and 0.1% Triton-X in PBS for 2 h) and then incubated with primary antibody (chicken anti-GFP, Abcam ab13970, 1:1,000; rat anti-RFP, ChromoTek 5f8, 1:1,000; goat anti-mCherry, Acris ab0040-200, 1:1,000; rabbit anti-FOS, Santa Cruz Biotech sc52, 1:500) overnight at 4 °C. Sections were then washed, incubated with secondary antibody (Alexa Fluor 488 goat anti-chicken, Life Technologies a11039, 1:1,000; Alexa Fluor 568 goat anti-rat, Life Technologies a11077, 1:1,000; Alexa Fluor 568 goat anti-rabbit, Life Technologies a11011, 1:1,000; Alexa Fluor 568 donkey anti-goat, Life Technologies a11057, 1:1,000) for 2 h at room temperature, washed again, mounted with DAPI Fluoromount-G

(Southern Biotech) and then imaged with a confocal microscope (Zeiss LSM-700). To visualize WGA-555 labelling of the dorsal motor nucleus of the vagus, sections were mounted and imaged without staining.

To visualize sensory ganglia, the ventral aspects of the skull and vertebral columns were dissected, post-fixed in 10% formalin overnight at 4 °C and then washed at room temperature. The nodose ganglion and thoracic dorsal root ganglion were further dissected, and then cryo-protected in 30% sucrose overnight at 4 °C. Sections (20 μm) were prepared with a cryostat, mounted on slides, washed, blocked (5% NGS and 0.1% Triton-X in PBS for 30 min) and then incubated with primary antibody (chicken anti-GFP, Abcam ab13970, 1:1,000; rabbit anti-NeuN, Milliipore abn78, 1:1,000) overnight at 4 °C. Sections were then washed, incubated with secondary antibody (Alexa Fluor 488 goat anti-chicken, Life Technologies a11039, 1:500; Alexa Fluor 568 goat anti-rabbit, Life Technologies a11011, 1:500) for 2 h at room temperature, washed again, mounted with DAPI Fluoromount-G (Southern Biotech) and then imaged with the confocal microscope.

Images underwent minimal processing (such as brightness and contrast adjustments) performed using the Fiji distribution of ImageJ (v.2.0, http://www.fiji.sc/).

**Data analysis**

We analysed behaviour data, fibre photometry data and microendoscope imaging data using custom MATLAB (v.R2018a, http://www.mathworks.com/products/matlab) scripts. Throughout the paper, a drinking bout is defined as any set of ten or more licks in which no inter-lick interval is greater than one second. For some assays, multiple trials of the same experiment were performed for an individual mouse, and then averaged and treated as a single replicate. For photometry data, all responses were normalized using the function: $\Delta F/F_0 = (F - F_0)/F_0$, in which $F$ is the raw photometry signal and $F_0$ is the median of $F$ during the baseline period (plotted data

before injection, infusion or drinking). For quantification in bar graphs, the median $\Delta F/F_0$ of a 10-s (for long experiments with >5 min of data plotted) or 2-s (for short experiments with <5 min of data plotted) window is reported. For peri-event time histograms around the end of drinking bouts, $F_0$ was defined as the median of $F$ at the time (± 1 s) of the last lick in the bout. For microendoscope imaging data, all responses were normalized using the function $z = (C_{raw} - \mu)/\sigma$, in which $C_{raw}$ is the output of the CNMF-E pipeline, $\mu$ is the mean of $C_{raw}$ during the baseline period and $\sigma$ is the standard deviation of $C_{raw}$ during the baseline period. *k*-means clustering was performed using the built-in MATLAB function (http://www.mathworks.com/help/stats/kmeans.html), as illustrated in Figure 4.12a. For quantification in linear regressions, the mean *z*-score of the final 1 min of plotted data for intragastric infusions (9–10 min after infusion begins) or of the first 1 min after drinking onset (first lick in first bout) is reported. The mean *z*-score of the first 1 min after the first lick in the first drinking bout was used to classify GABAergic MnPO neuron responses during ingestion (Figure 4.5c, d, Figure 4.14b, c). For time-courses of water intake, time 0 is the moment of water access unless otherwise noted. Initial drinking rate (Figure 4.2b) was calculated from the first 1 min of drinking after the first lick in the experiment. Latency to inhibition of $SFO^{Nos1}$ neurons by intragastric infusion of water was calculated as the moment at which the fibre photometry signal crossed a threshold of four standard deviations (4σ) below the mean signal level of the baseline period, and was adjusted to account for the dead volume of the intragastric catheter.

**Statistics and reproducibility**

We performed statistical analyses using Prism software (v.7.0, http://www.graphpad.com/scientific-software/prism). Throughout the paper, values are reported as mean ± s.e.m. (error bars or shaded area). In figures with linear regressions, shaded areas represent the 95% confidence interval for the line of best fit. *P* values for pair-wise comparisons were performed

using a two-tailed Student's *t*-test (with repeated measures when possible). *P* values for comparisons across multiple groups were performed using ANOVA (with repeated measures when possible) and corrected for multiple comparisons using the Holm–Šídák method (within-group comparison to the control condition). No statistical methods were used to predetermine sample size. The experiments were not randomized. The investigators were not blinded to allocation during experiments and outcome assessment. Representative images were selected from one to five original biological replicates, and representative recordings were selected from three to five original biological replicates.

## REFERENCES


1 Zimmerman, C. A., Leib, D. E. & Knight, Z. A. Neural circuits underlying thirst and fluid homeostasis. *Nat. Rev. Neurosci.* **18**, 459–469 (2017).

2 Gizowski, C. & Bourque, C. W. The neural basis of homeostatic and anticipatory thirst. *Nat. Rev. Nephrol.* **14**, 11–25 (2018).

3 Johnson, A. K. & Thunhorst, R. L. The neuroendocrinology of thirst and salt appetite: visceral sensory signals and mechanisms of central integration. *Front. Neuroendocrinol.* **18**, 292–353 (1997).

4 McKinley, M. J. & Johnson, A. K. The physiological regulation of thirst and fluid intake. *News Physiol. Sci.* **19**, 1–6 (2004).

5 Bellows, R. T. Time factors in water drinking in dogs. *Am. J. Physiol.* **125**, 87–97 (1938).

6 Adolph, E. F., Barker, J. P. & Hoy, P. A. Multiple factors in thirst. *Am. J. Physiol.* **178**, 538–562 (1954).

7 Thrasher, T. N., Nistal-Herrera, J. F., Keil, L. C. & Ramsay, D. J. Satiety and inhibition of vasopressin secretion after drinking in dehydrated dogs. *Am. J. Physiol. Endocrinol. Metabol.* **240**, E394–E401 (1981).

8 Figaro, M. K. & Mack, G. W. Regulation of fluid intake in dehydrated humans: role of oropharyngeal stimulation. *Am. J. Physiol. Regul. Integr. Comp. Physiol.* **272**, R1740–R1746 (1997).

9 Zimmerman, C. A. *et al.* Thirst neurons anticipate the homeostatic consequences of eating and drinking. *Nature* **537**, 680–684 (2016).

10 Mandelblat-Cerf, Y. *et al.* Bidirectional anticipation of future osmotic challenges by vasopressin neurons. *Neuron* **93**, 57–65 (2017).

11 Allen, W. E. *et al.* Thirst-associated preoptic neurons encode an aversive motivational drive. *Science* **357**, 1149–1155 (2017).

12 Augustine, V. *et al.* Hierarchical neural architecture underlying thirst regulation. *Nature* **555**, 204–209 (2018).

13 Weiner, I. H. & Stellar, E. Salt preference of the rat determined by a single-stimulus method. *J. Comp. Physiol. Psychol.* **44**, 394–401 (1951).

14 Oka, Y., Butnaru, M., von Buchholtz, L., Ryba, N. J. P. & Zuker, C. S. High salt recruits aversive taste pathways. *Nature* **494**, 472–475 (2013).

15 Maddison, S., Wod, R. J., Rolls, E. T., Rolls, B. J. & Gibbs, J. Drinking in the rhesus monkey: peripheral factors. *J. Comp. Physiol. Psychol.* **94**, 365–374 (1980).

16 Baertschi, A. J. & Vallet, P. G. Osmosensitivity of the hepatic portal vein area and vasopressin release in rats. *J. Physiol.* **315**, 217–230 (1981).

17 Stricker, E. M., Callahan, J. B., Huang, W. & Sved, A. F. Early osmoregulatory stimulation of neurohypophyseal hormone secretion and thirst after gastric NaCl loads. *Am. J. Physiol. Regul. Integr. Comp. Physiol.* **282**, R1710–R1717 (2002).

18 Gunaydin, L. A. *et al.* Natural neural projection dynamics underlying social behavior. *Cell* **157**, 1535–1551 (2014).

19 Oka, Y., Ye, M. & Zuker, C. S. Thirst driving and suppressing signals encoded by distinct neural populations in the brain. *Nature* **520**, 349–352 (2015).

20 Betley, J. N. *et al.* Neurons for hunger and thirst transmit a negative-valence teaching signal. *Nature* **521**, 180–185 (2015).

21 Ueno, A. *et al.* Mouse intragastric infusion (*iG*) model. *Nat. Protoc.* **7**, 771–781 (2012).

22 Andermann, M. L. & Lowell, B. B. Toward a wiring diagram understanding of appetite control. *Neuron* **95**, 757–778 (2017).

23 Zhang, F. *et al.* Optogenetic interrogation of neural circuits: technology for probing mammalian brain structures. *Nat. Protoc.* **5**, 439–456 (2010).

24 Berthoud, H.-R. & Neuhuber, W. L. Functional and chemical anatomy of the afferent vagal system. *Auton. Neurosci.* **85**, 1–17 (2000).

25 Vincent, J. D., Arnauld, E. & Bioulac, B. Activity of osmosensitive single cells in the hypothalamus of the behaving monkey during drinking. *Brain Res.* **44**, 371–384 (1972).

26 Abbott, S. B. G., Machado, N. L. S., Geerling, J. C. & Saper, C. B. Reciprocal control of drinking behavior by median preoptic neurons in mice. *J. Neurosci.* **36**, 8228–8237 (2016).

27 Leib, D. E. *et al.* The forebrain thirst circuit drives drinking through negative reinforcement. *Neuron* **96**, 1272–1281 (2017).

28 McKinley, M. J. *et al.* The median preoptic nucleus: front and centre for the regulation of body fluid, sodium, temperature, sleep and cardiovascular homeostasis. *Acta Physiol.* **214**, 8–32 (2015).

29 Ghosh, K. K. *et al.* Miniaturized integration of a fluorescence microscope. *Nat. Methods* **8**, 871–878 (2011).

30 Armbruster, B. N., Li, X., Pausch, M. H., Herlitze, S. & Roth, B. L. Evolving the lock to fit the key to create a family of G protein-coupled receptors potently activated by an inert ligand. *Proc. Natl. Acad. Sci. USA* **104**, 5163–5168 (2007).

31 Bernard, C. *Leçons de physiologie expérimentale appliquée à la médecine*. (Baillière, 1856).

32 Richter, C. P. Total self regulatory functions in animals and human beings. *Harvey Lecture Series* **38**, 63–103 (1943).

33 Cannon, W. B. Organization for physiological homeostasis. *Physiol. Rev.* **9**, 399–431 (1929).

34 Berridge, K. C. Motivation concepts in behavioral neuroscience. *Physiol. Behav.* **81**, 179–209 (2004).

35 Paxinos, G. & Franklin, K. B. J. *The Mouse Brain in Stereotaxic Coordinates*. 4 edn, (Academic Press, 2012).

36 Leshan, R. L., Greenwald-Yarnell, M., Patterson, C. M., Gonzalez, I. E. & Myers, M. G. J. Leptin action through hypothalamic nitric oxide synthase-1–expressing neurons controls energy balance. *Nat. Med.* **18**, 820–823 (2012).

37 Harris, J. A. *et al.* Anatomical characterization of Cre driver mice for neural circuit mapping and manipulation. *Front. Neural Circuits* **8**, 1–16 (2014).

38 Williams, E. K. *et al.* Sensory neurons that detect stretch and nutrients in the digestive system. *Cell* **166**, 209–221 (2016).

39 Zhou, P. *et al.* Interrogating translational efficiency and lineage-specific transcriptomes using ribosome affinity purification. *Proc. Natl. Acad. Sci. USA* **110**, 15395–15400 (2013).

40 Daigle, T. L. *et al.* A suite of transgenic driver and reporter mouse lines with enhanced brain-cell-type targeting and functionality. *Cell* **174**, 465–480 (2018).

41 Pogorzala, L. A., Mishra, S. K. & Hoon, M. A. The cellular code for mammalian thermosensation. *J. Neurosci.* **33**, 5533–5541 (2013).

42 Yang, H. *et al.* One-step generation of mice carrying reporter and conditional alleles by CRISPR/Cas-mediated genome engineering. *Cell* **154**, 1370–1379 (2013).

43 Yang, H., Wang, H. & Jaenisch, R. Generating genetically modified mice using CRISPR/Cas-mediated genome engineering. *Nat. Protoc.* **9**, 1956–1968 (2014).

44 Boyden, E. S., Zhang, F., Bamberg, E., Nagel, G. & Deisseroth, K. Millisecond-timescale, genetically targeted optical control of neural activity. *Nat. Neurosci.* **8**, 1263–1268 (2005).

45 Berndt, A. *et al.* High-efficiency channelrhodopsins for fast neuronal stimulation at low light levels. *Proc. Natl. Acad. Sci. USA* **108**, 7595–7600 (2011).

46 Chen, T.-W. *et al.* Ultrasensitive fluorescent proteins for imaging neuronal activity. *Nature* **499**, 295–300 (2013).

47 Beutler, L. R. *et al.* Dynamics of gut-brain communication underlying hunger. *Neuron* **96**, 461–475 (2017).

48 Höber, R. & Höber, J. Experiments on the absorption of organic solutes in the small intestine of rats. *J. Cell. Comp. Physiol.* **10**, 401–422 (1937).

49 Mordes, J. P., el Lozy, M., Herrera, M. G. & Silen, W. Effects of vagotomy with and without pyloroplasty on weight and food intake in rats. *Am. J. Physiol. Regul. Integr. Comp. Physiol.* **236**, R61–R66 (1979).

50 Powley, T. L., Fox, E. A. & Berthoud, H. R. Retrograde tracer technique for assessment of selective and total subdiaphragmatic vagotomies. *Am. J. Physiol. Regul. Integr. Comp. Physiol.* **253**, R361–R370 (1987).

51 Powley, T. L., Chi, M. M., Baronowsky, E. A. & Phillips, R. J. Gastrointestinal tract innervation of the mouse: afferent regeneration and meal patterning after vagotomy. *Am. J. Physiol. Regul. Integr. Comp. Physiol.* **289**, R563–R574 (2005).

52 Resendez, S. L. *et al.* Visualization of cortical, subcortical and deep brain neural circuit dynamics during naturalistic mammalian behavior with head-mounted microscopes and chronically implanted lenses. *Nat. Protoc.* **11**, 566–597 (2016).

53 Zhou, P. *et al.* Efficient and accurate extraction of in vivo calcium signals from microendoscopic video data. *eLife* **7**, e28728 (2018).

54 Sparta, D. R. *et al.* Construction of implantable optical fibers for long-term optogenetic manipulation of neural circuits. *Nat. Protoc.* **7**, 12–23 (2012).

55 Krashes, M. J. *et al.* Rapid, reversible activation of AgRP neurons drives feeding behavior in mice. *J. Clin. Invest.* **121**, 1424–1428 (2011).

56 Roth, B. L. DREADDs for neuroscientists. *Neuron* **89**, 683–694 (2016).

57 Saito, M. *et al.* Diphtheria toxin receptor–mediated conditional and targeted cell ablation in transgenic mice. *Nat. Biotechnol.* **19**, 746–750 (2001).

58 Cavanaugh, D. J. *et al. Trpv1* reporter mice reveal highly restricted brain distribution and functional expression in arteriolar smooth muscle cells. *J. Neurosci.* **31**, 5067–5077 (2011).

**Publishing Agreement**

*It is the policy of the University to encourage the distribution of all theses, dissertations, and manuscripts. Copies of all UCSF theses, dissertations, and manuscripts will be routed to the library via the Graduate Division. The library will make all theses, dissertations, and manuscripts accessible to the public and will preserve these to the best of their abilities, in perpetuity.*

***Please sign the following statement:***

*I hereby grant permission to the Graduate Division of the University of California, San Francisco to release copies of my thesis, dissertation, or manuscript to the Campus Library to provide access and preservation, in whole or in part, in perpetuity.*

Author Signature

2019-08-16

Date